FABRICATION AND CHARACTERIZATION OF MIXED METAL SULFIDE THIN FILMS FOR PHOTOELECTROCHEMICAL APPLICATION

KELVIN LAU CHING

MASTER OF SCIENCE

FACULTY OF SCIENCE
UNIVERSITI TUNKU ABDUL RAHMAN
OCTOBER 2020

FABRICATION AND CHARACTERIZATION OF MIXED METAL SULFIDE THIN FILMS FOR PHOTOELECTROCHEMICAL APPLICATION

By

KELVIN LAU CHING

A dissertation submitted to the Department of Chemical Science,
Faculty of Science,
Universiti Tunku Abdul Rahman,
in partial fulfillment of the requirements for the degree of
Master of Science
October 2020

ABSTRACT

FABRICATION AND CHARACTERIZATION OF MIXED METAL SULFIDE THIN FILM FOR PHOTOELECTROCHEMICAL APPLICATION

Kelvin Lau Ching

The M-doped (M = Fe, Co or Ni) thin films deposited on FTO substrate were prepared from AACVD process with dual precursors of $[(\eta^5\text{-Cp})\text{Mo}(\text{SMe})_2]_2$ (**2**) (Cp = C_5H_5) and Cp_2M in THF under Argon at 550 °C in 20 min. The Cp_2M worked as dopant was added in different mol%. The structure of the films was determined by XRD where rhombohedral MoS_2 and monoclinic Mo_2S_3 were observed in all films. The Fe-, Co- and Ni-doped thin films also showed the presence of monoclinic $Fe(MoS_2)_2$, monoclinic $Co(MoS_2)_2$ and rhombohedral Mo_3NiS_4, respectively. In the Raman Spectroscopy, all films showed similar bonding mode despite having different dopants. In the XPS spectroscopy, Mo^{3+}, Mo^{4+} and S^{2-} were observed in all films. From the 10 to 40 mol% Fe-doped thin films, it showed both Fe^{2+} and Fe^{3+} was detected while 80 and 100 mol% showed only the presence of Fe^{2+}. Co^{2+} was present in all Co-doped thin films while Ni^{2+} and Ni^{3+} were observed in all Ni-doped thin films. The EDX analyses showed that the dopants were lower than their theoretical values. The FESEM and the 2D AFM analyses showed all the Fe- and Co-doped thin films had a granular morphology from the top view while the 3D AFM analyses showed the present of

standing nanorod arrays. However, for Ni-doped thin films a transition from granular to flake morphology were observed from 40 mol% Ni-doped onwards. The optical properties of the thin films were analyzed using UV-Vis spectroscopy where three band gaps at 1.60, 1.90 and 2.30 eV were determined. The PEC studies showed at the overpotential of 0.6 V that the 10 mol% Co-doped thin film gave highest photocurrent density of 2.497 mA/cm^2 followed by the 40 mol% Fe-doped and 10 mol% Ni-doped thin film at 1.645 mA/cm^2 and 1.560 mA/cm^2, respectively.
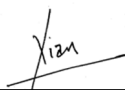
ACKNOWLEDGEMENT

APPROVAL SHEET

This project report entitled "**FABRICATION AND CHARACTERIZATION OF MIXED METAL SULFIDE THIN FILM FOR PHOTOELECTROCHEMICAL APPLICATION**" was prepared by KELVIN LAU CHING and submitted as partial fulfillment of the requirements for the degree of Bachelor of Science (Hons) in Chemistry at Universiti Tunku Abdul Rahman,

Approved by:

_____
(Dr. Ooi Mei Lee)
Date: 28 September 2020
Supervisor
Department of Chemical Science
Faculty of Science
Universiti Tunku Abdul Rahman

_____
(Dr. Ooi Zhong Xian)
Date: 28 September 2020
Co-supervisor
Department of Chemical Science
Faculty of Science
Universiti Tunku Abdul Rahman

_____
(Prof. Richard Wong Chee Seng)
Date: 28 September 2020
External co-supervisor
Department of Chemistry
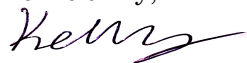Faculty of Science
University of Malaya

Date: 28 September 2020

SUBMISSION OF DISSERTATION

It is hereby certified that **_Kelvin Lau Ching_** (ID No: **_17ADM06342_**) has completed this dissertation entitled "_FABRICATION AND CHARACTERIZATION OF MIXED METAL SULFIDE THIN FILMS FOR PHOTOELECTROCHEMICAL APPLICATION_" under the supervision of Dr. Ooi Mei Lee (Supervisor) from the Department of Chemical Science, Faculty of Science , and Dr. Ooi Zhong Xian (Co-Supervisor)* from the Department of Chemical Science, Faculty of Science.

I understand that University will upload softcopy of my dissertation in pdf format into UTAR Institutional Repository, which may be made accessible to UTAR community and public.

Yours truly,

_____

(_Kelvin Lau Ching_)

DECLARATION

I hereby declare that the project report is based on my original work except for quotations and citations which have been duly acknowledged. I also declare that it has not been previously or concurrently submitted for any other degree at UTAR or other institutions.

Kelvin

_____

KELVIN LAU CHING

Date: _____ 28 SEPTEMBER 2020 _____

TABLE OF CONTENT

LIST OF TABLES

LIST OF FIGURES

LIST OF ABBREVIATIONS

AACVD	Aerosol-Assisted Chemical Vapor Deposition
AFM	Atomic Force Microscopy
Ar	Argon
CVD	Chemical Vapor Deposition
Co	Cobalt
Cp	Cyclopentadiene
EDX	Energy Dispersive X-ray
Eq.	Equation
Fe	Iron
FT-IR	Fourier-transform infrared
FTO	Fluorine-doped Tin Oxide
Ni	Nickel
NMR	Nuclear Magnetic Resonance
PEC	Photoelectrochemical
SCFH	Standard Cubic Feet per Hour
S	Sulfur
TGA	Thermogravimetric
W	Tungsten
XPS	X-ray Photoelectron Spectroscopy
XRD	X-ray Diffraction

CHAPTER 1

INTRODUCTION

1.1 Introduction

The gradual increase of world's population over the years had caused energy demands to be increased as well. Most of the countries rely heavily on non-renewable energy due to the fact that most of these types on energy are easy to be extracted (Osterloh and Parkinson, 2011). Combustion of fossil fuels cause increasing in concentration of CO_2 gas in atmosphere which leads to green house effect thus resulting in climate change in Earth's atmosphere (Habisreutinger, Schmidt-Mende and Stolarczyk, 2013). In addition, combustion of carbon based non-renewable energy causes pollution such as emission of sulfur dioxide which may eventually cause acid rain as well as cause respiratory problem to human. The usage of carbon based non-renewable energy must be reduced in order to minimize the negative impact on the Earth's climate. Thus, to overcome these problems an alternative energy such as hydrogen energy can be used. Hydrogen as a source of energy does not emits pollutants when undergoing combustion with oxygen as the by-product is water. The sources of hydrogen include water, hydrocarbons and organic matters (Joy, Mathew and George, 2018).

Since extracting hydrogen from hydrocarbons and organic matters causes pollution, water electrolysis or water splitting to generate hydrogen using solar energy is somehow important because solar hydrogen will play a vital role as energy as it is storable, transportable and can produce electricity by using fuel cells (Hisatomi, Kubota and Domen, 2014). Solar energy is somewhat non-polluting as well as being naturally abundant and it can overcome many energy and environmental issues. This is because solar energy that irradiates the earth surface is more than the human energy consumption (Hisatomi, Kubota and Domen, 2014). Presently, the usage of solar energy to generate hydrogen is via photovoltaic cell coupled with electrolysis. The photovoltaic cell converts solar energy into electrical energy and eventually the generated electricity is used for water electrolysis to generate hydrogen. Even though this method has zero emission of pollutants, the method is costly compared to the traditional combustions of fossil fuel (Tilley, 2019). Fortunately, there is another method to extract hydrogen using solar energy which is photoelectrochemical (PEC) water splitting (Hisatomi, Kubota and Domen, 2014; Honda and Fujishima, 1972; Kudo and Miseki, 2008). PEC water splitting has an advantage of being low-cost to generate hydrogen because unlike photovoltaic cell coupled with electrolysis, the solar energy can be directly convert into hydrogen as shown in Figure 1.1.
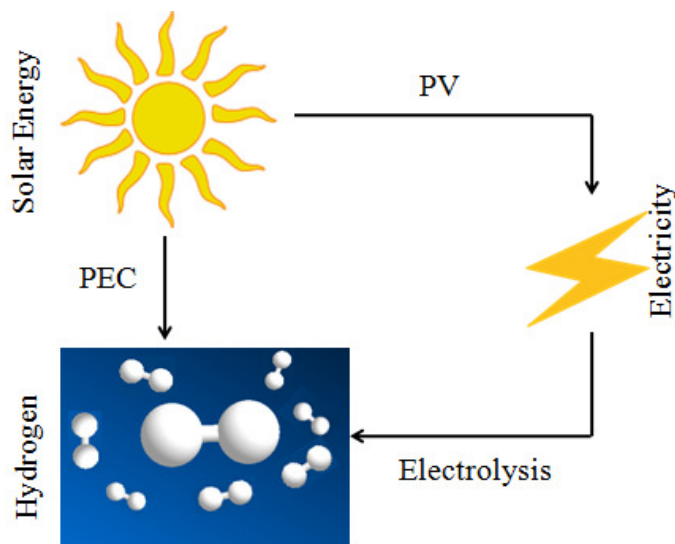
Figure 1.1: Schematic diagram of two different methods to utilize solar energy to produce hydrogen.

1.2 Problem Statements

Currently, the best material that is used to generate hydrogen *via* PEC water splitting is by using precious metals such as platinum, palladium and rhodium. This is because precious metal has the near zero hydrogen adsorption free energy. Several promising alternatives to replace these precious metals had been exploited including combination of metals, $3d$ transition metal sulfide, $3d$ transition metal nitride and $3d$ transition metal phosphides. Among them molybdenum disulfide, MoS_2, shows a promising candidate to replace precious metal for PEC water splitting as it has similar property to platinum's hydrogen adsorption free energy. However, molybdenum disulfide is not fully utilize because only the edge site showed it is hydrogen evolution reaction (HER) active

while the basal plane does not showed HER activity based on the density functional theory (DFT) (Wang et al., 2015). Moreover, preparation of high quality MoS_2 in a large area is still challenging (Li et al., 2015). The stability and conversion energy of MoS_2 can be further improved by tuning its band gap by means of doping with dopant.

1.3   Objective

The research objective of this study is to fabricate the metal-doped molybdenum sulfide thin film using the aerosol-assisted chemical vapor deposition (AACVD) with the optimized parameter from our previous studies (Lim et al., 2019). The metal dopants employed in this study are the iron triads which comprised of iron, cobalt and nickel where they are in the form of metallocene. It is worth noting that cobalt is one of the effective dopant due to its abundant electronic structure and it minimizes the distortion in the molybdenum sulfide lattice (Goncalves et al., 2019). It is interesting to investigate the effect of iron and nickel on the thin film since it has similar chemical and physical properties with cobalt (Petrucci, Cunningham and Moore., 1989). Another objective of this study is to investigate the effect of different molar percentage of dopants on the physical and optical characteristics as well as photoelectrochemical water splitting activity of the fabricated thin films.

CHAPTER 2

LITERATURE REVIEW

2.1 General

One of the alternative energy that can be used to replace fossil fuel energy is the hydrogen energy. The hydrogen energy is non-polluting because the by-product of the combustion is water. As the main source of hydrogen is from water, it is naturally abundant as the earth is made of 70% of water. Therefore, the hydrogen energy plays a vital role in a modern energy conversion as green energy for the future due to its high energy density (Hisatomi, Kubota, and Domen, 2014).

Apart from providing energy for fuel cells, hydrogen is also used in industrial ammonia synthesis. The hydrogen produced can be oxidized by burning in air or in a fuel cell to release energy and regenerate water. Currently, fossil fuels are used to generate hydrogen by steam reforming as shown in the equations (Eq.) 2.1 and 2.2.

$$CH_4 + H_2O \longrightarrow CO + 3H_2 \qquad \text{Eq. 2.1}$$

$$CO + H_2O \longrightarrow CO_2 + H_2 \qquad \text{Eq. 2.2}$$

This method still contribute the problem as CO_2 will be emitted which contribute to environmental issue such as greenhouse effect. Thus, hydrogen should be produced by a renewable energy which is solar energy. Production of hydrogen using this energy can be achieved by (Kudo and Miseki, 2009):

(i)   Water electrolysis using a solar cell

(ii)   Biomass reforming

(iii)   Photoelectrochemical (PEC) water splitting

Utilization of solar energy is needed in order to consume less energy for hydrogen generation. Solar energy can be utilized by directly using it to generate hydrogen instead of converting solar energy into electrical energy for generating hydrogen. Solar energy is fairly non-polluting apart of being naturally abundant and it can overcome many energy and environmental issues as the energy irradiates the earth surface is more than the human energy consumption (Hisatomi, Kubota, and Domen, 2014). The best way to utilize solar energy to minimize the consumption of energy for generating hydrogen is photoelectrochemical (PEC) water splitting (Fujishima, and Honda, 1972; Kudo and Miseki, 2009; Hisatomi, Kubota, and Domen, 2014).

One of the fundamental requirements to convert solar energy into hydrogen energy by the photocatalytic system is the photoresponse of the system should be optimally match with the solar spectrum. The photoexcited charge must also be efficiently separated in order to prevent recombination as well as the charge should has enough energy to carry out desired chemical reactions. Lastly

the photocatalyst must be low cost, photo-stable and chemically inert (Colmaneras et al., 2009).

2.2   Photoelectrochemical (PEC) Water Splitting

As solar energy irradiates the earth more than human consumption, it is interesting to combine solar irradiation with electrochemical water splitting. There are two approaches for water splitting process which are indirect approach and direct approach. Concurrently, indirect approach utilizes conventional solar panel to generate electricity first and use separate device for electrolysis to generate hydrogen production later. There is loss in efficiency due to additional step to generate hydrogen. Hence, single device that could performs both light absorption and water splitting has been studied and developed to replace conventional indirect approach (Roger, Shipman and Symes, 2017).

Photoelectrochemical (PEC) water splitting is one of the ways to produce hydrogen from water with the presence of sunlight. A semiconductor called photoelectrochemical material is utilized when irradiated with light to dissociate water into hydrogen and oxygen. The process involves the conversion of solar energy into chemical energy in the form of hydrogen. The pioneer for photoelectrochemical (PEC) water splitting is Fujishima and Honda in 1972 where they describe the water splitting process involves Honda-Fujishima effect using TiO_2 as their material.

This process converts solar energy also known as photon energy into chemical energy is comparable with photosynthesis process by green plants as shown in Figure 2.1. Thus, photoelectrochemical (PEC) water splitting can be considered as artificial photosynthesis because it is comparable with photosynthesis. Artificial photosynthesis is a term that refers to a scheme where solar energy is been captured and stored in the chemical bonds of a fuel.
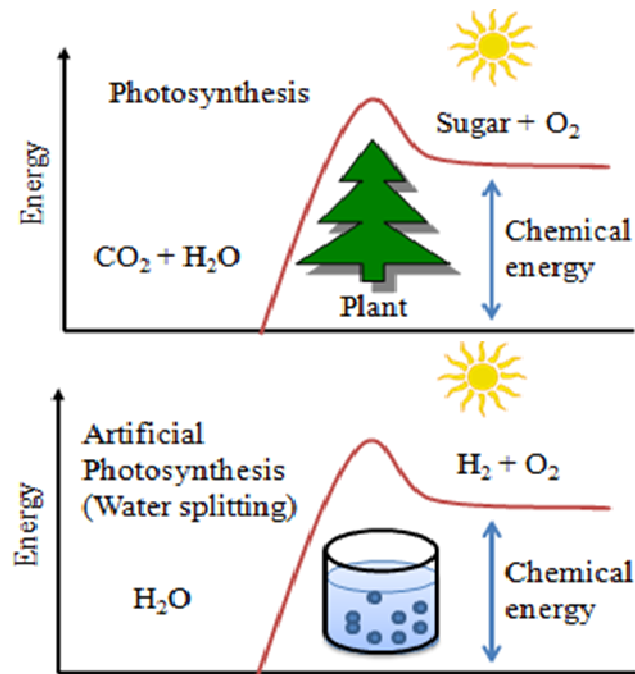
Figure 2.1: Photosynthesis and artificial photosynthesis from water splitting (Kudo and Miseki, 2009).

In order for water splitting to work, band gap energy should be more than 1.23 eV where anodic process occurs for one electrode and cathodic process for another electrode. This potential difference which is the band gap energy is the same as light radiation wavelength which is roughly 1000 nm. Thus, it is possible

to utilize visible light region apart from ultraviolet region to dissociate water into hydrogen and oxygen (Fujishima and Honda, 1972).

2.2.1 Mechanism of Photoelectrochemical (PEC) Water Splitting

Water splitting process consists of five steps which are absorption of light, electron-hole separation, migration of electron-hole, electron-hole recombination and water splitting (redox) reactions. The absorption of light (photons) by the material will causes the electron excited from the valence band and transfer to the conduction band. This process leads to the formation of electron-hole pairs. If the amount of light energy, where the energy must be larger than the band gap of the material, causes electrons and holes to be generated in the conduction band and valence band respectively. Consequently, the water splitting reaction will occur where the hydrogen ion, H^+ in water (H_2O) will be reduced into hydrogen gas (H_2) by the electrons at the conduction band whereas H_2O will be oxidized by the photogenerated holes into O_2.

The band gap width and the position of both valence band and conduction band must be taken into consideration because these are part of the factor to decide the efficiency of the PEC water splitting process. The position of the conduction band must be more negative than the H^+/H_2 reducing potential which is at 0 V while the valence band must be more positive than the O_2/H_2O oxidizing potential which is at +1.23 V. Theoretically, the minimum band gap for water

splitting is at 1.23 eV, which is corresponded to the light wavelength of 1100 nm (Kudo and Miseki, 2009; Li and Wu, 2014). Thus, the band gap should not be less than 1.23 eV. Equation 2.3 shows the band gap calculation while Figure 2.2 shows the water splitting principle.

$$\text{Band gap (eV)} = 1240/\lambda \text{ (nm)} \qquad \text{Eq. 2.3}$$
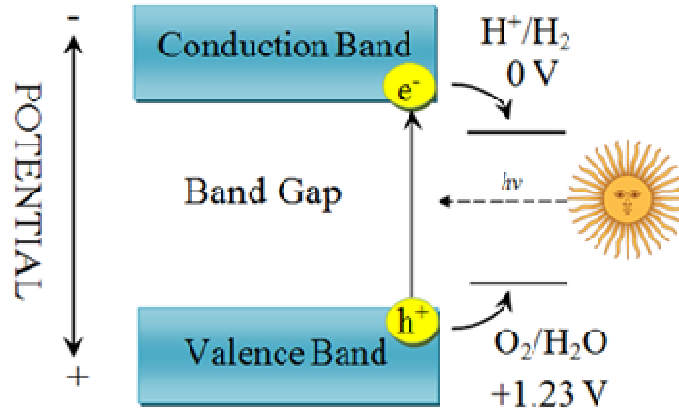
Figure 2.2: Water splitting principle using photocatalysis material.

It is noted that the band gap structure is only a thermodynamic condition but not a suitable condition for water splitting efficiency. For example material made up of cadmium sulfide, CdS, has an ideal band gap for water splitting of 2.4 eV. However, due to the absence of the hole scavenger (reducing reagent), the S^{2-} in CdS is being reduced to S while Cd^+ will be eluted out according to Equation 2.4. This reaction is known as photocorrosion (Pleskov and Gurevich, 1986).

$$CdS + 2h^+ \longrightarrow Cd^{2+} + S \qquad \text{Eq. 2.4}$$

Moreover, the morphology changes also would affect the HER activity because morphology is linked to the number of surface active sites for adsorption of molecules onto the surface of semiconductor. Hence, designing a material that has suitable band gap as well as having a suitable morphology is necessary to design a photocatalyst with high efficiency for efficient water splitting process (Kudo and Miseki, 2009).

2.2.2 Materials for Semiconductor Photocatalyst

Materials are crucial when constructing photocatalyst semiconductor as different materials will gives different results for water splitting. The materials used for photocatalysts must be able to absorb light to enable electron-hole separation which eventually led to the electron-hole migration to the electrolyte solution for water splitting (redox) reactions.

Small band gap of semiconductor is necessary to absorb wide absorption spectral range so that the water splitting process is efficient (Jaafar et al., 2017). As mentioned previously, the position of the valence band (VB) and conduction band (CB) must overlap the redox potential for water splitting photocatalytic reaction. Water splitting reaction is similar to the photosynthesis process because both of these reactions are uphill reactions (Kudo and Miseki, 2008; Li and Wu, 2014). That is why the photocatalytic water splitting is also known as artificial photosynthesis. This implies that this reaction is uphill thermodynamically and

Gibbs free energy of 237 kJ/mol is necessary to initiate the reaction. The material should have at least minimum band gap energy of 1.23 eV as well as having the position of CB to be more negative than the reducing potential of H^+/H_2 while the position of VB needs to be more positive than oxidizing potential of O_2/H_2O as shown in Figure 2.3 (Hisatomi, Kubota and Domain, 2014).
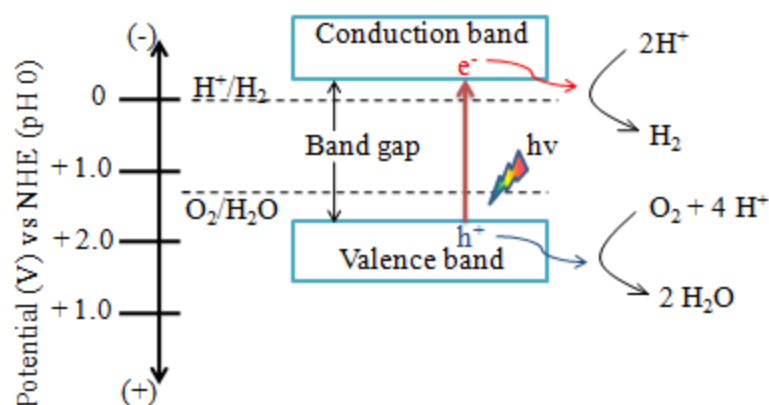
Figure 2.3: Energy diagram for photocatalytic water splitting ((Hisatomi, Kubota and Domen, 2014).

Despite having an ideal condition for efficient water splitting process different material may possess different charge recombination rate where high charge recombination may hinder the water splitting process efficiency. Therefore, material with high charge mobility and long diffusion length must be taken into consideration to have a low rate of charge recombination (Li and Wu, 2015). Generally, charge mobility is defined as drift velocity of the charge carrier (cm/s) per unit of applied electrical field (V/cm) (Tsutsui et al., 2016). High mobility in semiconductor is desirable as it allows faster process and energy efficient by reducing process time (Tsutsui et al., 2016; Schweicher et al., 2014; Sirringhaus,

2014). This attribute is not only important parameter for electronic circuits but also can give a large positive impact in hydrogen generation in PEC water splitting process. As for charge carrier diffusion length, a long carrier charge diffusion length is desirable. Charge (electrons and holes) carrier diffusion length is defined by the average distance the charge move throughout the semiconductor (Hodes and Kamat, 2015).

Besides, the material should have good photocatalytic activity toward water redox reaction to reduce overpotential. The material must also need to be stable in electrolyte in order to meet global demands for practical applications. Last but not least, it must be sustainable whereby the materials employed should be earth abundant, low cost and environmental friendly.

2.2.3 Elements that Construct the Materials for Semiconductor Photocatalyst

As shown in Figure 2.4, elements that are used in constructing the photocatalyst in the semiconductor can be classified into four groups:

i)   Elements for constructing crystal structure and energy structure

ii)   Elements for constructing crystal structure

iii)   Elements for forming impurity levels as dopants

iv)   Elements as co-catalyst

Metal oxide, sulfide and nitride composed of d^0 and d^{10} configuration metal cations. The conduction bands for d^0 and d^{10} for the metals consist of d and sp orbitals respectively. As for valence band, metal oxides, sulfide and nitride usually consist of O $2p$, S $3p$ and N $2p$ orbitals respectively. These are the elements that are used to form crystal structure and energy structure semiconductor.

Alkali and alkaline earth metals can only build crystal structure but unable to form energy structure as there are no band formation when using these metals. Partially filled d obitals transition metals such as Cr^{3+}, Ni^{2+} and Rh^{3+} forms can act as dopants for native metal cations. They are function as recombination centers between photogenerated holes and electrons. Apart from that, they also play an important function as visible light absorber. Recombination of H_2 and O_2 into H_2O must be suppressed in water splitting process. Thus, co-catalyst such as Au (Bamwenda et al., 1995; Iwase, Kato and Kudo, 2006), NiO (Domen et al., 1980) and RuO_2 (Kawai and Sakata, 1980) play an important role to minimize the recombination of H_2 and O_2 as the back reaction to form water is an uphill reaction.

Figure 2.4: Elements that build photocatalysts (Kudo and Miseki, 2008).

2.3 Typical Materials for Semiconductor Photocatalyst

Several materials have been used in constructing semiconductor photocatalyst. Different materials have their own advantages and weaknesses for PEC water splitting applications. The materials are categorized into two groups, which are (monometallic thin films) single metal and mixed metals.

2.3.1 Monometallic Thin Films

The earliest single metal semiconductor photocatalyst is TiO_2, which was developed by Fujishima and Honda in 1972. It has a band gap of 3.2 eV and 3.0 eV for anatase and rutile phase, respectively. This material is non-toxic with high abundance and stable under extreme conditions. Despite of having excellent features, TiO_2 has a wide band gap and consequently it is only able to absorb the ultraviolet region of the electromagnetic spectrum. Thus, this has caused this material to be inefficient for practical applications despite of having other excellent features.

Another material that is used as semiconductor photocatalyst is Fe_2O_3 with a suitable band gap ranging from 1.9 – 2.3 eV, depending on the phase that is formed (Young et al., 2013). This shows improvement when compared to TiO_2. For example, a study by Young showed that hematite (Fe_2O_3 in hexagonal phase) had a band gap of 2.1 eV whereas TiO_2 usually have band gap of 3.2 eV. The band gap value is much closer to the water splitting band gap thus the Fe_2O_3 is a more ideal semiconductor photocatalyst for water splitting when compare to TiO_2 (Young et al., 2013). Apart of having a band gap that is much closer to the water splitting band gap (1.23 eV), this material is also earth-abundant, non-toxic and photochemically stable. The weaknesses for this material is it has short hole diffusion length, low hole charge mobility and poor water redox reaction which

leads to high recombination rate of evolved H_2 and O_2 (Katz et al., 2012; Sivula, Le Formal and Gratzel, 2011).

Material that has an ideal band gap for water splitting is CdS where the band gap is 2.4 eV (Chen et al., 2012). However, CdS easily undergo photocorrosion because it has low oxidation kinetics that leads to the holes accumulation (Li and Wu, 2015; Chen et al., 2012; Kudo and Miseki, 2008). The equation (Eq.) 2.5 had shown that the Cd^{2+} has been eluted by photogenerated holes (h^+).

$$CdS + 2h^+ \longrightarrow Cd^{2+} + S \qquad \text{Eq. 2.5}$$
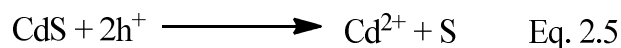
Transition metal dichalcogenides (TMDC's), most notably tungsten disulfide and molybdenum disulfide, have been long used for interest as they are earth-abundant in the form of molybdenite and tungstenite. The materials have been known for a wide variety of applications such as optoelectronics, spintronics, energy storage, lubrication, and catalysis (Tedstone, Lewis and O'Brien, 2016).

MoS_2 has recently gained a lot of interest by researchers as it offers many advantages because they are earth abundant, have an ideal band gap of $1.8 - 1.9$ eV for direct band gap in 2D monolayer and indirect band gap of 1.2 eV for bulk material, high stability, low cost and high hydrogen generation activities (Yu et al., 2016; Rahman and Purgon, 2017). Moreover, MoS_2 has near zero hydrogen adsorption free energy which is similar to palladium semiconductor photocatalyst analogous (Wang et al, 2015). It is noted that concurrently the best material for water splitting is palladium. Due to its high cost and low abundant the best

alternative which is the MoS_2 should be considered. This material can be further improved as the number of active sites is proportional to the hydrogen evolution reaction (HER) (Yu et al., 2016; Li and Zhu, 2015).

It was noticed that the process of hydrodesulfurization, CO_2 reduction and hydrogen evolution tends to occur at the sheets' edges of 2D TMDC's while at the basal plane the processes is close to none. (Wang et al, 2015). The shape is based on the Wulff-theorem where the MoS_2 edges were referred to as the $(\bar{1}010)$ as the S edge, $(10\bar{1}0)$ as the Mo edge and (0001) as the basal plane (Lauritsen et al., 2007; Lauritsen et al., 2015).

In order to compensate this problem and to further improve HER, band gap tuning can be done by changing the size of nanostructure, its dimension and adopt a crystal structure. Doping with other metal which will produce mixed metals can be employed in order to achieve these. The parent structure of TMDC's as well as its morphology can be modified by doping method. This is because doping is another strategy to modify the basal plane thus increasing the density of active sites.

2.3.2   Mixed Metals

Mixed-metals semiconductor photocatalysts have advantages of being more stable and more efficient in photocatalytic activity when compare to the single material. This may due to that alteration of physical, chemical and optical properties of the semiconductors' material.

Mixed-metals semiconductor photocatalysts can be produced using doping method. Doping is defined as introduction of impurities into the semiconductor. This will alter the morphologies as well as photocatalyst properties when compared to its parent material. Different mol percentage of dopant gives rise different morphology as well as the number of active sites (Tedstone et al., 2014; Lewis et al., 2015; Al-Dulaimi et al., 2016). Figures 2.5 and 2.6 demonstrated that the different percentage of dopants that had altered its parent thin film's morphology which are the molybdenum disulfide (MoS_2) and tungsten disulfide (WS_2).

$Mo_{0.7}W_{0.3}S_2$ $Mo_{0.5}W_{0.5}S_2$
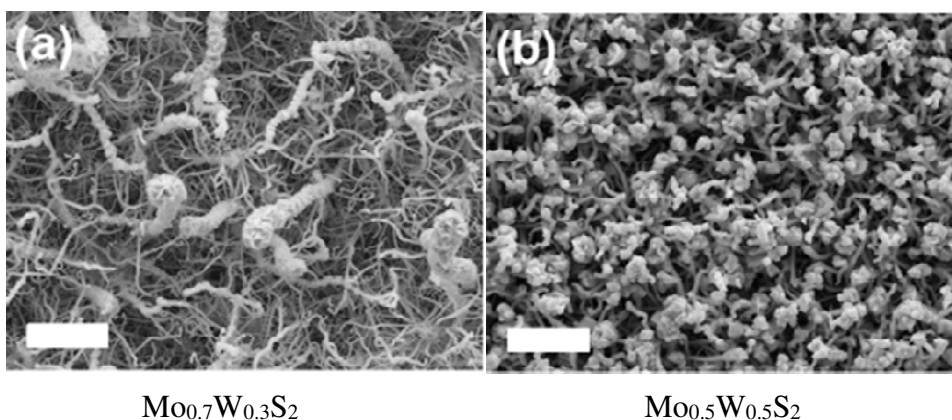
Figure 2.5: W-doped MoS_2 with different mol percentage of dopant (Tedstone et al., 2014).

MoS_2 $Mo_{0.9821}Re_{0.0179}S_2$ $Mo_{0.982}Re_{0.018}S_2$

$Mo_{0.964}Re_{0.036}S_2$ $Mo_{0.9375}Re_{0.0625}S_2$ ReS_2
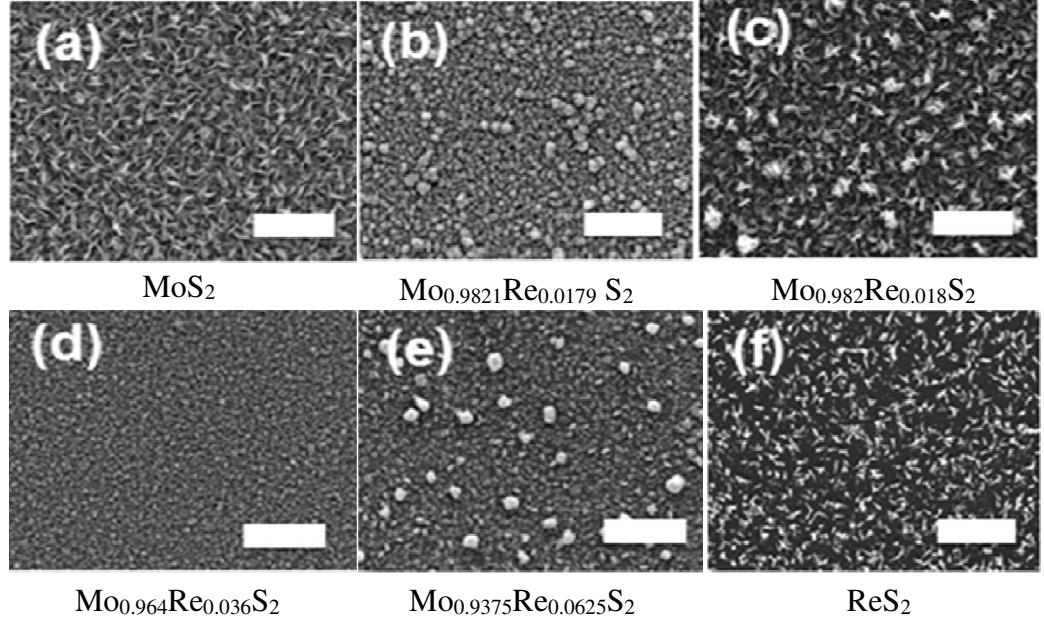
Figure 2.6: MoS_2 doped with Re in different mol percentage (Al-Dulaimi et al., 2016).

Incorporation of impurities can increase the spectral response into the visible range (Ratova et al., 2014; Kudo and Miseki, 2009). This is because new electron band will be created above the valence band within the band gap of the parent material. However, different dopants may give different results. Hence, optimizing the mol percentage or ratio of dopants to be incorporated into the parent material is important. Examples are shown in Table 2.1 where TiO_2 are doped with different amount of N.

Table 2.1: Effect of doping on band gap (Ratova et al., 2014).

Sample ID	Band-gap, eV	Band-gap shift (compared to TiO_2)
TiO_2	3.15	-
TiO_2 + Mo	3.00	- 0.15
N1	3.22	+ 0.07
N3	3.22	+ 0.07
N5	3.20	+ 0.05
N7	3.14	- 0.01
N10	3.08	- 0.07
MoN1	3.09	- 0.06
MoN3	3.09	- 0.06
MoN5	3.05	- 0.10
MoN7	3.04	- 0.11
MoN10	3.07	- 0.08

Naturally occurring molybdenite contains impurities which is similar with the transition metal dichalcogenides (TMDC's) thin film doped with other materials. Thus, it must be noted that doping may not be suitable in certain applications, so optimization of different mol percentage of dopants is very crucial to synthesize large crystals, thin layers and suspensions of a few- or monolayer of TMDCs with controlled composition (Tedstone, Lewis and O'Brien, 2016). This is because optimum amount of dopants will give desirable characteristics for its potential applications as it may induce vacancies, defects and as mentioned before, alter the parent structure. Thus, the product synthesized will be more stable and possess higher efficiency.

The metal dopants can play the role as the co-catalyst, which contribute to improve the efficiency of charge separation and transportation which eventually increase the reactivity and stability of the semiconductor photocatalysts (Kuo et al., 2017). Metals, especially noble metal are usually used as co-catalyst to

enhance the photocatalytic activity due to its promotional effect on redox reaction. The surface of the semiconductor photocatalyst is modified by the metal cocatalyst where the photogenerated electron will be transferred from the semiconductor to the metal co-catalyst and being trapped over there. As a result, the adsorption and activation energy for the redox reaction with O_2 will be promoted (Kuo et al., 2017). Without the involvement of co-catalysts, "non-selective" reaction such as recombination of H_2O in water splitting will be favored for the redox reaction.
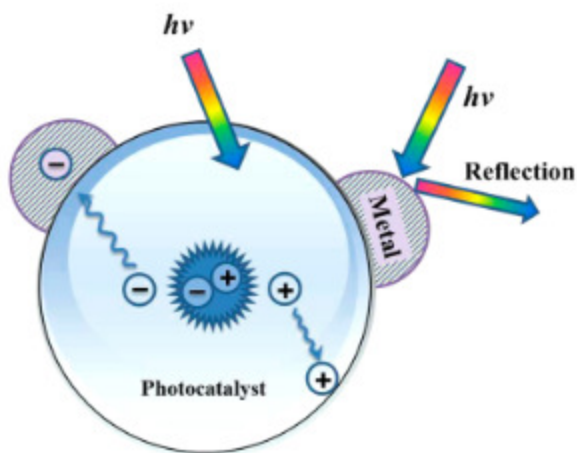
Figure 2.7: Schematic description of photocatalytic processes for metal loaded photocatalyst (Kuo et al., 2017).

2.3.3   The Iron Triads (Fe, Co and Ni) as Dopant

Due to its similarity in chemical and physical properties of iron (Fe), cobalt (Co) and nickel (Ni), these elements are group together which is known as the iron triads (Petrucci, Cunningham and Moore, 1989). The magnetic properties of these elements can create large magnetic pole because they have unpaired electron. It is because of the magnetic properties that they are commonly used as dopant (Petrucci, Cunningham and Moore, 1989). Despite their similarities, they are exploited differently in nature and industry.

The usage of Fe as dopant was showed by Wang using density functional theory (DFT). It was observed that the carrier concentration of MoS_2 can be further increased by doping 0.5 atomic percentage of iron (Fe) into the lattice structure (Wang et al., 2014). The bandgap of the MoS_2 does not change but there is additional feature at 1.2 eV.

The density functional theory (DFT) calculation by Ma and Wang have been studied for Fe-doped MoS_2 and concluded that iron is capable to increase the catalytic activity of basal plane of MoS_2 monolayer for reduction of carbon monoxide catalyst (Ma et al., 2015). The edge of the sheets is known to be photocatalytically active as there is more concentration of active sites. The active sites can be further increase at the basal plane by creating sulfur vacancies on the catalytically active site. Based on the literature, iron is also capable to increase the active sites while maintain the stability with respect to diffusion of Fe at room

temperature. An example by Wang is shown in Figure 2.8 to compare the hydrogen free adsorption energy between the pristine MoS_2 and Fe-doped MoS_2 from the DFT calculation. The free energy, ΔG, should be closed to zero indicate that the hydrogen is readily absorbed to the Mo- or S-site. The adsorbed hydrogen is circled in red in the figure. It is noted that the Mo edge is deactivated from the hydrogen adsorption based on the figure after doping. However, the overall photocatalytic activity of Fe-doped MoS_2 can achieve 2.3 mA/cm^2 at 300 mV which is higher compare to pristine MoS_2 where it only achieved 0.2 mA/cm^2 at 300 mV (Wang et al., 2014).
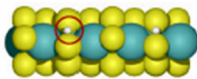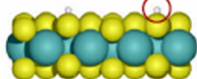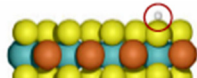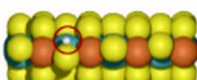
MoS_2 catalyst	Edge	Structure	ΔG_H (eV)
Pristine	Mo-edge		0.06
	S-edge		-0.45
Fe-doped	Mo-edge		0.48
	S-edge		0.04

Figure 2.8: Edge structures and the hydrogen adsorption free energy. The hydrogen adsorbed is circled in the red (Wang et al., 2014).

Co-doped MoS_2 has been reported and was used as hydrodesulfurization catalysts (Deepak et al., 2011). Besides, Peng et al. (2015) reported that the Co-doped MoS_2 nanoparticle of 30-40 nm size is used as catalyst for the conversion of CO_2 to methanol. The atomic percentage of 33 % for cobalt with respect to

molybdenum had showed the best catalytic properties as the band gap of the material was 1.41 eV which matched the reduction potential of CO_2. Co-doped MoS_2 is able to enhance the sunlight harvesting. A study had shown that the hollow structure of $CoMoS_3$ and $CoMoS_4$ possess high curvature and therefore these materials consist higher density of exposed active site (Yu et al., 2016). Thus, they are highly effective catalyst for hydrogen evolution reaction (HER).

Last but not least, nickel (Ni) also shows a promotional effect for Ni-doped amorphous MoS_3. Similar to Fe and Co, Ni also shows capability of promoting MoS_3 films growth, resulting a high surface area and a higher catalyst loading (Merki et al., 2012). Thus, it is also a highly effective HER catalyst. It should be highlighted that the MoS_3 films used in this study is amorphous instead of crystalline material. So, it is proposed that, if crystalline MoS_2 is being used the HER activity could be more efficient as the crystalline parent material has more active site as compared to amorphous MoS_2.

2.3.4 Heterostructured Materials

Heterostructured material is a material consists of two or more constituent materials that have different physical and chemical properties. When two constituent materials combine it may form a material that may have different properties when compare to the individual constituent material. Therefore, instead of forming a pure semiconductor thin film, heterostructured material could be formed. The lifetime of the photoexcited charge carriers may be prolonged and

the photoresposive range could be broadened when composite material is used. This is because combination of electronic structure can alter the pure material properties, thus, improves the conversion and yield (Liu et al., 2010). It was noting that the terms composite materials and heterostructure materials is not strictly divided.

Mumtaz and coworker in 2016 had demonstrated that the photocatalytic activity of V_2O_5/TiO_2 nanorod was better compare to the TiO_2 nanorod. In the study, that had made comparisons of photocatalytic activity between TiO_2, solution deposition of V_2O_5/TiO_2 and flame oxidation of V_2O_5/TiO_2 as shown in Figure 2.9. From the figure, the composite which is the V_2O_5/TiO_2 generally has a better photocatalytic activity compare to the TiO_2. The TiO_2, solution deposition of V_2O_5/TiO_2 and flame oxidation of V_2O_5/TiO_2 that was hydrothermal synthesis have an onset potential of -0.62 V, -0.09 V and -0.36 V. It was also observed that after the solution deposition of V_2O_5/TiO_2 was annealed using methane and propane mixed blue flame at >1000 $^{\circ}$C for 1 minute to produce flame oxidation of V_2O_5/TiO_2 it had photocurrent density of 7.89 $\mu A/cm^2$ at 0 V vs Ag/AgCl which is higher that TiO_2 nanorod where the photocurrent density is 5.60 $\mu A/cm^2$ at 0V vs Ag/AgCl (Mumtaz et al., 2016).
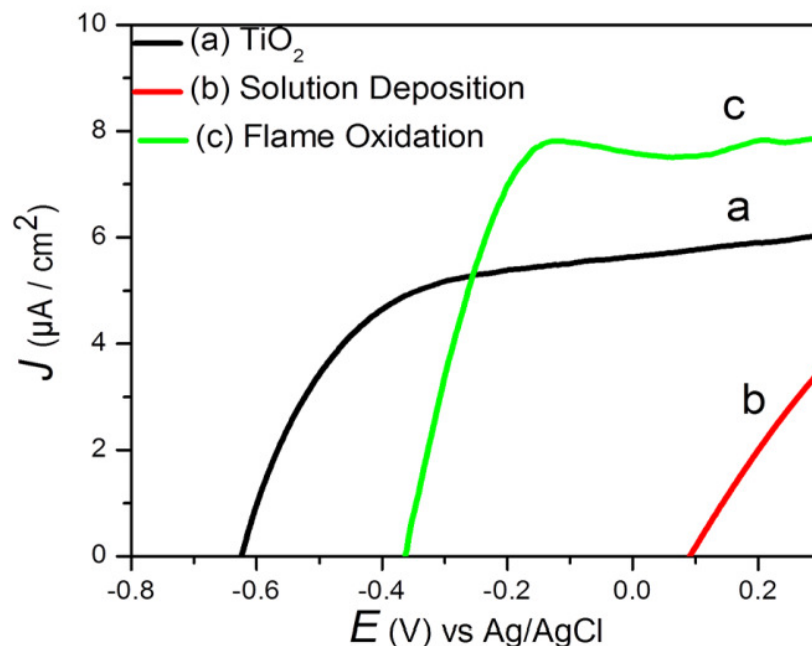
Figure 2.9: Photocurrent density of (a) TiO_2 (b) solution deposition of V_2O_5/TiO_2 and (c) flame oxidation V_2O_5/TiO_2 (Mumtaz et al., 2016).

Another type of heterostructured material reported by the same group in 2016 is the core-shell materials that also shown a significant impact on the PEC water splitting studies. The core-shell vanadium modified titania@β-indium(III) sulfide (V-TiO_2@β-In_2S_3) has demonstrated a better photocatalytic activity compare to the TiO_2 as shown in Figure 2.9. It was observed in Figure 2.9 (a) that V-TiO_2 has photocurrent density of 0.60 mA/cm^2 at 0.5 V vs Ag/AgCl which are higher than the TiO_2 photocurrent density of 0.55mA/cm^2 in light condition (depicted as L in the figure). The chronoamperometric curves in Figure 2.10 (a) showed both of the thin films for V-TiO_2 and TiO_2 had a stable photoresponse. They had also evaluated the different loading time of TiO_2@β-In_2S_3 on the photocurrent density. It was observed in Figure 2.10 (b) that the TiO_2@β-In_2S_3 with a loading time of 10, 20 and 30 minutes had photocurrent density of 0.92,

0.90 and 1.05 mA/cm^2 at 0.5 V vs Ag/AgCl. The V-TiO$_2$@β-In$_2$S$_3$ had the photocurrent density of 1.42 mA/cm^2 at 0.5 V vs Ag/AgCl. The reason why composite material has a better photocatalytic activity is due to the efficient charge transfer across the interfaces in the semiconductor as shown in Figure 2.10.

The Figure 2.11 (a) represents the core-shell (bilayer) strategy, which is similar to TiO$_2$@β-In$_2$S$_3$. As the light was irradiates on the semiconductor, electron excitation from valence band to conduction band occurs in both layers. The excited electron from the second layer of β-In$_2$S$_3$ was transferred to the conduction band in the first layer of TiO$_2$. The charge transfer mechanism for V-TiO$_2$@β-In$_2$S$_3$ was shown in Figure 2.11 (b) where V acts as the recombination center that can quench the holes of the second layer. The complete Z-scheme for V-TiO$_2$@β-In$_2$S$_3$ is shown in Figure 2.11 (c) (Mumtaz et al., 2016).
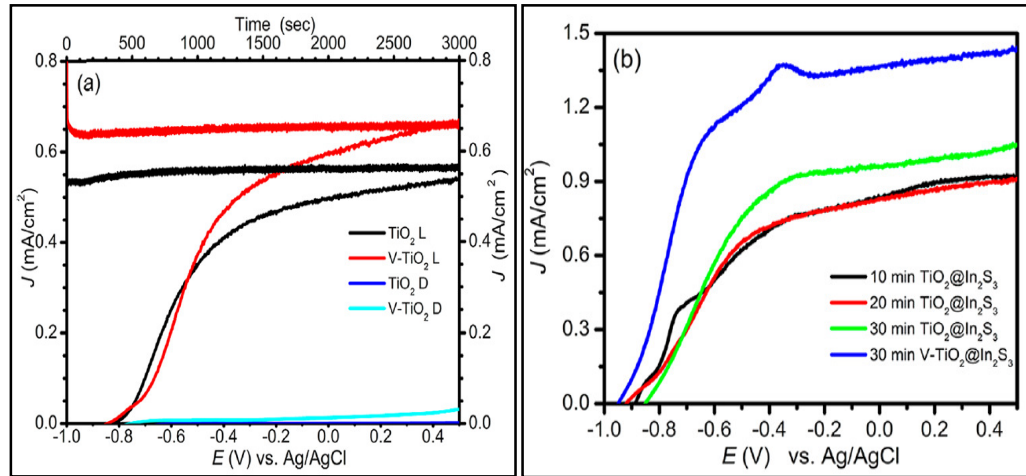
Figure 2.10: (a) J-V curve at the left bottom scale with TiO$_2$ and V-TiO$_2$ in dark (D) and light (L) conditions as well as chronoamperometric curves (CA) in light (L) conditions, (b) J-V curve for TiO$_2$@β-In$_2$S$_3$ with different duration of loading times and V- TiO$_2$@β-In$_2$S$_3$ (Mumtaz et al., 2016).
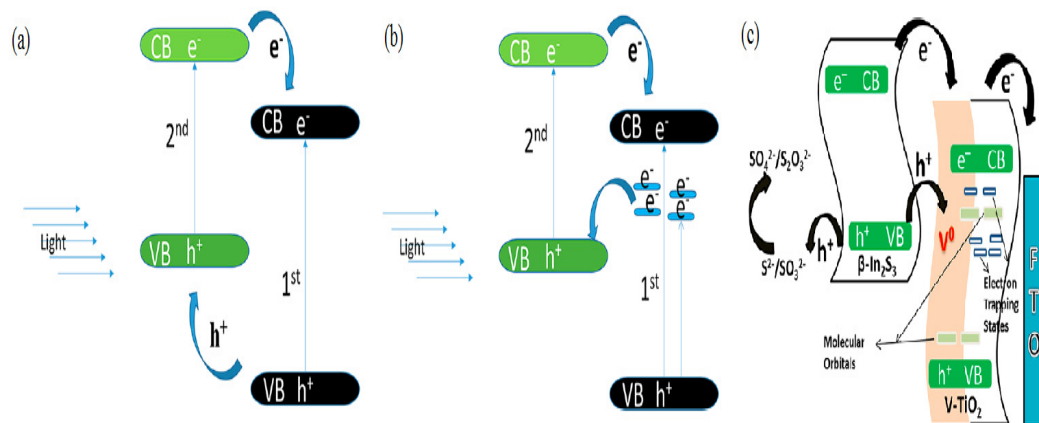
Figure 2.11: Z-scheme for heterostructured materials (a) bilayer (b) bilayer with surface modification for first layer and (c) V-TiO$_2$@β-In$_2$S$_3$ (Mumtaz et al., 2016).

2.4 Fabrication of Monolayer MX$_2$ Thin Film (M = Metal; X = O, S or NO)

There are two types of fabrication of monolayer thin film which are bottom-up method (constructive method) and top-down method (destructive method). The bottom-up method is defined as built-up of materials from atom to cluster to nanoparticles or in this case thin film. On the other hand, top-down method is a reduction from bulk material to powder and finally to thin film. There are various methods of bottom-up and top-down method (Sang et al., 2016). The difference between bottom-up method and top-down method to fabricate thin film was depicted in Figure 2.12.
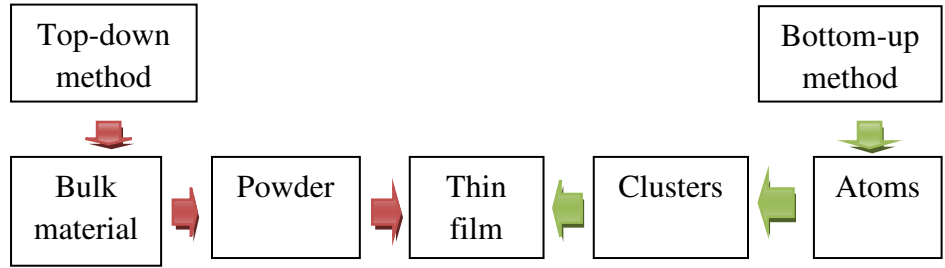
Figure 2.12: Synthesis processes of thin film (Han et al., 2017).

2.4.1   Top-Down Method

One of the top-down methods is mechanical exfoliation whereby it uses adhesive tape to create a high quality thin film. However, it can only produced films in a small scale and can only be applied in a fundamental research. Thus, it has a low cost efficiency.

Liquid exfoliation is another top-down method to produce single or multilayer 2D high quality nanosheets. The disadvantages of using this method are it is time consuming and requires high temperature to produce small scale productions.

2.4.2 Bottom-Up Method

One of the bottom-up methods for synthesizing thin film is by replacing the oxygen atom in the metal oxide thin film with sulfur atom. This method is known as oxide thin-film replacement. The thickness of the metal sulfide films is similar to the initial metal oxide films. The disadvantage of using this method is it is often difficult to synthesize thin film with mono- or bi-layer thickness (Han et al., 2016).

Chemical Vapor Deposition (CVD) method is the chemical reactions of gaseous reactants deposited on the surface of the heated substrate to fabricate thin films (Choy, 2003). The advantage of CVD method large area of thin films with controllable layer can be produced (Sang et al., 2016; Tedstone et al., 2014). CVD method has the ability to manipulate the surface morphology and crystal structure by manipulating the parameter of this technique (Choy, 2003). It should be take note that these advantages are the general advantages of CVD technique as there are variants of CVD and each variant has its own advantages and drawbacks.

Ideally, the films produced by CVD method are generally homogenous over the entire substrate to guarantee the electronic and optoelectronic properties are uniform in the devices. It is very challenging in growing uniform high quality 2D films over a large area is with small grain. As mentioned before, small grain is necessary for high efficiency catalytic activity. If the synthesis is carried out in the furnace tube, morphology may vary and the layer distributions are random which affects the uniformity of the thin films. Besides, transfer of the film from

substrates to another target one is tedious for specific application as it may contaminate or damage the synthesized films. Mass production of the films is still challenging due to sluggish growth rate and precise growth situation necessities. Therefore, condition optimization is necessary to produce a desirable film (Cai et al., 2018). In this study aerosol-assisted chemical vapor deposition is chosen mainly due to its simplicity for manipulation during fabrication of the thin film.

2.5   Overview of Aerosol Assisted Chemical Vapor Deposition (AACVD)

AACVD is a synthesis method where the substrate is deposited by one or more non-volatile precursors in a liquid-gas phase (generated ultrasonically). In other words, this method involves aerosol droplets to transport precursor with the aid of inert carrier gas. Unlike other CVD methods, the precursor is not necessarily to be volatile but partially soluble in a solvent from which the aerosol can be generated. The advantage of this method is it offers a variety of choices of precursors for high quality products at low cost. AACVD can be operated in low pressure and atmospheric pressure.

As shown in Figure 2.13, the AACVD process starts by forming aerosol droplet from precursor in a solution using a humidifier. The aerosol droplet then is transported by carrier gas typically argon gas to the reaction chamber. On reaching the chamber, the solvent evaporates due to increase in temperature

Depending on the deposition temperature, the aerosol may undergo four deposition mechanisms as shown in Figure 2.12. The first process is where the aerosol precursor droplets are sprayed directly onto a heated substrate, followed by the removal of the solvent through evaporation and decomposition of the precursor to the finished product.

The properties of 2D films depend on the size, morphology, phase, presence of interface and many more. These features can be controlled based on the parameters of AACVD process. This is because factors such as the temperature, precursor, pressure and substrate would affect the materials' growth as shown in Figure 2.14.
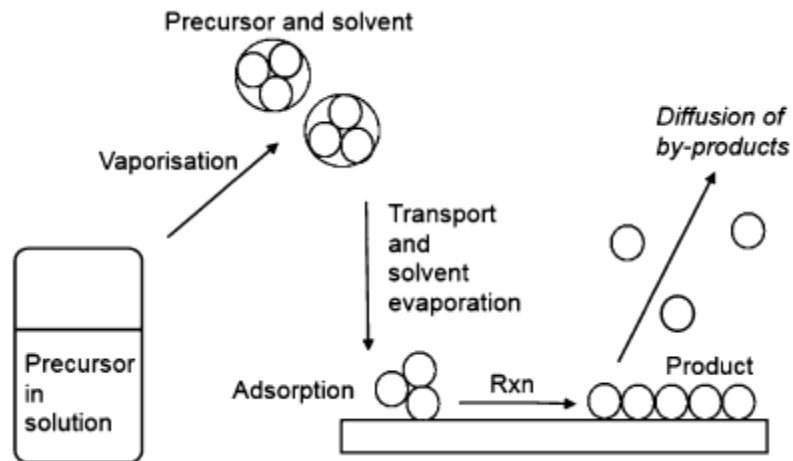
Figure 2.13: Schematic illustration of AACVD process (Knapp and Carmalt, 2016).
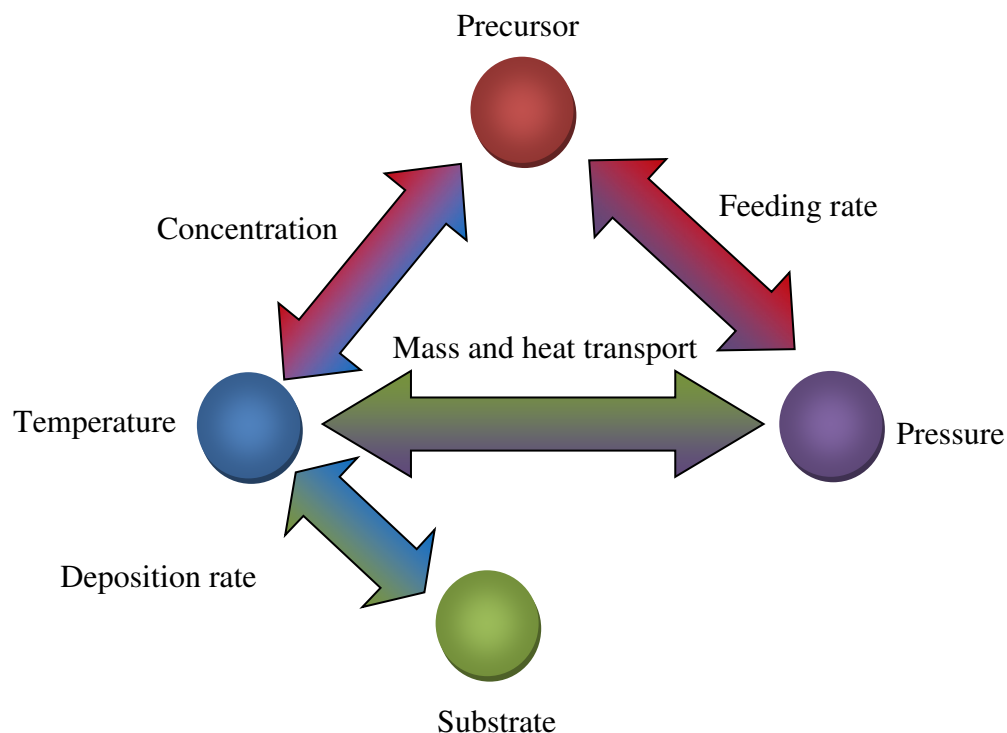
Figure 2.14: Schematic showing that the factors that have an affects on the AACVD 2D materials' growth (Cai et al., 2018).

2.5.1   Precursor for Aerosol Assisted Chemical Vapor Deposition (AACVD)

Precursors are used as reactant in the AACVD process. The precursor alteration into the targeted products can be done by thermal decomposition reactions. The carrier gas is introduced into the silicon commercial growth to allow accurate control of the molecules' number that were involved by altering or optimizing each of the precursors' flow rate as well as its partial pressure. In order to control the molecules' number one should know that 1 standard cubic centimeters per minute (sccm) is equivalent to 7.4×10^{-7} mol/s. It must be highlighted that very pure precursors are essential to avoid or at least minimize

side reactions and contamination of final product. Other methods such as chemical synthesis reactions as well as chemical transport reactions also can be applied to achieve similar result (Cai et al., 2018).

CH_4 and H_2 (gaseous sources) are frequently used as precursors for graphene deposition because the control of the flow rate can be easily manipulated so that the physical properties of the graphene can be altered. Doping of N or P atoms into graphene also can be done by using gaseous source of NH_3 or PH_4.

The growth of transition metal dichalcogenides are usually using solid source. The sources of metal are from transition metal oxides or chlorides or metal foil while sulfur or selenium can be used directly as its own source. These types of precursor need precise deposition temperature as they are very sensitive to temperature. Thus, optimization of AACVD condition is a challenge for TMDC's growth.

2.5.2 Temperature

The deposition temperature in AACVD process can influence the thin films' composition as well as its homogeneity because it affects the carrier gas flow, precursors' reaction in its gaseous form and the rate of deposition of thin film. Excellent in quality products are usually formed with high deposition temperature. The temperature in the heated zone is crucial because a minor change of temperature may largely affect the saturation pressure of gasified solid precursors eventually have an effect on the growth of TMDC thin film. Mass transport of species and vapor-solid interface reaction can also be affected by deposition temperature, thus effective reaction rate can be achieved by adjusting the temperature.

Thermodynamic process occurs when the reaction system is in high temperature while kinetic process occurs in low temperature for nucleation at the interface of solid-vapor (Cai et al., 2018). Study conducted by He et al. had shown that growth rate at solid-vapor interface would be accelerate at high temperature (He et al., 2016). While the layer thickness, number of layers and morphology of WSe_2 flakes were also affected by the growth temperature as been claimed by Liu et al (Liu et al., 2016).

2.5.3   Substrates

Apart from being a place for a material to be deposited in AACVD process, the substrate has other functions depends on the material of the substrate. The structure of the substrate can have an effect on the growth of thin films. TMDC thin films are usually grown on silicon thermal oxide, mica and polyimide substrate (Ji et al, 2013; Liu et al., 2016; Gong et al; 2017). Some metal foils such as tungsten and gold also have been used as substrate for TMDC growth (Sanne et al., 2015; Zhou et al., 2016; Zhang wt al., 2017).

A study conducted by Shi et al had shown that different facet (orientation) of the substrate results in different nucleation (morphology and particle size) of TMDC thin film growth. This is due to the different binding energy at the interface of the selected facet and the TMDC thin film causing a preferential nucleation of the thin film (Shi et al., 2015). Thus, the facet of the substrate has an effect on the nucleation or growth of thin film which will eventually lead to different morphology and particle size.

2.5.4 Pressure

Pressure in a AACVD reaction system can affect the gas flow behavior according to the ideal gas law (PV = nRT). The volume flow and gas velocity increased when using a low pressure for using the same molar flow based on the gas law equation. At the same time, the precursor concentration decreases. This results in more controllable reaction.

Some studies used low-pressure AACVD to obtain a high quality MoS_2 thin film (Yu et al., 2013). The studies are consistent with the nucleation of high quality WSe_2 by Elias et al. (2013). It was claimed that the partial pressure influences the layered WSe_2 thin film's nucleation. The nucleation at low pressure happens at the grain boundaries when using a low pressure which is more desirable due to its homogeneity and consistency. At high pressure the nucleation or growth of thin film happens randomly which cause low homogeneity (mixture of monolayer and multilayer thin film).

2.6   AACVD Growth of Thin Film

Recent studies had shown that AACVD technique has the capability to fabricate thin films as well as 2D materials. A thorough understanding on the thin film nucleation mechanism must be grasped firmly in order to improve its reproducibility for practical applications. Therefore, it is utmost important to understand the correlation of fabrication of thin films and AACVD process. Single crystal materials give precious information to investigate growth and nucleation mechanism of the thin film fabrication on a substrate. It also provides information on manipulating the properties of materials. In section 2.7, theoretical and practical approaches are discussed on how to control the properties of thin film which includes its particle size, number of layers, orientation, morphology and dopants as well as its defects.

In the early stage of the research, metal oxide precursor are reduced into suboxides (electropositive metal is more than oxides) and further reduced by reacting with chalcogenides (in gaseous phase) to form TMDC thin film on a substrate.

Cain and co-worker as well as Li and co-worker found out that a metastable nanoparticle reaction intermediate, MO_xX_y (M – Metal; O – oxygen; X – chalcogenide), function as the metal source as well as nucleation site for the fabrication of TMDC thin film (Cain et al., 2016, Li et al., 2016). The degree of

saturation plays a role to determine types of growth and nucleation mode of the materials (Cai et al., 2018).

The growth control of thin film is based on the theory of growth and nucleation of thin film in process of CVD. There is a relationship between variety of properties of thin film and the manipulation of parameters on the CVD growth process. The properties of the thin films are categorized into particle size, number of layers, orientation, morphology, dopants (doping agents), defects and quality.

2.6.1 Particle Size

Najmaei and co-worker reported that they had observed grain boundaries in MoS_2 thin film that was fabricated using CVD method (Najmaei et al., 2013). These grain boundaries could deteriorate the physical properties of the MoS_2 thin film and therefore have a negative effect on the thin film activity. For example, grain boundaries may cause scattering of charge carrier which may results in lower mobility and therefore reduce the effectiveness for the thin film practical application such as water splitting process. On the other hand, single crystal has minimum scattering due to the small amount of grain boundaries (Yan, Peng and Tour, 2014).

Based on the recent silicon-based (semiconductor) technology, it is preferable to fabricate large area of thin films. This is because materials with large

area of single crystals has more active sites for photoelectrochemical reaction, thus has shorter response time compare to single crystal samples with small area and large polycrystalline (crystals with variety of size and orientation) samples. Single crystal with small area and large polycrystalline samples may have low efficiency on the photoelectrochemical reaction process due to low amount of active. Thus, fabrication large area single crystals for recent technology are preferred for many efficient practical applications apart from water splitting process such as high efficiency electronics, optoelectronics, thermal management applications, flexible and wearable devices and many more (Cai et al., 2018).

Large single crystals growth can be achieved by decreasing the nucleation density during the fabrication of the thin film. Chen and co-worker had fabricated $MoSe_2$ thin film with single crystals size (particle size) around 2.5 mm on molten glass by using CVD method as can be seen in Figure 2.15. The molten glass was heated at high temperature which leads to the formation of smooth surface causing a small amount of nucleation sites for $MoSe_2$ growth into single crystals (Chen et al., 2017). Therefore, it can be deduced that molten substrate may promote single crystal thin film growth and nucleation mechanisms as it provides a few nucleation sites which will decreases the nucleation density.
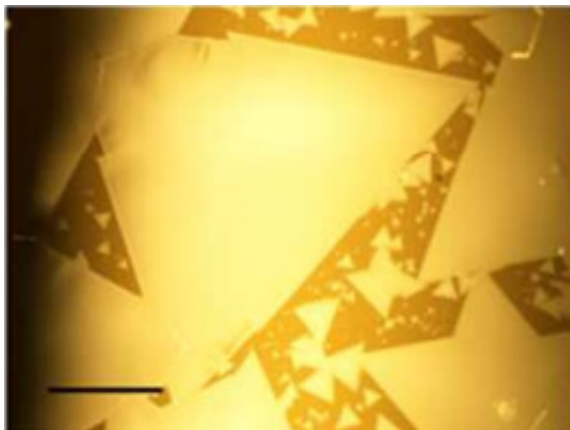
Figure 2.15: Optical image of MoSe$_2$ thin film with single crystals that was fabricated on heated molten glass at high temperature (Chen et al., 2017).

Moreover, another approach to increase the particle (single crystal) size, is by maintaining the growth and nucleation mechanism of the thin film in a long period of time. This can be achieved by decreasing the energy barrier of the reaction which was demonstrated by Gao et al. They had demonstrated this idea by fabricate large area of WS$_2$ single crystal thin film on gold (Au) substrate with resulting in a particle size in the size of millimeter point. The sulfurization process of WO$_3$ is possible due to decrease of energy barrier which was resulted from dissociation of two S atoms from S$_2$ at Au substrate's surface. Thus, a high quality of WS$_2$ crystals to be grown as shown in Figure 2.16 (Gao et al., 2015). A similar results were obtained by growing MoS$_2$ on Au foils had been shown by Shi and co-worker (Shi et al., 2015).
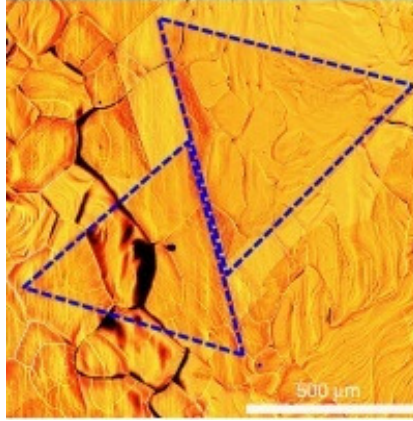
Figure 2.16: Optical image of monolayer single crystals WS$_2$ domain grown on Au foil (Gao et al., 2015).

So far, the sizes of TMDCs single crystals that are grown by CVD process are smaller compare to the crystal grapheme that are grown with the same method (Cai et al., 2018). The grain boundary formation kinetics (Cheng et al., 2015), decrease of the nucleation density, increase of growth rate (Gao et al., 2017) and maintaining long periods of growth and nucleation must be understood in order to obtain large particle size (centimeter level) with single crystal thin film in a large area.

2.6.2 Number of Layer

The interesting feature of thin film especially 2D materials (sometimes known as monolayer thin film) is their properties can be tuned by altering the number of layers. For most of materials that made up of TMDC, higher number of layers decreases the band gap. Materials with tunable band gap are vital for electronics, optoelectronics, and catalyst as well as energy applications. Studies

for TMDC materials had shown that the decrease number of layer into monolayer cause the shift of indirect band gap to direct band gap. The direct band gap material is preferred because the electron from the balance band can be directly excited into the conduction band by using photon. On the contrary, indirect band gap materials require photon and phonon to cause electron excitation from valence band to conduction band. This implies that the direct band gap material has better light absorption properties. Even though tuning the number of layers for practical usages is important, designing of multifunctional heterostructures materials are important as well because it offers new properties and novel devices for practical applications (Lan et al., 2016; Yu et al., 2014; Zhou et al., 2015: Babu et al., 2016).

The number of layer can be controlled by manipulating the temperatures in a CVD reaction system which has been shown by He et al. By using growth temperature of 750, 825 and 900 $^{\circ}$C, they obtained 1-2, 1-3 and 1-4 layers of MoSe$_2$ respectively (He et al., 2016), as shown in Figure 2.17. Similar study by Liu and co-worker also showed similar trend where the number of layer increases as the temperature increases when synthesizing WSe$_2$ (Liu et al., 2015).

Concurrently, the relationship between number of layers and CVD growth parameters are yet to be fully understood and the most established methods are based on the experiences. This implies that it is unclear whether it would work or not for other CVD systems. Further study and thorough understanding of optimization of CVD parameters is required to obtain a deep scientific insight of controlling the growth of 2D materials.
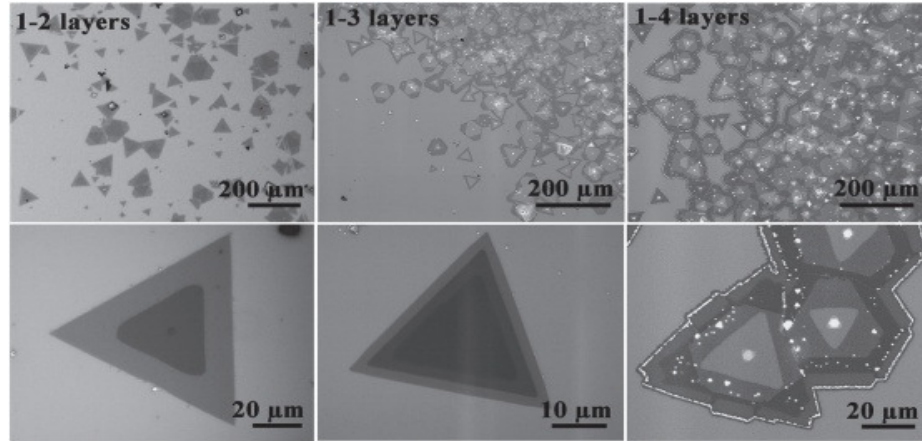
Figure 2.17: Optical images of CVD grown multilayer MoSe$_2$ with different temperatures (He et al., 2016).

2.6.3 Orientation

A good knowledge on growing large particle size (single crystal) 2D materials that is affected by the growth orientation is important in order to obtain ultrafast rate growth. The grain orientation is affected by the relative angle between the deposited material and the substrates. It was observed that the substrate was correlated to the lattice-orientation control of 2D material thin film during its growth and nucleation process. This is because the Van der Waals interactions between the deposited material and the lattice structure of the substrate would determine the preferential growth and nucleation process for fabrication of the thin film. This implies that the Van der Waals interactions would have preferential orientation for the grown thin films (Aljarb et al., 2017).

Dumcenco et al had demonstrated this idea by fabricating monolayer MoS$_2$ on the smooth surface (highly polished) sapphire substrate. The smooth

surface would limit the lattice orientations' number of sapphire substrate. Their finding which is shown in Figure 2.18 had showed that the lattice rotation angles between the grown monolayer MoS_2 and the c-plane sapphire substrate has a majority orientation of 0 and 60 $^{\circ}$ and the minority orientation of 30 and 90 $^{\circ}$. This implies that the orientations of the epitaxial growth of were influenced by the *c*-plane sapphire. Therefore, it can be concluded that the crystal growth of thin film orientation is affected by the substrate orientation (Dumcenco et al., 2015).
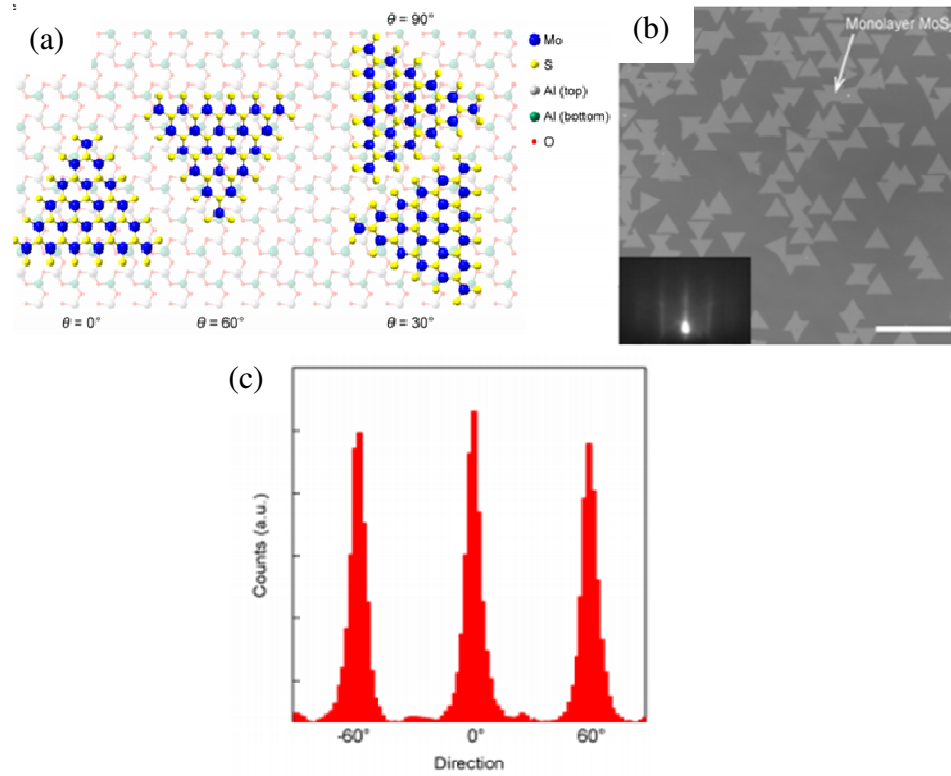
Figure 2.18: (a) Schematic drawing of top view of both monolayer MoS_2 and sapphire (c-plane) lattice orientation. (b) Optical image of monolayer MoS_2 on sapphire substrate; inset reflection high-energy electron diffraction (RHEED) pattern. (c) Histogram based on the orientation of monolayer MoS_2 on sapphire substrate in image b. (Dumcenco et al., 2015).

2.6.4 Morphology

As mentioned earlier, morphology is important because it affects the efficiency of thin films in various practical applications such as energy applications, catalysis, photocatalysis, electrochemical and photoelectrochemical reactions. For example, Ji et al. had shown the catalytic activity of monolayer MoS_2 thin film grown on mica for hydrogen evolution reaction (HER) purpose was affected by the number of exposed edge sites (Ji et al., 2016). According to the crystal growth theory, growth rate can affect the crystal shape. Studies conducted by Wang and co-workers had shown the distance between the Mo source and the substrate affect the concentration of MoO_3 deposited on the substrate as shown in Figure 2.19 (Wang et al., 2014). In Figure 2.12, the optimal distance between the Mo source and substrate should be optimized in order to have a good thin film growth and morphology with high density of active sites. This concluded that morphology control (growth rate) is important for producing a high quality thin film with high catalytic performance.

Figure 2.19: Schematic diagram of different distance between precursor and substrates that affects the concentration of MoO_3 and morphology (Wang et al., 2014).

2.6.5 Doping
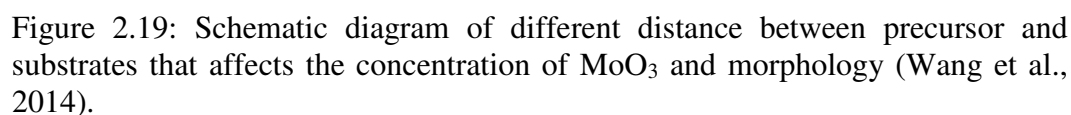
Elemental doping offers a different method for tuning the electronic structures, chemical and physical properties of thin films. Doping is the intentional addition of impurities into the thin film (in other case would be various type of semiconductor depends on its applications) to alter the properties for the purpose of enhancing its performance such as enhance the efficiency for water splitting. Various TMDC materials such as MoS_2 or $MoSe_2$, even though they may have similar atomic structures but they consist indistinguishable difference in terms of efficiency. Therefore, in order to make their efficiency more distinguishable, dopant can be added to produce the ternary TMDC thin film such as Fe-doped MoS_2 thin film. However, addition of dopants (metal or non-metal) may be challenging because inappropriate amount of dopant may lead to negative results. This implies that different amount of doping would lead to a wide variety

of results as mentioned in section 2.3.2. Other than that, the atomic concentration control is also challenging because the amount of dopant in the precursor would always be lower in the product (Tedstone et al., 2014; Lewis et al., 2015; Al-Dulaimi et al., 2016). Though very seldom reported, it is noteworthy that different amount and type of dopant may cause the changes to different properties of the thin film eg. morphology, thickness and particle size that may affected the efficiency of the thin film activity. Despite all of these, doping still gives promising approach to enhance the thin film efficiency as long as there are thorough understandings with this approach.

In order to obtain metal doped TMDC thin film, an example had been shown by Wang et al where they synthesized a homogenous monolayer $Mo_{1-x}W_xS_2$ thin film by a low pressure CVD technique. WCl_6 was used as the source of W while the source of Mo was from MoO_3. The growth temperature in this case would be at 700 $^\circ$C (optimized growth temperature from the reaction of MoO_3 with S). The ratio between the Mo and W was modified by adjusting the concentration of the MoO_3 and WCl_6 that was used (Wang et al., 2016).

Another approach to dope metal onto the thin film which was demonstrated by Ma et al is the post-treatment of thin film. They had fabricated monolayer MoS_2 thin film by conventional CVD method first. After that, the thin film was exposed to 500 V Ar plasma to removed certain amount of sulfur before quickly exposing the thin film with diselenodiphenyl (DS) to dope Se into the thin film to fabricate $MoS_{2(1-x)}Se_{2x}$ thin film (Ma et al., 2014).

2.6.6 Quality and Defects

Thin film's quality and defects are one of the important features for TMDCs growth. High quality TMDCs are needed to ensure high efficiency for practical applications (Tosun et al., 2016). It is unfortunate that defects are inevitable during the CVD growth and the defects may degrade the charge carrier mobility (Najmei et al., 2015). Conversely, controlled type and density of defects could be beneficial and desirable for applications such as catalysis (Lin et al., 2016). There is an example based on the density functional theory (DFT) calculation reported by Wang et al. where they noticed a line of S vacancies that is present in the MoS_2 thin film may cause shift of band structure from semiconductor to metal (Wang et al., 2016).

Defects in TMDC thin film are usually due to chalcogen vacancies because of their lowest formation energy. By using the density functional theory (DFT) calculation, Komsa et al. had demonstrated the mechanism on how the S vacancies were formed when the MoS_2 was exposed to electron irradiation (Komsa et al., 2012). Moreover, the correlation of the density of S vacancies and the thin film efficiency had also been studied by Qiu et al. where they had discovered that the S vacancies on the few layers MoS_2 surface function as electron donors may play important role to facilitate charge transport within the thin film (Qiu et al., 2013).

Additionally, macroscopic material properties are affected by the metal vacancies. This is because metal vacancies have deep-trap states which would affect the electron mobility more when compared to chalcogen vacancies which has shallow-trap states as mentioned by Jeong et al. Deep-trap are usually undesirable because it requires more energy to remove electron or hole from the trap to the conduction band during electron excitation (Jeong et al., 2017).

Therefore, defects could become advantages if the amount of defect is right or it also could become disadvantages for thin films fabrication if the amount of defect is too extreme. Thus, it is also important to have good knowledge on the defects for fabricating high performance thin film.

CHAPTER 3

METHODOLOGY

3.1   Materials and Reagents

Silica gel with size of 230-400 mesh that was used for chromatography was purchased from Merck, respectively. Celite was purchased from R&M and was used for filtration. Solvents used were hexane, toluene, tetrahydrofuran and Ethylene glycol dimethyl ether were AR grade and from Merck. The reagents used in this study, hexacarbonyl molybdenum, dimethyl disulfide, and dicyclopentadiene were from Merck. Hexacarbonyl molybdenum is 99% purity while the others were synthesis grade. Both ferrocene and cobaltocene were from Fluka while nickelocene was from Sigma Aldrich. All metallocene were 99% purity. The fluorine-doped tin oxide (FTO) wafer that was used as the substrate for the thin film fabrication was from Sigma Aldrich.

3.2 General Procedure

Most of the synthetic procedures were carried out using standard Schlenk technique and further manipulation were carried out inside the Vacuum Atmosphere Dribox that was equipped with Model HE 493 Dri-train under inert atmosphere of argon. All solvents used were pre-dried with activated molecular sieves (4 Å) and were degassed prior to usage. Silica gel and celite were pre-dried overnight at 140 °C before they were employed. The fluorine-doped tin oxide (FTO) substrate was immersed in acetone and then ultrasonicated for 15 minutes. Then, it was immersed in distilled water and ultrasonicated for another 15 minutes. The substrate was air dried and the conductive surface was identified with a multimeter.

3.3 Physical Measurements

^{1}H and ^{13}C NMR spectra were obtained using JEOL ECX FT NMR 400 MHz Spectrometer and the samples were prepared in deuterated benzene, C_6D_6. The chemical shifts were referenced to residual C_6H_6 in C_6D_6. IR spectra were measured in Nujol mulls on KBr (potassium bromide) salt plate. The spectra were recorded in the range of 4000-400 cm^{-1} with resolution of 16 cm^{-1} using Perkin-Elmer RX 1 Fourier Transform Infra-Red (FTIR) instrument. Thermogravimetric analysis was performed using Mettler-Toledo, TGA/STA 851e. Shimadzu UV-

2600 UV-Vis Spectrophotometer was used to analyze the fabricated thin film on FTO substrate. Scanning electron microscopy (SEM) analysis was performed using JEOL JSM-700F Field Emission SEM in secondary electron imaging (SEI) with an accelerating voltage of 2-4 kV. Energy-dispersive X-ray (EDX) spectroscopy (that were coupled with FESEM) was conducted on the same system with accelerating voltage of 20 kV using INCA detector. Samples for SEM imaging were mounted on SEM stubs using a carbon conductive adhesive tape from Agar Scientific. Atomic force microscopy (AFM) was conducted using Park Systems Atomic Force Microscope XE-70 equipped with a AFM non-contact mode cantilever with a force constant of 42 and frequency of 303.01 kHz. The scan rate and z-servo were at 0.7 Hz and 2, respectively. X-ray diffraction spectroscopy was performed using Shimadzu 6000 XRD diffractometer equipped with the X-ray tube (Cu, kα) at the voltage and current of 40.0 kV and 30.0 mA, respectively. The divergence slit, scatter slit and receiving slit were 1.0º, 1.0º and 0.3 mm, respectively. As for the XRD scanning parameter, the 2θ range was set at 10-90º where the scan speed, sampling pitch and preset time were 2º/min, 0.01º and 0.3 s, respectively. X-ray photoelectron spectroscopy (XPS) analyses were performed in Thermo Fisher Scientific K-Alpha setup using a monochromatic Al Kα$_1$ source (1593 eV) as the x-ray source at the Centralised Analytical Laboratort (CAL), University Technology Petronas (UTP). The XPS analyzer was constant analyzer energy (CAE) which was used to collect the spectra at 50.0 eV. The number of scan and the energy step size were, 50 and 0.1 eV, respectively. The

Raman spectroscopy analysis was done at 532 nm (green light) with 25 mW laser power *via* Renishaw model at University Malaya (UM).

3.4 Synthesis of Cyclopentadianylmolybddenum Tricarbonyl Dimer, [(η⁵-Cp)Mo(CO)₃]₂ (1) (Cp = cyclopentadienyl, C₅H₅)

The synthesis of **1** was according to the literature with slight modifications (Birdwhistell, Hacket and Manning, 1978). A solution of sodium cyclopentadienide in diglyme (200 mL) was prepared by treating sodium metal (0.0561 g, 2.44 mmol) with dicyclopentadiene (0.17 mL, 1.22 mmol) at 160 ℃. Molybdenum hexacarbonyl (0.6442 g, 2.44 mmol) was added when all of the metal had dissolved and the reaction mixture was refluxed for 30 minutes. The reaction mixture was allowed to cool down while stirred before proceed to next step. Hydrated iron(III) sulphate (20 g) in water (250 mL) and acetic acid (15 mL) was added into the reaction mixture. The colour of the reaction mixture was changed from yellow to purple and fine purple crystals of **1** were precipitated. The crystals were filtered off and washed with water before it was dissolved with tetrahydrofuran (THF). The solution was passed through celite to isolate excess ligand and diglyme from the desired product which is **1**. It was pumped dry to obtain fine purple crystals of **1** with 90 % yield.

3.5 Synthesis of *Bis*(η⁵-cyclopentadienyl)dimolybdenum Tetramethylthiol, [(η⁵-Cp)Mo(SMe)$_2$]$_2$ (2)

The synthesis of **2** was according to literature (King, 1963) with slight modifications. Briefly, **1** (600 mg, 1.22 mmol) was heated to reflux in toluene (30 mL) in the presence of dimethyl disulfide (1.82 mL, 20.48 mmol) for overnight with magnetic stirring. The reaction mixture was allowed to cool slowly to room temperature and was passed through silica gel column prepared in n-hexane (8.0 cm length, 2.0 cm diameter) to isolate **2** and excess ligand to give brownish-red crystal of **2** after crystallization with mass of 404 mg (66 % yield).

3.6 Deposition of Thin Films by Aerosol-assisted Chemical Vapor Deposition

0.08 g (0.159 mmol) of the precursor (**2**) and various mole ratio of ferrocene (10 %, 20 %, 40%, 80 % and 100 %) were dissolved in tetrahydrofuran (20 mL) to give solutions with varying mole ratios of (**2**) and metallocene (ferrocene, cobaltocene and nickelocene). The solutions were sonicated for five minutes using an ultrasonicator in order to make the solutions homogenous prior to carry out AACVD technique. The solution was held over a piezoelectric humidifier and the aerosol was carried by argon gas (gas flow rate: 0.5 SCFH) to the heated fluorine doped tin oxide (FTO) plate (2 cm × 1 cm) placed 6 cm from the entrance of delivery tube to the first end of the plate. The tube was housed inside

a tube furnace and the deposition temperature was set at 550 °C. The deposition time is 20 minutes for all cases.

3.7   Photoelectrochemical (PEC) Studies Measurement

The photoelectrochemical(PEC) studies was analysed using Princeton Applied Research (PAR-VersaSTAT-3) electrochemical workstation with three electrodes system where the Ag/AgCl, Pt and the thin films served as the reference electrode, counter electrode and working electrode, respectively, under inert (N_2) atmosphere. The electrolyte solution used in this project consists of 0.35 M Na_2SO_3 and 0.25 M Na_2S with pH of 12.1. The PEC studies were performed in both dark and light condition where the light intensity was set at 100 mW/cm^2 under AM 1.5 G. The measurements were conducted using a scan rate of 20 mV/s at a potential range of – 0.6 V to 0.6 V for linear sweep voltammetry (LSV). The electrochemical impedance was carried out at the starting frequency of 10 Hz and end frequency of 0.01 Hz with amplitude of 25 µA RMS. The Mott-Schottky analysis was carried out at a frequency of 100 Hz at the potential range of -2 to 1 V.

CHAPTER 4

RESULTS AND DISCUSSION

4.1 Preparation of $[(\eta^5\text{-Cp})Mo(SMe)_2]_2$ (2) as Precursor for AACVD

The complex **2** was prepared according to King's method (as mentioned in 3.2) and was authenticated in order to make sure the complex is pure before used as the precursor for Aerosol Assisted Chemical Vapor Deposition (AACVD) process for the fabrications of the thin film. Purity of complex **2** is essential to minimize the risk of contamination of unwanted impurities that may affect the properties and the photocatalytic activity of the thin films.

4.2 Authentication of $[(\eta^5\text{-Cp})Mo(SMe)_2]_2$ (2)

Bis(η^5-cyclopentadienyl)dimolybdenumtetramethylthiol, $[(\eta^5\text{-Cp})Mo(S\text{-}Me)_2]_2$ (**2**) was authenticated by using the proton and carbon nuclear magnetic resonance (^{1}H- and ^{13}C-NMR) as well as infrared spectroscopy. The thermogravimetric analysis (TGA) was also used to find out the decomposition temperature of complex **2**.

4.2.1 Nuclear Magnetic Resonance (NMR) Analysis

NMR analysis was performed to analyze the $bis(\eta^5$-cyclopentadienyl)dimolybdenumtetramethythiol, $[(\eta^5\text{-Cp})Mo(SMe)_2]_2$ (**2**). The ^1H NMR chemical shifts were referenced to residual C_6H_6 in C_6D_6 (benzene-d_6) with a reference peak at δ 7.16 ppm. The authentic sample ^1H NMR chemical shifts value was included for the comparison purpose (King, 1963).

From the ^1H NMR spectra as shown in Figure 4.1 for complex **2**, two major peaks were observed where a singlet at δ 5.19 ppm which was assigned as the $-CH_2$ group in the cyclopentadienyl ligand while another singlet at δ 1.62 ppm indicates the existence of methyl proton from $-SCH_3$. As for the ^{13}C NMR spectrum in Figure 4.2, signal at δ 90.89 ppm represents the carbon in cyclopentadienyl group while signal at δ 10.46 ppm represents the carbon in the methyl group for complex **2**. Since there are no impurities present, the synthesized complex **2** was pure and can be used for the preparation of thin film via AACVD.
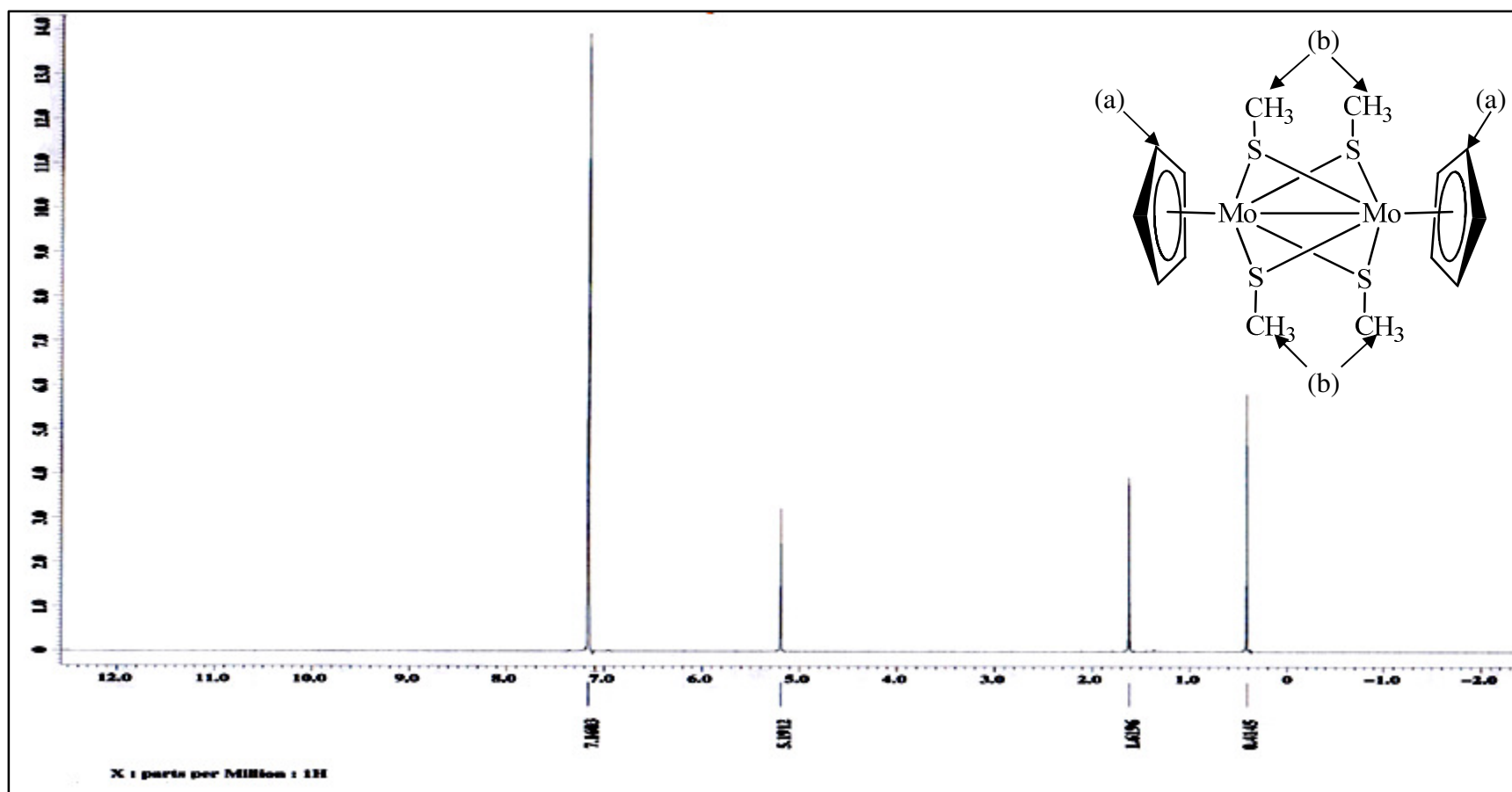
Figure 4.1: ^{1}H NMR spectrum for *bis*(η^5-cyclopentadienyl)dimolybdenumtetramethythiol, [(η^5-Cp)Mo(SMe)$_2$]$_2$ (**2**).

Figure 4.2: ^{13}C NMR spectrum for *bis*(η^5-cyclopentadienyl)dimolybdenumtetramethythiol, [(η^5-Cp)Mo(SMe)$_2$]$_2$ (**2**).

4.2.2   Fourier-transform Infrared (FT-IR) Analysis

Infrared spectroscopic analysis was carried out to analyze complex **2** using nujol mull with KBr cell. Figure 4.3 showed the FT-IR for complex **2** and the spectrum is identical to the literature (King, 1963). The IR spectrum showed the present of C=C-H (2924 cm^{-1}), C-H (2854 cm^{-1}), C=C (1456 and 1377 cm^{-1}) and C-S (1101, 997 and 783 cm^{-1}). The paraffin oil absorption peaks were overlapped with the complex **2** absorption peaks at 2854, 1456 and 1377 cm^{-1}. Nevertheless, the carbonyl groups are absence because there are no traces of molybdenum hexacarbonyl and complex **1** remained as shown in Figure 4.3. Thus, the conversion of complex **1** to complex **2** was successful.
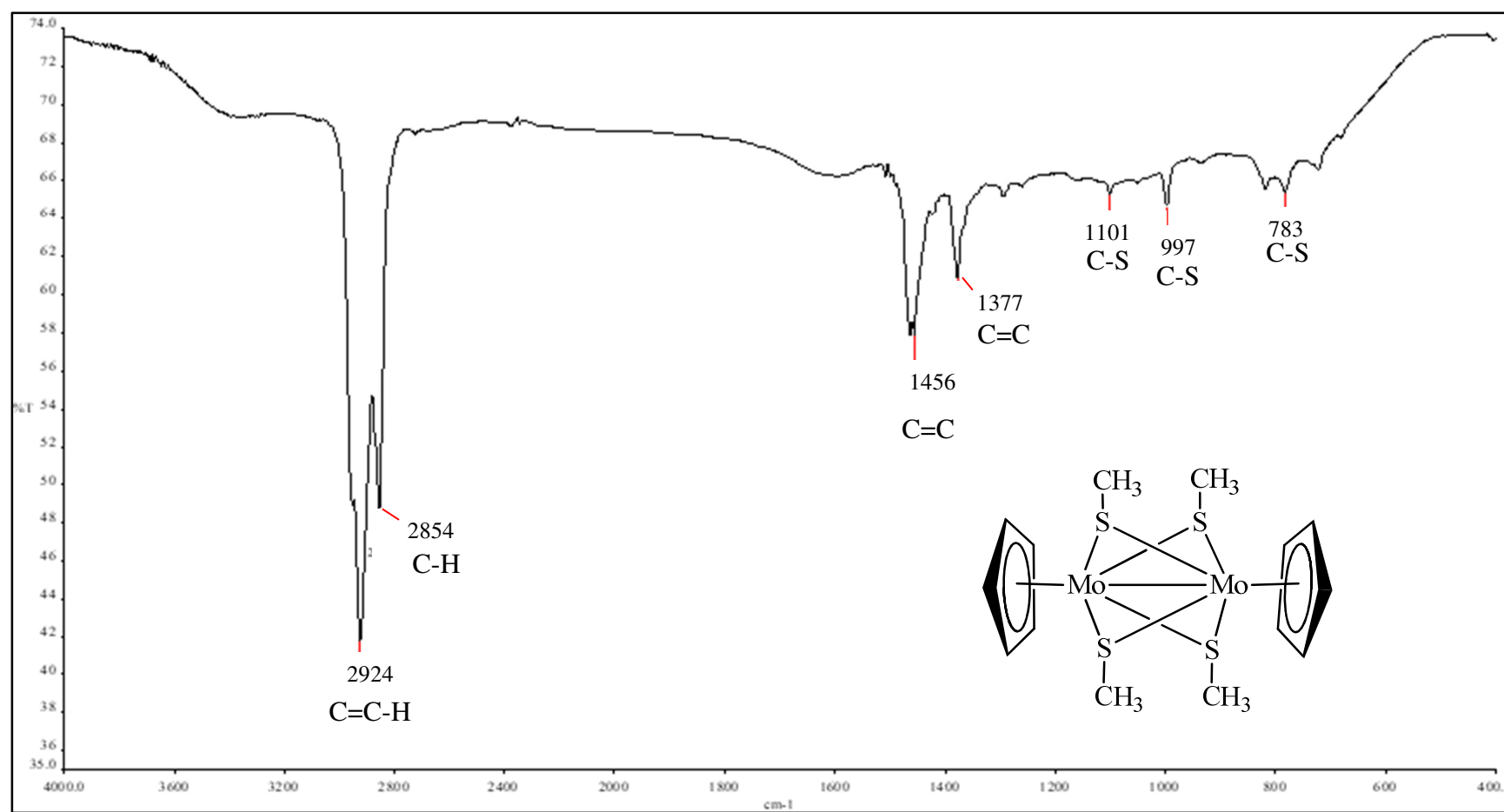
Figure 4.3: FT-IR spectrum for *bis*(η^5-cyclopentadienyl)dimolybdenumtetramethythiol, [(η^5-Cp)Mo(SMe)$_2$]$_2$ (**2**).

4.2.3 Thermogravimetric (TGA) Analysis

Complex **2** was analyzed using thermogravimetric analysis (TGA) in order to determine the thermal decomposition temperature as a precursor for AACVD. Complex **2** decomposed in one step, where the weight loss started at ~200 $^{\circ}$C and the final decomposition temperature was observed at 400 $^{\circ}$C. The TGA profile with derivative thermogravimetric (DTG) profile is shown in Figure 4.4. The weight percentage loss of 41.4% and the residue of 52.6% suggested that the formation of 1 mole of Mo_2S_3 (calc. 56.2%). The residue was lower than the expected formation of 1 mole of Mo_2S_3 could be due to reduction of Mo_2S_3 into MoS_2.

Both cobaltocene and nickelocene air sensitive, hence the decomposition temperature for both of these metallocenes were referred directly from the literature (Bhattacharjee et al., 2014; Vieyra-Eusebio and Rojas, 2011). According to the literature ferrocene, cobaltocene and nickelocene will have the final decomposition temperature of 175 $^{\circ}$C .
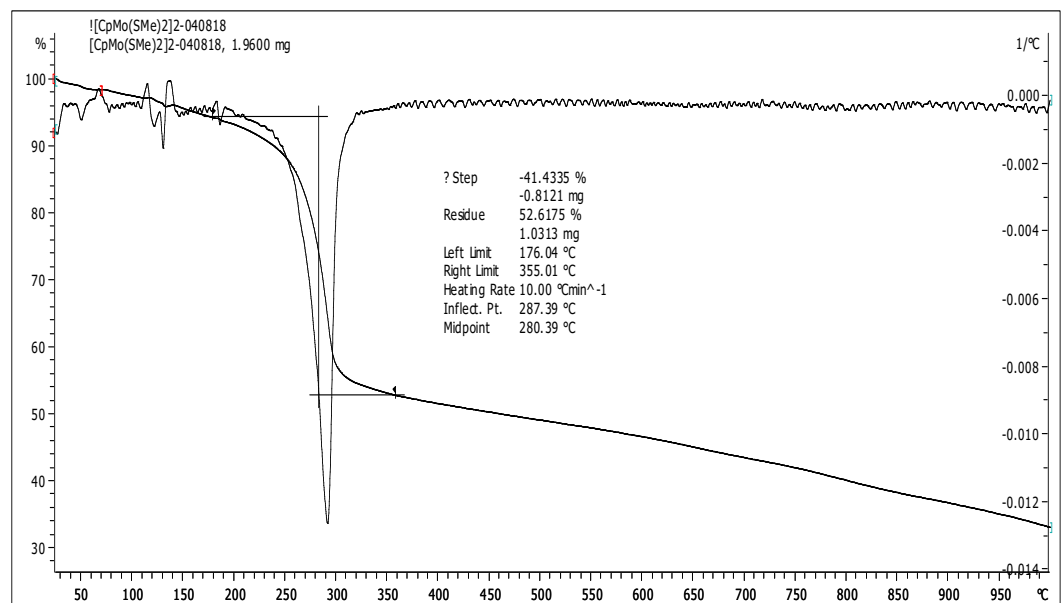
Figure 4.4: DTG profile overlap with TGA profile for complex **2**.

4.3 Characterization of Thin Films Prepared from [(η⁵-Cp)Mo(SMe)₂]₂ (2) With Different mol% of Ferrocene, Cp₂Fe (Cp = cyclopentadiene)

All films prepared from complex **2** in different mol % of Cp₂Fe at 550 °C *via* AACVD process in 20 minutes were characterized with XRD, Raman spectroscopy, XPS, EDX, AFM, SEM and UV-Vis spectroscopy. The photoelectrochemical studies were also performed by analyzing the J-V curve, Nyquist plot, Bode plot and Mott-Schottky plot.

4.3.1 X-ray Diffraction Analysis (XRD)

The XRD patterns of different mol% Fe-doped thin films are shown in Figure 4.5. The strong FTO background is due to the thickness of FTO layer is much thicker than the Fe-doped thin film. Nevertheless, the XRD patterns of each were found to be comprised of 3 types of crystal structures which were identified with International Centre for Diffraction Data (ICDD) database which are rhombohedral MoS_2 (ICDD 01-077-0341), monoclinic Mo_2S_3 (ICDD 01-078-1332) and monoclinic $Fe(MoS_2)_2$ (ICDD 01-070-8639). The peaks for MoS_2 were observed at 14.44°, 15.40°, 37.96° and 51.68° which correspond to (002), (012), (104) and (018) diffraction plane, respectively. The XRD pattern for Mo_2S_3 is shown at 17.13°, 34.17°, 51.68° and 65.55° which corresponded to (-101), (111), (-114) and (-221) respectively. Apart from that the thin films also matches with the XRD pattern of monoclinic $Fe(MoS_2)_2$ (ICDD 01-070-8639). Some of the peaks from MoS_2 are coincidentally matches with the $Fe(MoS_2)_2$ 15.40°, 34.17°, 37.96° and 51.68° correspond to (002), (221), (-115) and (331), respectively. There are also overlapping of $Fe(MoS_2)_2$ with Mo_2S_3 at the 17.13° and 34.17°, respectively. It was interesting to note that the peaks at 2θ (15.40°) only exist in the Fe-doped thin film. The Fe atom which was originated from the Cp_2Fe was believed located in the interstitial site of MoS_2 where was intercalated between two layers of sulfur atoms to form $Fe(MoS_2)_2$. Similar phenomena were reported by previous studies (Dai et al., 2015; Feng et al., 2015; Topsøe et al., 1981; Xiong et al., 2018).

The characteristic peaks are tabulated in Table 4.1. It is worth noting that the intensity of $Fe(MoS_2)_2$ at the peak of 17.18^o (-202) was the highest at 20 mol% Fe-doped thin films followed by 40 mol% and 80 mol% Fe-doped thin films while the 10 mol% and 100 mol% Fe-doped thin films showed small peak at that particular phase. This observations could be due to their small thin film thickness (refer to section 4.3.6 for thickness comparison).
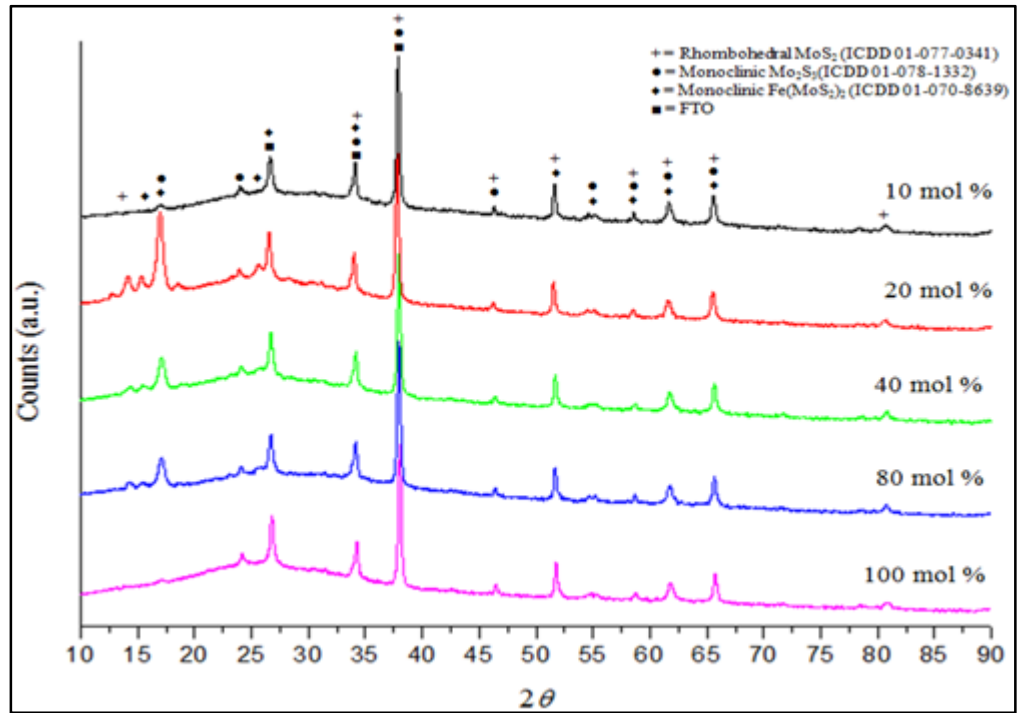
Figure 4.5: XRD diffraction patterns for 10 mol %, 20 mol %, 40 mol %, 80 mol % and 100 mol % of Fe-doped thin films.

Table 4.1: XRD characteristic peak list for Fe-doped thin film.

2θ	Assigned Peak
14.44	MoS_2
15.40	$Fe(MoS_2)_2$
17.13	Mo_2S_3/ $Fe(MoS_2)_2$
24.01	Mo_2S_3
26.70	$Fe(MoS_2)_2$/FTO
34.17	MoS_2 / Mo_2S_3 / $Fe(MoS_2)_2$/FTO
37.96	MoS_2 / Mo_2S_3/$Fe(MoS_2)_2$/FTO
46.40	Mo_2S_3/ $Fe(MoS_2)_2$
51.68	MoS_2/ Mo_2S_3/ $Fe(MoS_2)_2$
55.09	Mo_2S_3/ $Fe(MoS_2)_2$
58.66	MoS_2/ Mo_2S_3/ $Fe(MoS_2)_2$
61.74	MoS_2 / Mo_2S_3/ $Fe(MoS_2)_2$
65.55	MoS_2 / Mo_2S_3 / $Fe(MoS_2)_2$
80.87	MoS_2
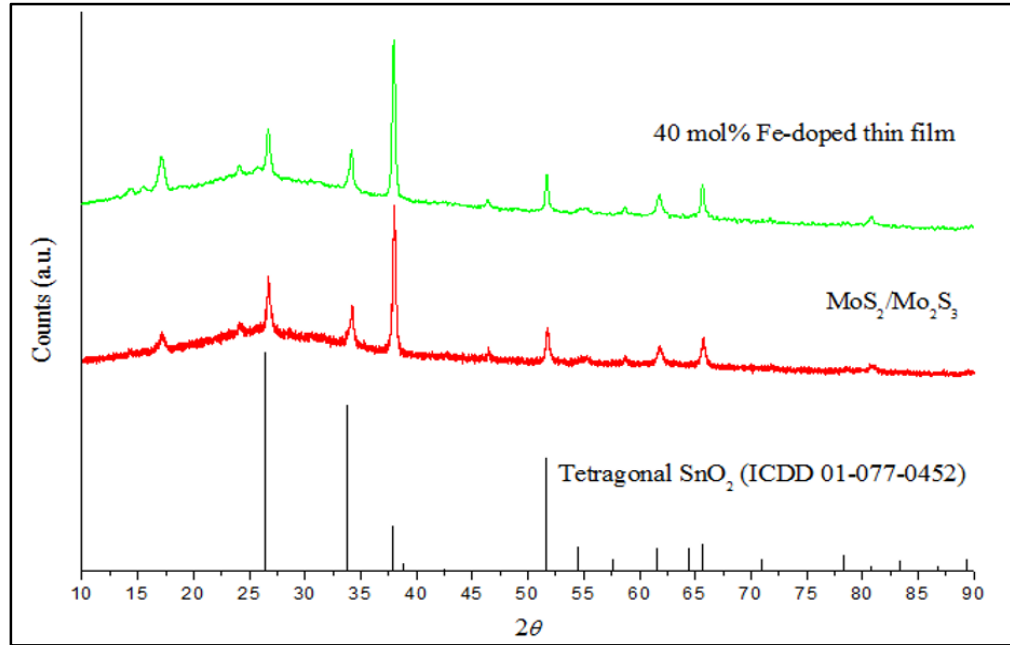
Figure 4.6: Comparison of XRD diffraction patterns for 40 mol% Fe-doped thin film, MoS_2/Mo_2S_3 and tetragonal SnO_2 (ICDD 01-077-052).

4.3.2   Raman Spectroscopy Analysis

Raman spectroscopy of 80 mol% Fe-doped thin film was carry out because it has homogenous morphology based on secondary electron microscopy (SEM) analysis as well as highest atomic percentage (at %) of iron (Fe) when compared to 10, 20, 40 and 100 mol% Fe-doped thin films. As shown in Figure 4.7, there are peaks at the values of 379.57 and 398.74 cm^{-1} which are corresponded to the typical E^1_{2g} and A_{1g} of MoS_2. The difference between these two peaks is 19.17 cm^{-1} which indicates that the MoS_2 is monolayer (Topsøe et al., 1981; Xiong et al., 2018; Lim et al., 2019). As shown in the spectrum, the existence of the broad peak is due to the overlapping between MoS_2 and Mo_2S_3 where it is in agreement with XRD analysis which shows the presence of MoS_2 and Mo_2S_3. The presence of amorphous molybdenum with sulfide bridging was indicated by the peaks at 336.28 and 452.81 cm^{-1} (Khaemba, Neville and Morina, 2016).
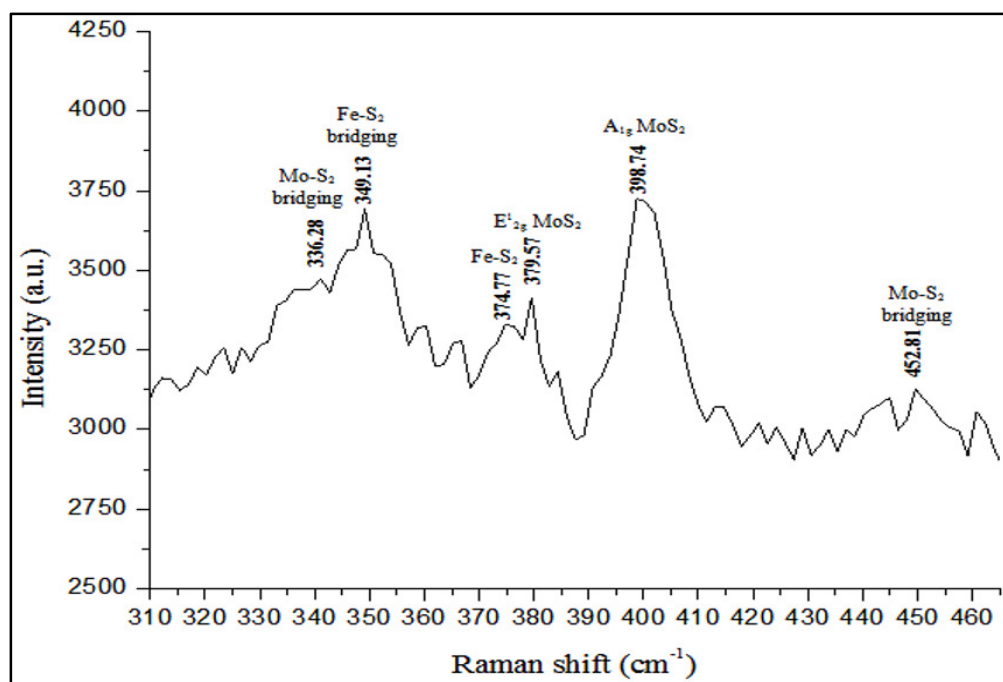
Figure 4.7: Raman spectroscopy of 80 mol % Fe-doped thin film.

4.3.3 X-ray Photoelectron Spectroscopy (XPS) Analysis

All Fe-doped thin films have been analyzed by XPS analysis. Figure 4.8, 4.9 and 4.10 had showed the XPS spectrum for Fe 2p, Mo 3d and S 2p of Fe-doped thin film. From the XPS spectrum for Fe 2p, Fe^{3+} was found in all thin films. The multiplet splitting occurs at ~711.30 and ~713.52 eV is due to the high spin Fe^{3+} based on the literature findings (Grosvenor et al., 2004; Matamoros-Veloza et al., 2018). While for the 10, 20 and 40 mol % Fe-doped thin film, both Fe^{2+} and Fe^{3+} were observed in the XPS spectrums. The Fe^{2+} binding energy at $2p_{3/2}$ and $2p_{1/2}$ was recorded at ~ 709 eV and ~ 723 eV, respectively. There are chemical shifts among different mol % doping due to different bondings between the elements. Smaller peaks that are present in the spectrums are due to Plasmon

loss peaks which are caused by interaction between photoelectrons and electrons. The presence of Fe^{2+}/Fe^{3+} is beneficial for the redox reaction as it functions as the redox mediator (Arai et al., 2007, Miseki and Sayama, 2012, Wang et al., 2017). The intensity of the Fe^{2+} and Fe^{3+} is proportional to the amount of Fe ions presence in the thin film and it may affect the photocatalytic activity performance. The 100 mol % Fe-doped thin film does not follow the trend where it showed less amount of Fe when compared to 20, 40 and 80 mol %. This observation could be due to spontaneous decomposition of ferrocene when in larger amount to form metallic iron and sublime at the glass tube during AACVD process (Bhattacharjee et al., 2014; Leonhardt et al., 2006). This disadvantage was also observed in the SEM, XRD and UV-Vis spectroscopy as well by PEC studies.
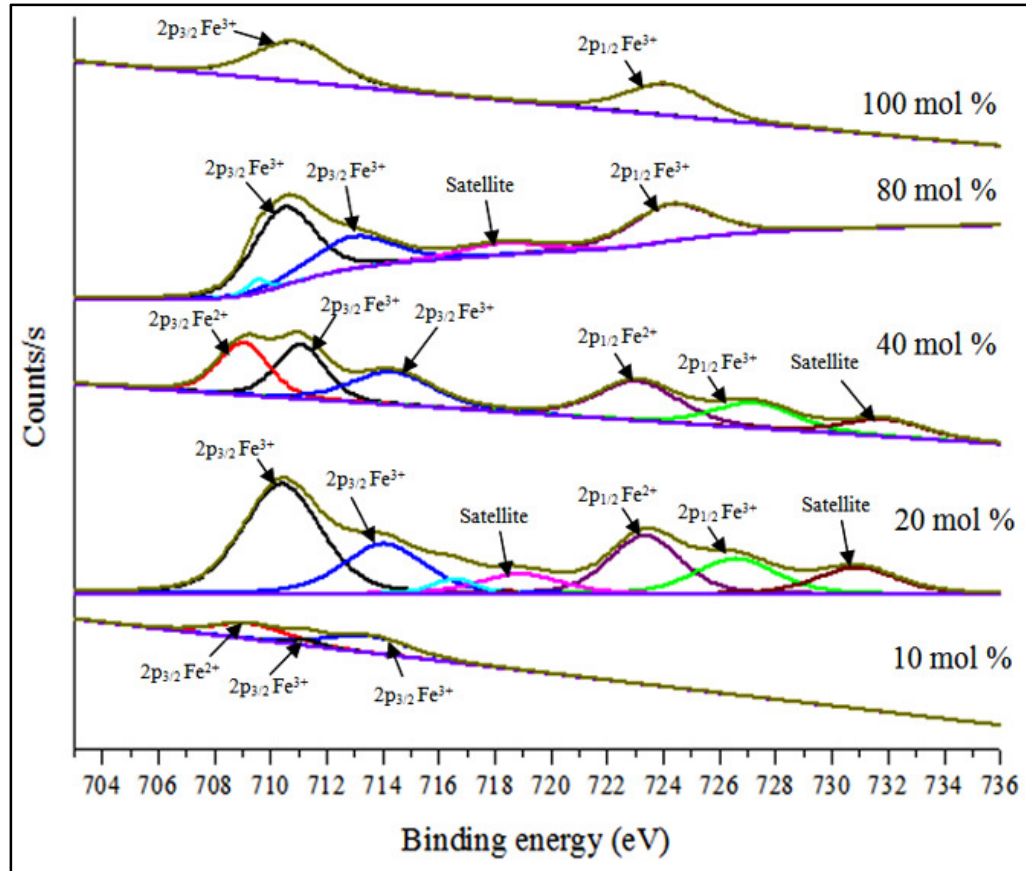
Figure 4.8: Fe 2p XPS spectrum for Fe-doped thin film.

As for Mo 3d, Figure 4.9 had showed the presence of Mo^{3+} and Mo^{4+} are presents in the thin film which was corresponded to the apical sulfur of Mo_2S_3 and MoS_2, respectively. The binding energy at 231.97 and 235.10 eV corresponded to the Mo^{3+} $3d_{5/2}$ and Mo^{3+} $3d_{3/2}$ whereas at 228.75 and 231.97 eV is referred to the Mo^{4+} $3d_{5/2}$ and Mo^{4+} $3d_{3/2}$ and that there is an overlapping between two different peaks for Mo^{3+} and Mo^{4+} at binding energy of 231.97 eV (Lim et al., 2019; Zhang et al., 2016). Furthermore, the intensity of Mo^{4+} diminishes as the mol% of Fe dopants increases while the Mo^{3+} increases. It can be observed that the Mo^{3+} becomes dominant for the 80 mol% Fe-doped thin films.
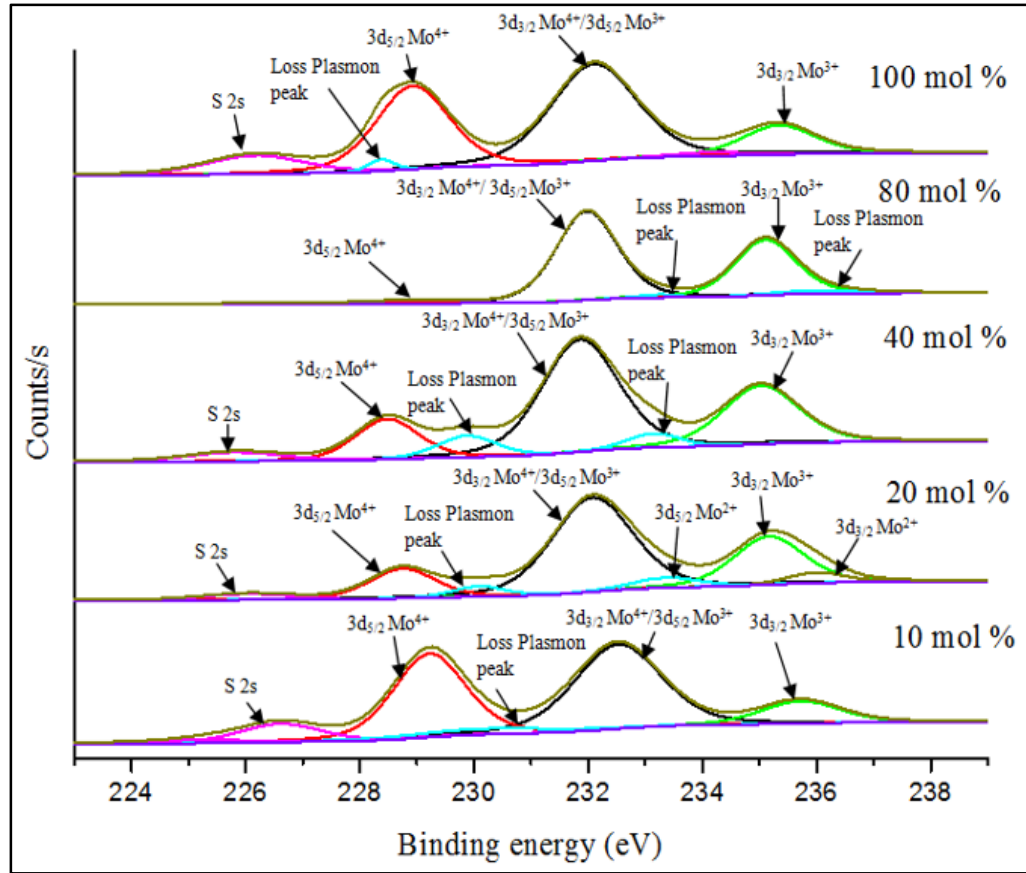
Figure 4.9: Mo 3d XPS spectrum for Fe-doped thin films.

The S 2p spectrum was shown in Figure 4.10. The binding energy of 162.4 and 163.7 eV which correspond to the S^{2-} $2p_{3/2}$ and S^{2-} $2p_{1/2}$ were in agreement with the reported literature (Lim et al., 2019). Peak with binding energy of 164.4 eV corresponds to apical S^{2-} $2p_{1/2}$ of Mo_2S_3 where there was a gradual rise upon increasing of Fe dopant in the thin film. Moreover, the Fe-S was overlapped with the peak at binding energy of 163.7 and 164.4 eV for S^{2-} $2p_{1/2}$ and S^{2-} $2p_{3/2}$, respectively (Tang et al., 2018). Smaller peaks that were present in the spectrums are due to Plasmon loss peaks which were caused by interaction between photoelectrons and electrons. The satellite peaks exist because of sudden change

in Coulombic potential as the photoejected electron passes through the valence band.

   The XPS analysis findings concluded that the thin films are made of composites materials which are in agreement with the XRD findings. This could be due to the machine limitation as the analysis is based on the surface. The sampling depth is usually 3-10 nm. Moreover, the roughness and surface morphology could also affect the XPS analysis.
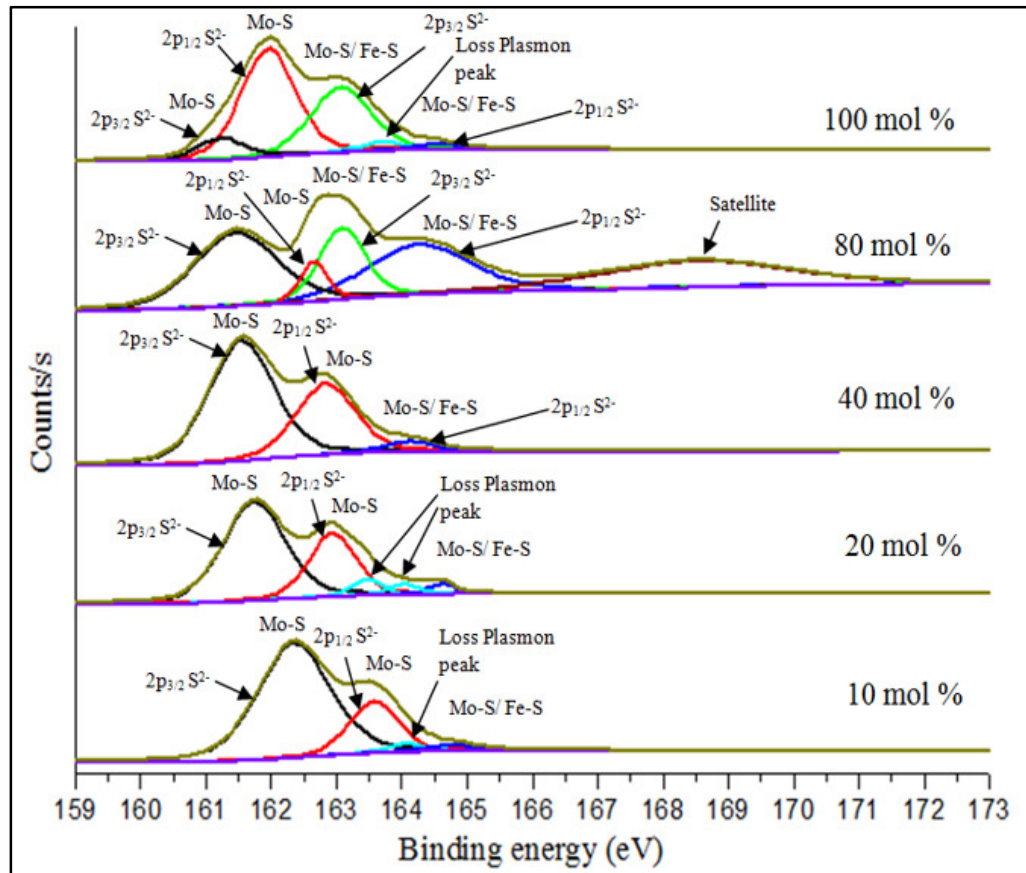
Figure 4.10: S 2p XPS spectrum for Fe-doped thin films.

4.3.4 Energy Dispersive X-ray (EDX) Spectroscopy and Elemental Mapping Analysis

Elemental analysis was carried out to determine the composition of the thin films with electron acceleration voltage of 20 kV. Elemental mapping analyses were used to investigate the homogeneity of the thin films. Five points on the thin films were randomly selected during the EDX analyses and average value of atomic percent (at %) were calculated. The EDX graphs were illustrated in Figure 4.11 while the results were tabulated in Table 4.2. It was found out that the elemental composition (at %) of molybdenum and sulfur ratio are in the range of 1:1.53 whereas the Fe dopant that was present in the thin film was lesser than the expected theoretical value. This could be due to the low sublimation point of Fe at 55 $^{\circ}$C (Lousade et al., 2008) resulting in a considerable amount of Fe that was deposited on the inner wall of the glass tube during thin film fabrication process. It was also observed that when the mol percentage of ferrocene increased in the feed, the amount of iron deposited on the thin films was also increased. However, this trend was stopped at 80 mol% Fe-doped thin film where the 100 mol% Fe-doped thin film has lower Fe atomic % than the 80 mol% Fe-doped thin film. The actual reason for this observation is still unclear. According to a literature source, there was a possibility that the ferrocene decompose spontaneously at 550 $^{\circ}$C to form metallic iron and sublimed onto the inner wall of glass tube during the AACVD process (Sarkar et al., 2014; Bhattacharjee et al., 2014) and higher amount may cause the sublimation on the wall to be possible. The elemental mapping analyses for the Fe-doped thin films were showed in

Figure 4.12 where Mo, S and Fe were seen distributed homogenously on the thin films despite of having different atomic% of Fe dopant that was present in the thin films.

Table 4.2: EDX results for various mol% of Fe-doped thin films.

Mol% of Fe-doped thin film	Elements	Atomic % (at %)
10	Mo	40.44
	Fe	0.94
	S	58.62
20	Mo	41.30
	Fe	1.67
	S	57.03
40	Mo	38.61
	Fe	2.33
	S	59.06
80	Mo	45.41
	Fe	2.73
	S	51.86
100	Mo	44.40
	Fe	0.82
	S	54.77
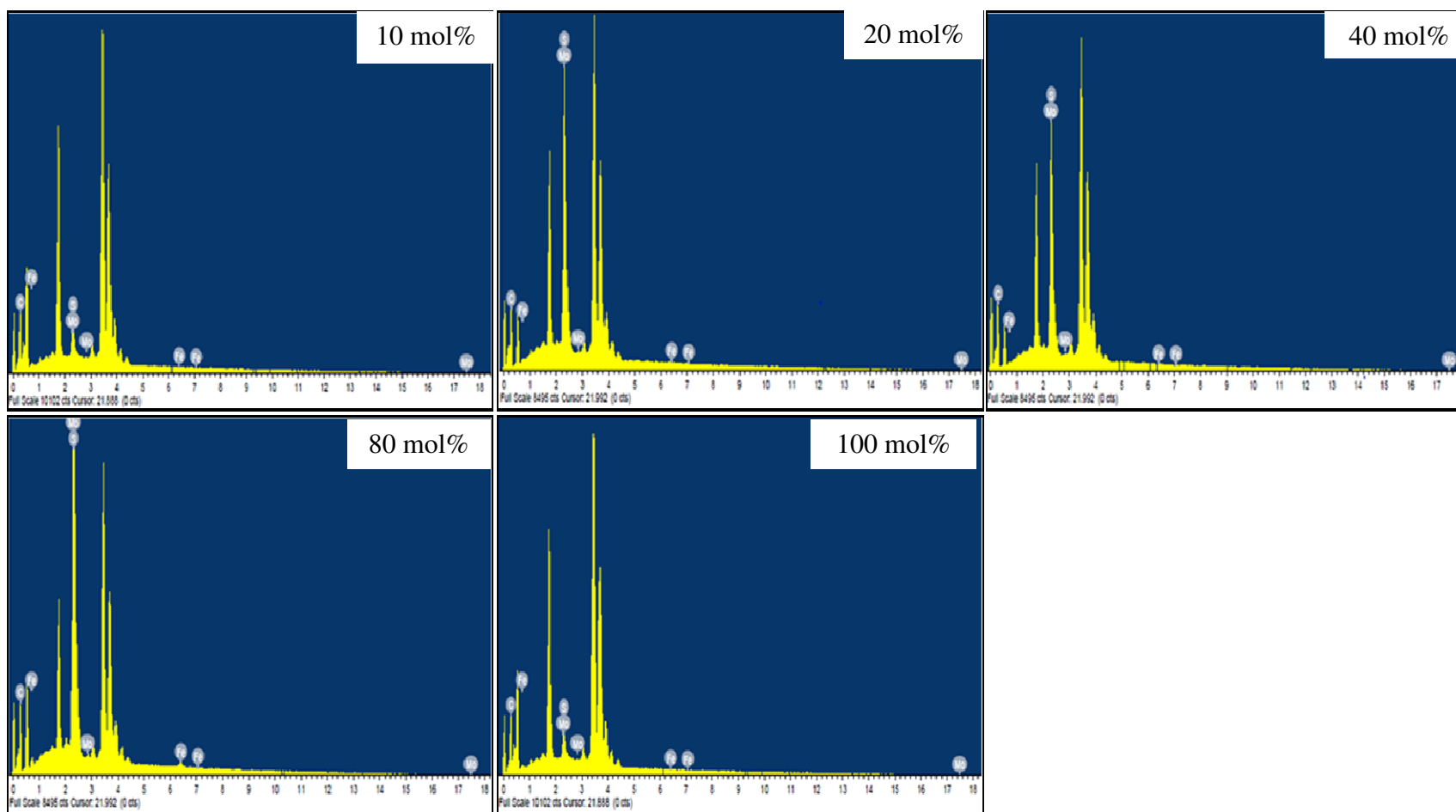
Figure 4.11: EDX graph for various mol% Fe-doped thin films.

10 mol% Fe-doped thin film
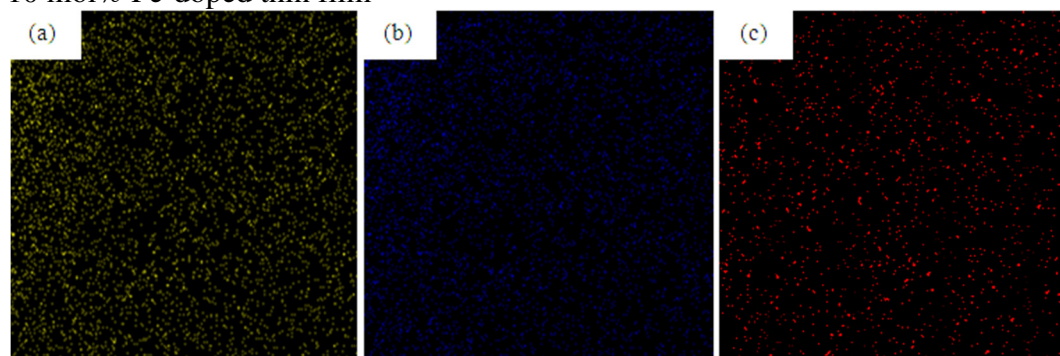
20 mol% Fe-doped thin film
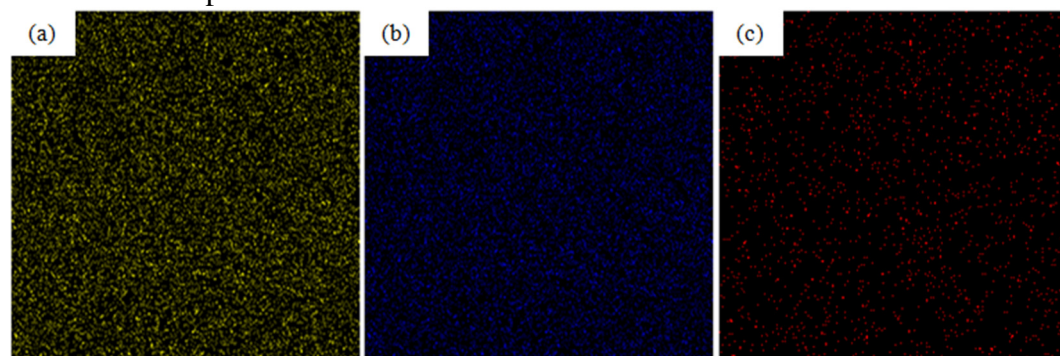
40 mol% Fe-doped thin film
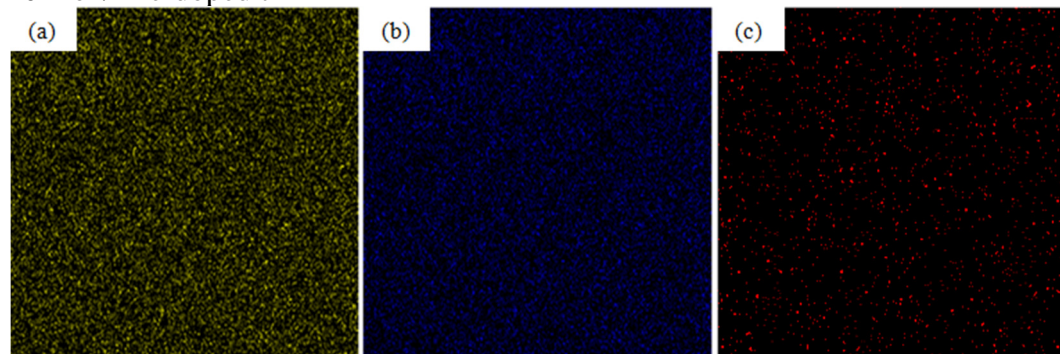
80 mol% Fe-doped thin film
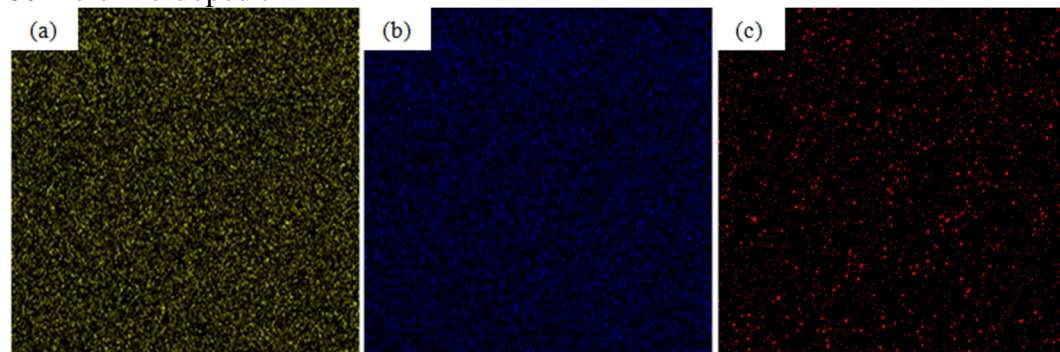
100 mol% Fe-doped thin film
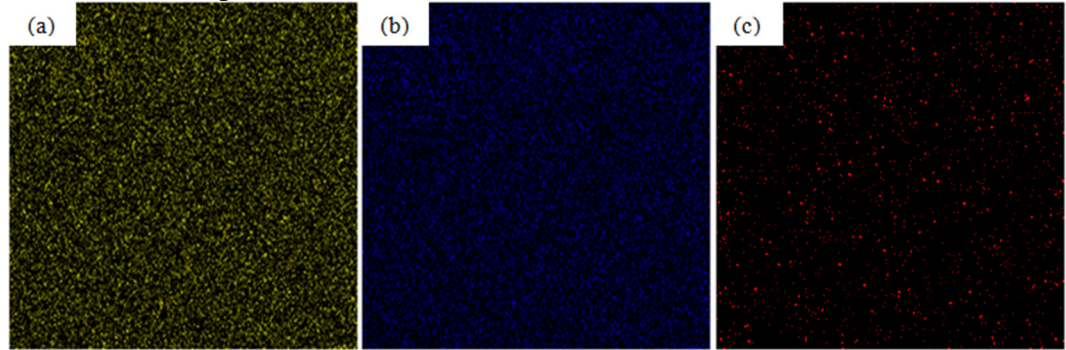
Figure 4.12: EDX elemental mapping Fe doped thin film (a) sulfur, (b) molybdenum and (c) iron.

4.3.5 Atomic Force Microscopy (AFM) Analysis

The surface morphology of the thin films was also investigated by using AFM analysis and similar observation as the SEM analyses was obtained where all thin film had granular morphology. Figure 4.13 shows the two dimensional (2D) images for Fe-doped thin films with area 10×10 while the line profiles for five different mol% of thin films were shown in Figure 4.14. The 2D images showed the presence of granular shape having void and coalescences between them while 3D images as shown in Figure 4.15 had showed the topology to be a standing rod having valleys between them. This indicates that the Fe-doped thin films were grown vertically layer-by-layer along the basal plane with strong covalent bonding (Ho et al., 2017). From the 2D and 3D AFM images, we noticed the 20 mol% Fe-doped thin film has the smallest intra-space between the nanorod followed by 100, 10 and 40 mol% Fe-doped thin films. As for the 80 mol% Fe-doped thin film, the largest intra-space between the nanorod arrays had been observed. The intra-space between the nanorods could be one of the factors that

affect the photoelectrochemical activity of the thin film because the wider intra-space could facilitate the electron flows. The thin films line profile parameters, roughness average (Ra), root mean square (Rq), maximum profile height (Rpv), maximum valley depth (Rv) and maximum peak height (Rp) were also analyzed and were tabulated in Table 4.3. The thin film roughness also shows the homogeneity of the thin film where small roughness is desirable because it would have better stability. From this analysis, 80 mol% of Fe-doped thin film has the highest roughness average, Ra, of 15.766 nm while 40 mol% of Fe-doped thin film has the lowest roughness average of 4.991 nm.
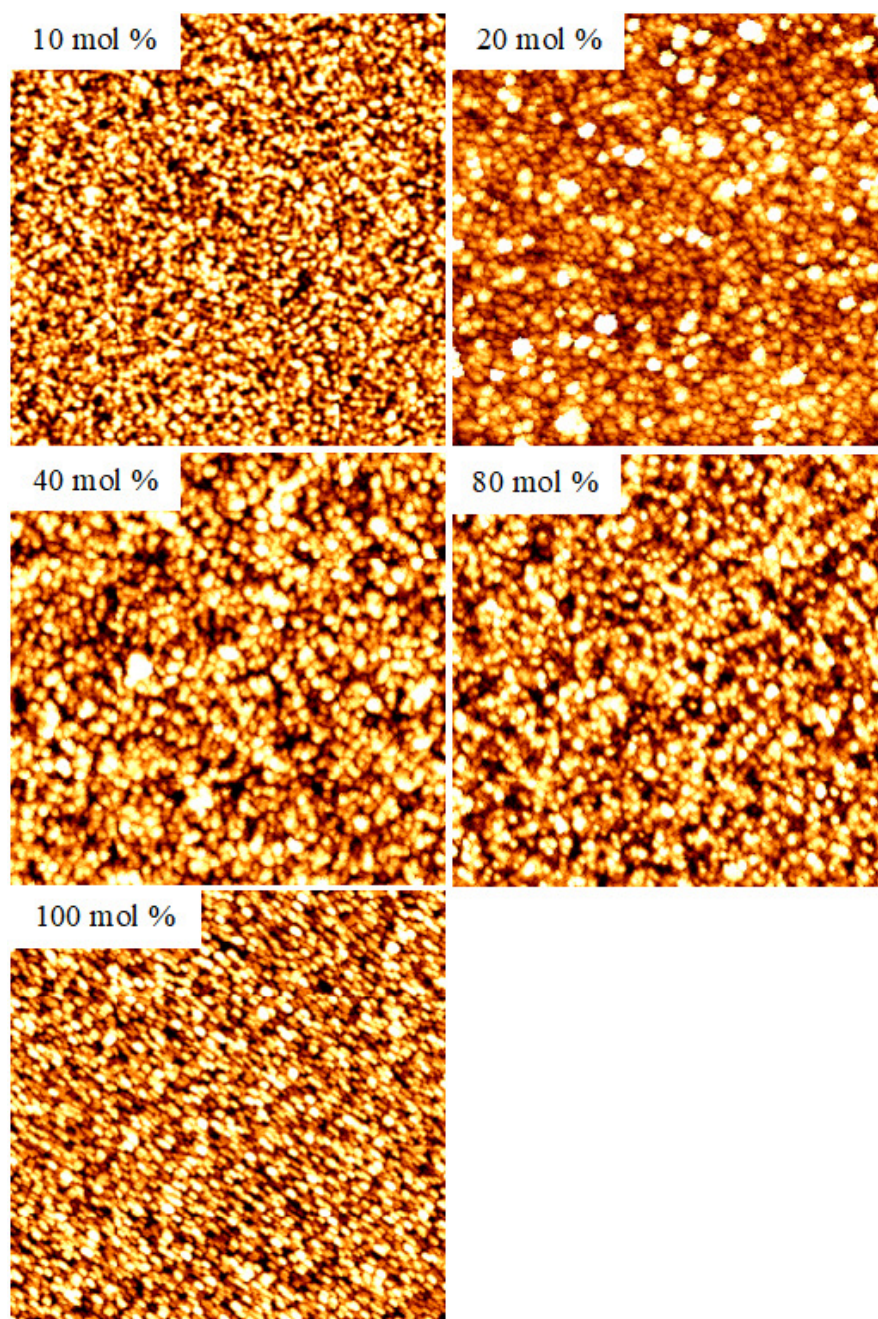
Figure 4.13: AFM 2D images for 10, 20, 40, 80 and 100 mol% of Fe-doped thin films.
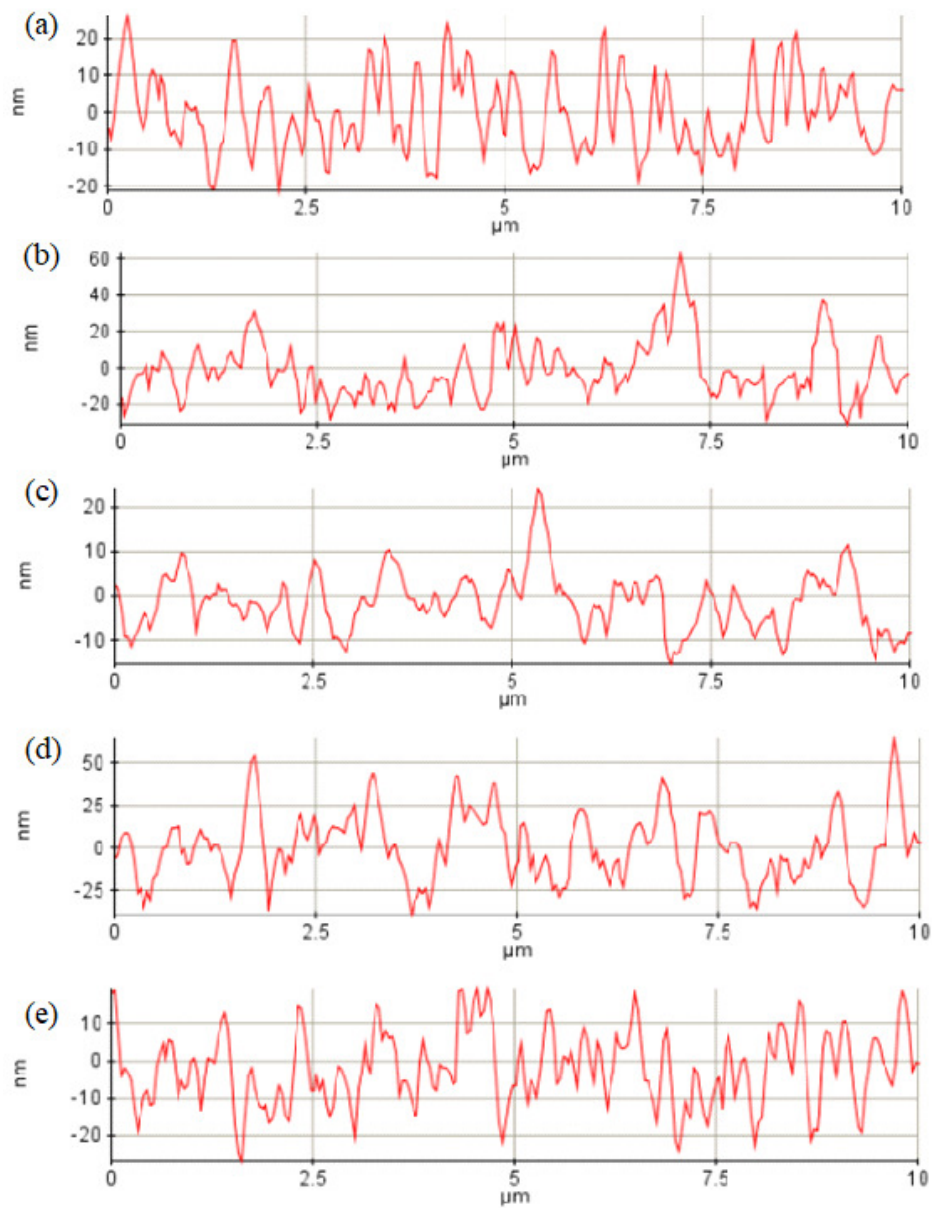
Figure 4.14: Line profile for (a) 10, (b) 20, (c) 40, (d) 80 and (e) 100 mol% of Fe-doping.
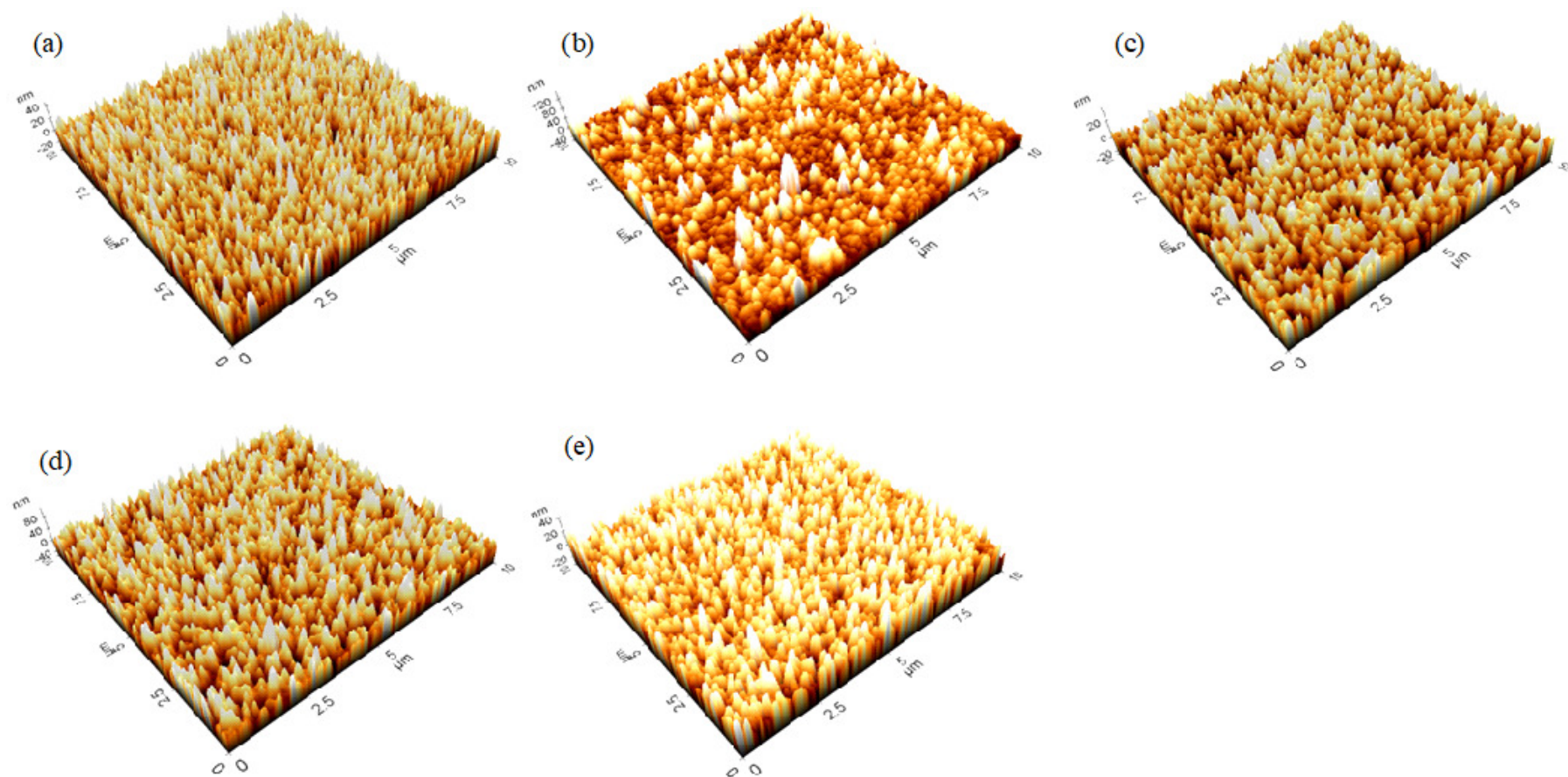
Figure 4.15: AFM 3D view for (a) 10, (b) 20, (c) 40, (d) 80 and (e) 100 mol% of Fe-doped thin films.

Table 4.3: Ra, Rq, Rpv, Rv and Rp for various mol% of Fe-doped thin films.

Mol %	Statistics	Value (nm)
10	Roughness average, Ra, (nm)	8.478
	Root mean square, Rq, (nm)	10.281
	Maximum profile height, Rpv, (nm)	47.284
	Maximum valley depth, Rv, (nm)	21.177
	Maximum peak height, Rp, (nm)	26.107
20	Roughness average, Ra, (nm)	11.813
	Root mean square, Rq, (nm)	15.734
	Maximum profile height, Rpv, (nm)	94.134
	Maximum valley depth, Rv, (nm)	31.488
	Maximum peak height, Rp, (nm)	62.645
40	Roughness average, Ra, (nm)	4.991
	Root mean square, Rq, (nm)	6.441
	Maximum profile height, Rpv, (nm)	39.360
	Maximum valley depth, Rv, (nm)	15.473
	Maximum peak height, Rp, (nm)	23.887
80	Roughness average, Ra, (nm)	15.766
	Root mean square, Rq, (nm)	19.832
	Maximum profile height, Rpv, (nm)	102.943
	Maximum valley depth, Rv, (nm)	38.057
	Maximum peak heaigh, Rp, (nm)	63.886
100	Roughness average, Ra, (nm)	7.999
	Root mean square, Rq, (nm)	9.871
	Maximum profile height, Rpv, (nm)	46.332
	Maximum valley depth, Rv, (nm)	27.039
	Maximum peak height, Rp, (nm)	19.293

4.3.6   Scanning Electron Microscopy (SEM) Analysis

The films that have been produced were analyzed using SEM to investigate the morphology and homogeneity of the thin films. The SEM images of various mol% Fe-doped thin films were taken at 40 000 magnification and 2.0 kV. Their respective cross-section images were taken at 10 000 magnification and are illustrated in Figure 4.16 to Figure 4.20. It was observed in the histogram as shown in Figure 4.19, the 80 mol% Fe-doped thin film has the smallest particle

size of 100 nm as compared to other thin films such as 120 nm for 100 mol%, 140 nm for 20 mol% and 160 nm for both 10 and 40 mol% Fe-doped thin films. Previously, our group had fabricated MoS_2/Mo_2S_3 thin films from complex **2** where the particle size was around 298 nm (Lim et al., 2019). This observation indicates that the incorporation of Fe dopant into the thin films allowed the Fe atom to intercalate between the interstitial sites of two S atoms. This shortening of the Fe-S bond eventually diminished the particle size. The small particle size may give an advantage in enhancing the photocatalytic activity as it had a large surface area which is at the interface of the thin films and the surrounding of the electrolytes. It was also observed that the amount of Fe dopant that was present in the thin films were proportional to the thin films thickness.

Due to its low surface roughness based on AFM analyses (refer to section 4.3.5), the images from SEM analysis appeared to be smooth and absence of distinguishable morphologies. As the 80 mol% Fe-doped has the highest roughness average of 15.766 nm, the morphology is distinguishable. Different mol% of Fe dopant gave different cross section thickness of the thin films because addition of different amount of dopant gave rise to different equilibrium film thickness. According to Clarke and Tanaka et al., the equilibrium film thickness is determined by the competition between the attractive Van der Waals forces, repulsive steric force and electric-double-layer force (Clarke, 1989; Tanaka et al., 1994). However, it was noting that the theory was qualitative understood and influence of amount of dopant on the film thickness should be further investigated. The thickness for 10, 20, 40, 80 and 100 mol% Fe-doped thin film is 155, 182,

204, 480 and 122 nm, respectively. The thickness value is reciprocal to the absorbance value which is in accordance to the Beer-Lambert's law (Aly and Akl, 2015). Therefore, 80 mol% of Fe-doped thin film has the highest absorbance value while 100 mol% of Fe-doped thin film has the lowest absorbance value. The SEM images were found to be in agreement with the AFM images for Fe-doped thin films.
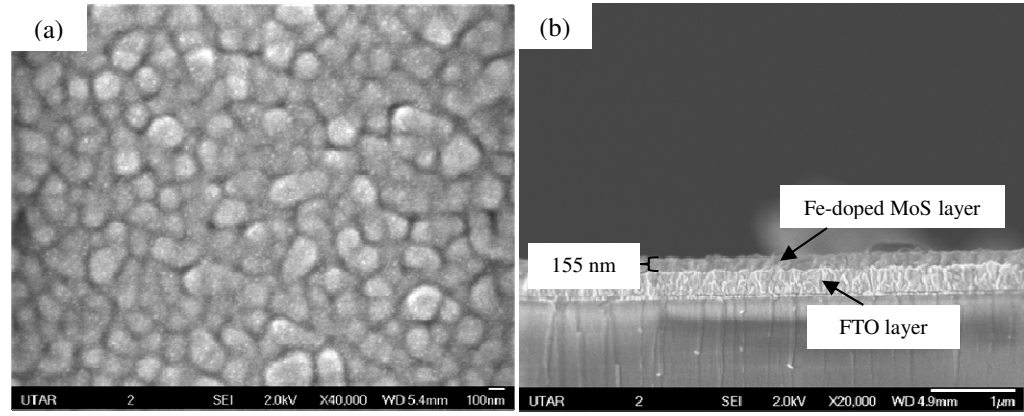
Figure 4.16: SEM images for 10 mol% Fe-doped thin film for (a) surface morphology and (b) cross section thickness.
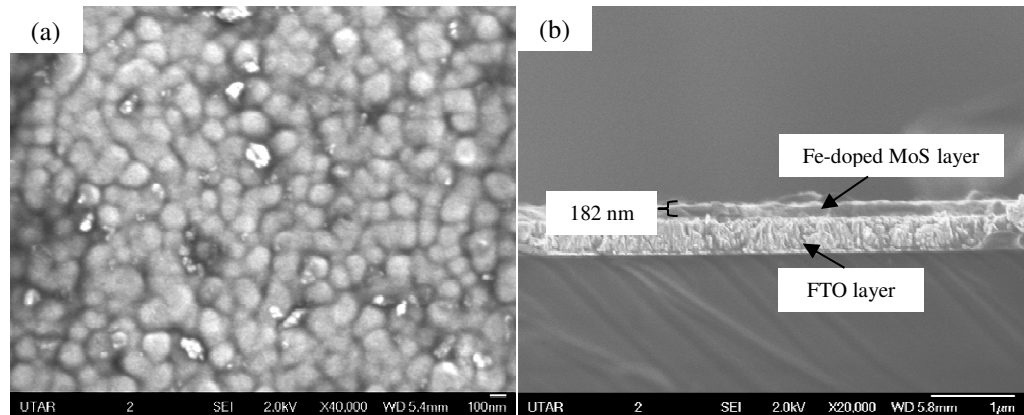
Figure 4.17: SEM images for 20 mol% Fe-doped thin film for (a) surface morphology and (b) cross section thickness.
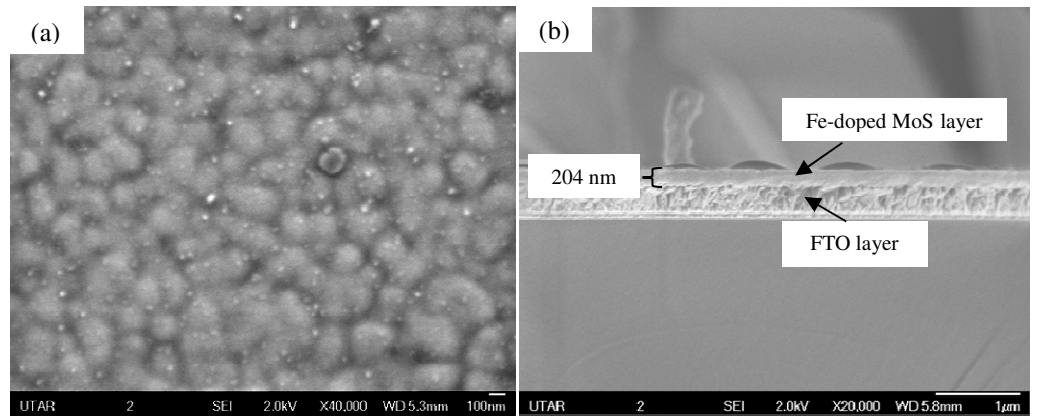
Figure 4.18: SEM images for 40 mol% Fe-doped thin film for (a) surface morphology and (b) cross section thickness.
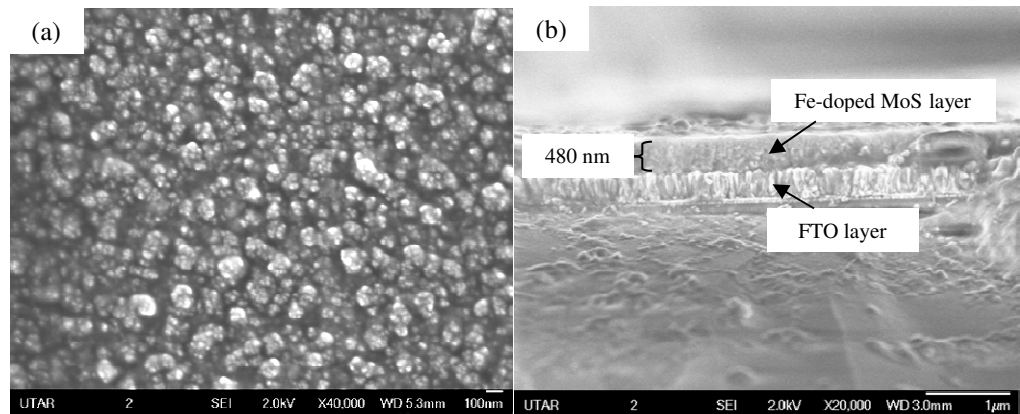
Figure 4.19: SEM images for 80 mol% Fe-doped thin film for (a) surface morphology and (b) cross section thickness.
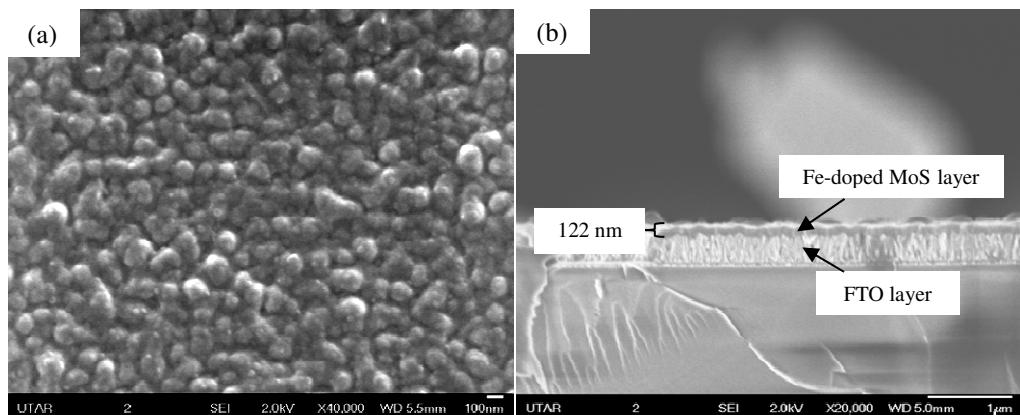
Figure 4.20: SEM images for 100 mol% Fe-doped thin film for (a) surface morphology and (b) cross section thickness.

The distributions of the particle size found from each film through the SEM analyses were plotted in the histogram as shown in Figure 4.21. From the histograms, 10, 20, 40, 80 and 100 mol% Fe-doped thin films showed the highest number of particle size at 160, 140, 160, 100 and 120 nm, respectively. It was concluded that the 80 mol% Fe-doped thin film gives the smallest particle size as compared to other mol% Fe-doped thin film. Particle size affects the number of active sites that is correlated to the photoelectrochemical activity. This is because small particle size gives a larger surface area at the interface of the thin film and the surrounding electrolytes and therefore larger number of active site are available for the photoelectrochemical activity.
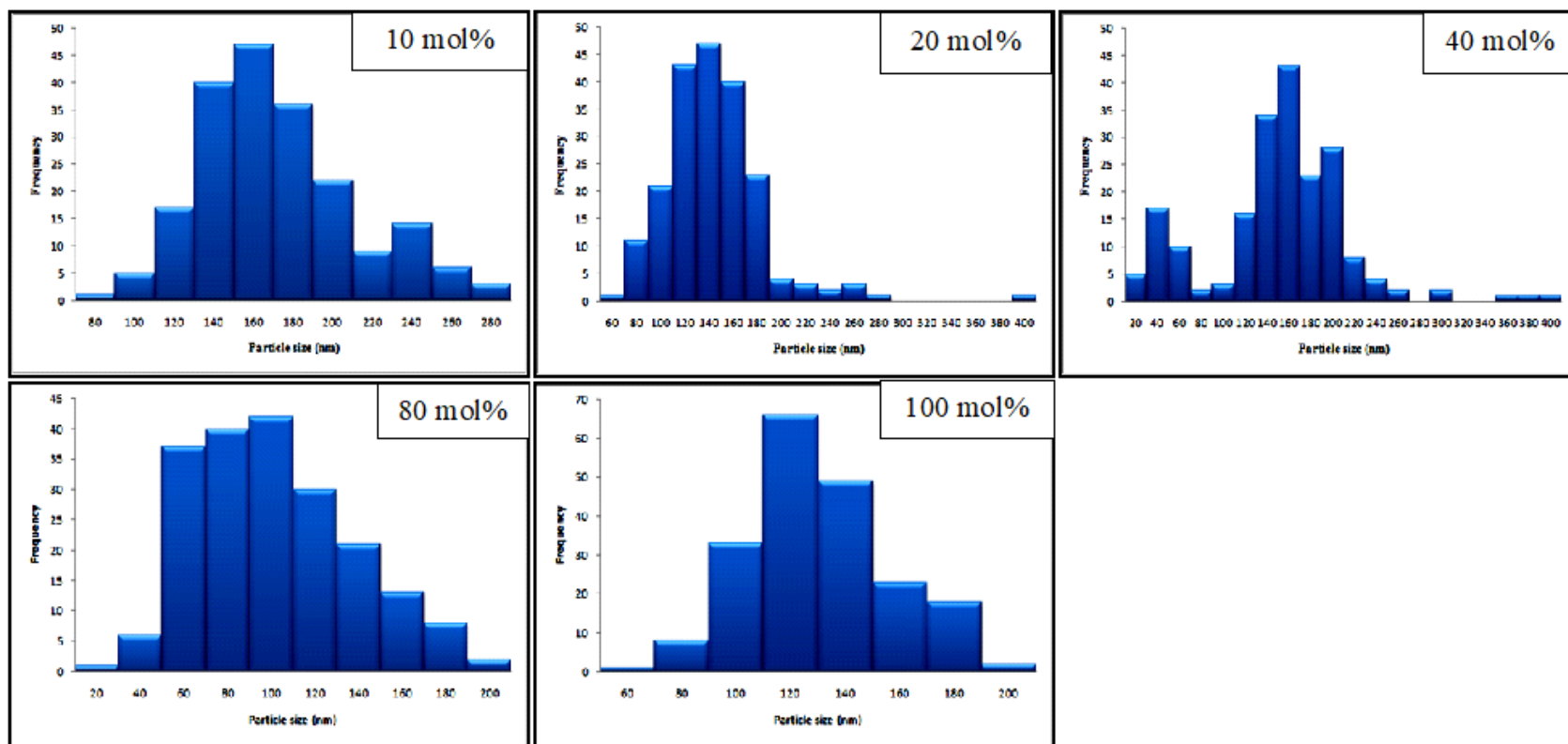
Figure 4.21: Histogram for various mol% Fe-doped thin films.

4.3.7   UV-Vis Spectroscopy Analysis

The UV-Vis spectroscopy analysis was conducted to determine the optical properties for all the thin films. Figure 4.22 shows the UV-Vis spectrum for 10, 20, 40, 80 and 100 mol% of Fe-doped thin films. It was observed that the thickness is proportional to the absorbance value where thicker film will have higher absorbance. The 80 mol% Fe-doped thin film shows the highest absorbance value followed by 40, 20, 10 and 100 mol% Fe-doped thin films, respectively. The obtained results were obeying with the Beer-Lambert's law (Luo et al., 2016). For the band gap value, it can be determined by two methods. The first method is by extrapolating a tangent to the x-axis of the UV-Vis spectrum to determine the cutoff wavelength (λ). Next, the determined cut off wavelength value was substituted into the Eq. (4.1) to obtain the band gap energy (Dharma, Pisal and Shelton, 2009). The second method is substituted the thin film's thickness into Eq. (4.2) to obtain the $\alpha h v^{1/n}$ value and make a Tauc plot (Murugadoss et al., 2016; Naeem, 2017). The band gap was determined from the Tauc plot by extrapolating a straight line to the energy axis at $\alpha h v = 0$. The Tauc plots of various mol% Fe-doped thin films were shown in Figure 4.23 while the respective UV-Vis spectrums with showing the cut off wavelength were also shown in the inset of the figure.

$$E_g = \frac{hc}{\lambda} \qquad \text{Eq. (4.1)}$$

$$\alpha h v^{1/n} = A(h v - E_g) \qquad \text{Eq. (4.2)}$$

For both of the equations, E_g represents the direct band gap. In Eq. (4.1), h, c and λ represent the Planck's constant (6.626 × 10³⁴ m²kg/s), speed of light (3.0 × 10⁸ m/s) and the cut off wavelength. From the Eq. 4.2, $n = \frac{1}{2}$ for determining the direct band gap of the thin film. The hv and A is the photon energy and proportionality constant respectively. Three different band gap values were obtained due to the present of three composite materials in the thin films (Lim et al., 2019). The $Fe(MoS_2)_2$ showed the value ~1.60 eV whereas MoS_2 and Mo_2S_3 had shown the value at ~1.95 eV and ~2.30 eV which are similar to the previous report from Lim et al. (2019). The band gaps for the Fe-doped thin films were summarized as shown in Table 4.4. It is noteworthy that regardless of the percentage amount of Fe dopant, the band gap does not shows significant changes. This observation is similar to Ratova's work on doping of molybdenum and nitrogen onto titania thin film (Ratova et al., 2015).
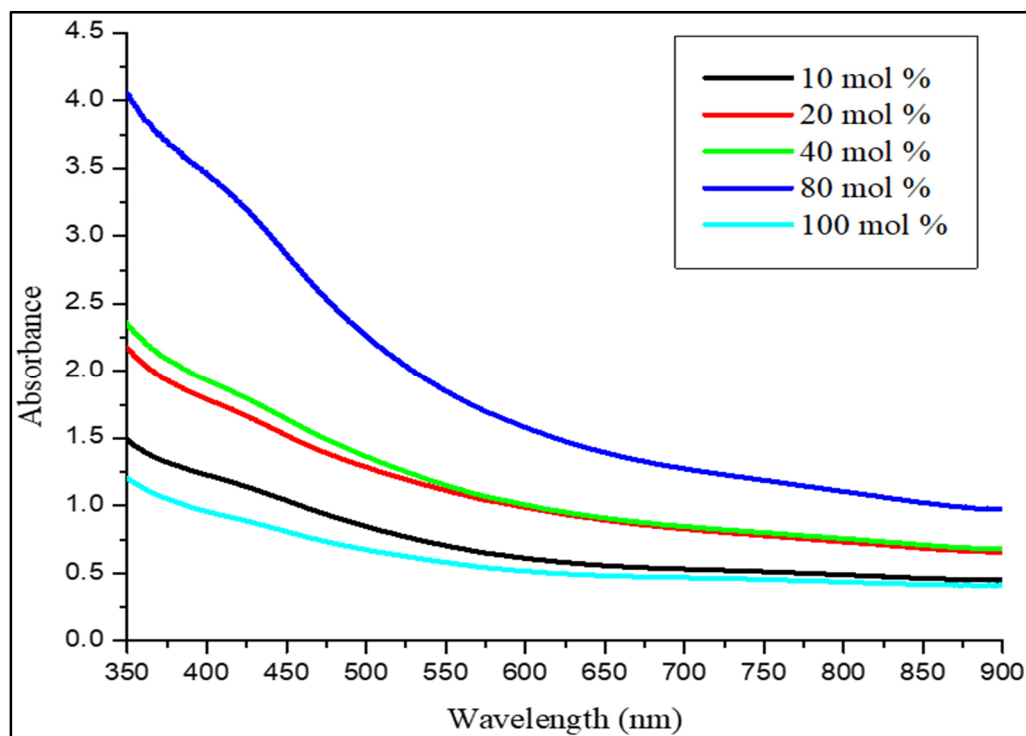
Figure 4.22: UV-Vis for 10, 20, 40, 80 and 100 mol% of Fe-doped thin films.

Table 4.4: Band gaps corresponding to the mol% of Fe-doped thin films.

Mol% of Fe doping	Cross section thickness (nm)	Band gap (eV)		
10	155	1.62	1.97	2.25
20	182	1.61	1.90	2.29
40	204	1.58	1.96	2.23
80	480	1.62	2.00	2.30
100	122	1.63	1.98	2.24
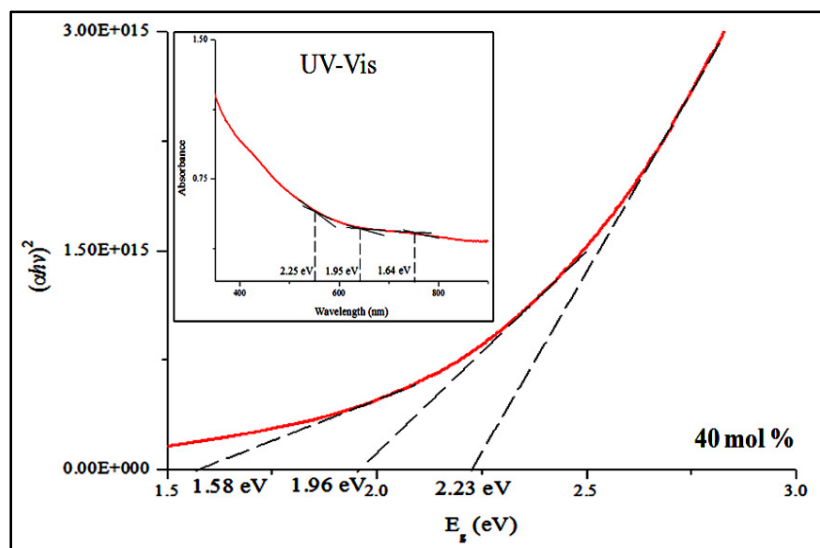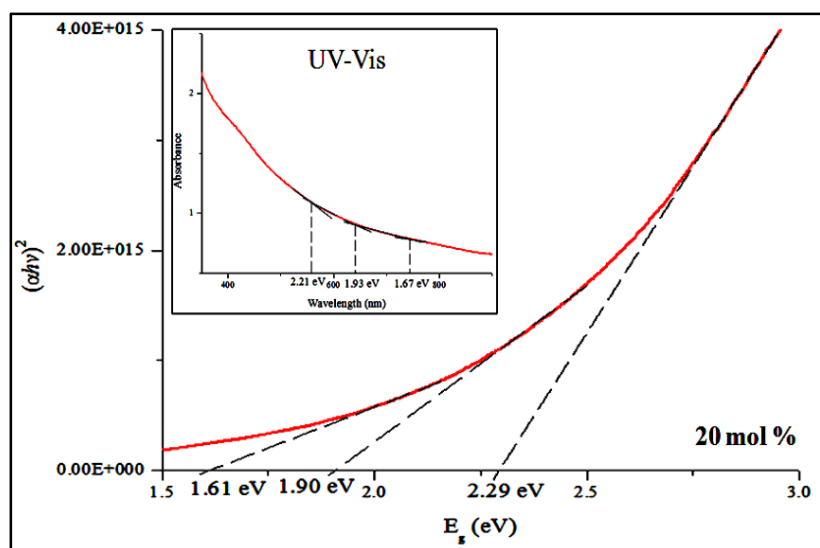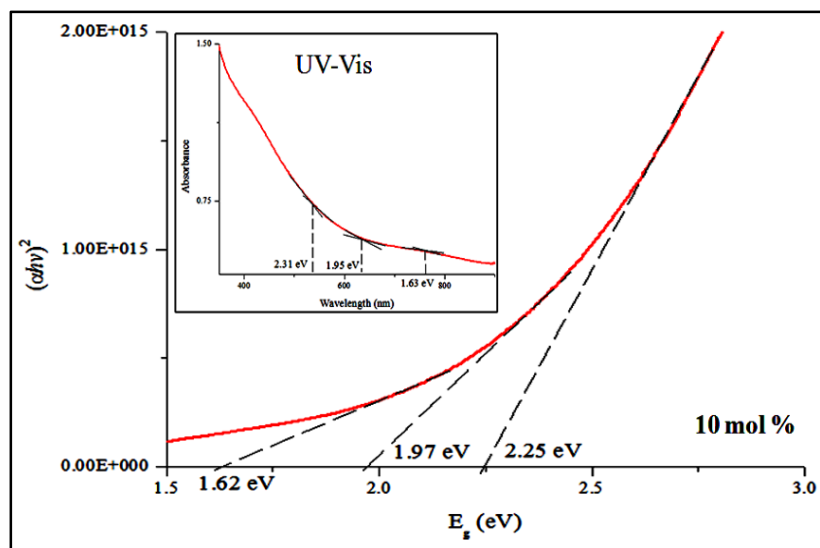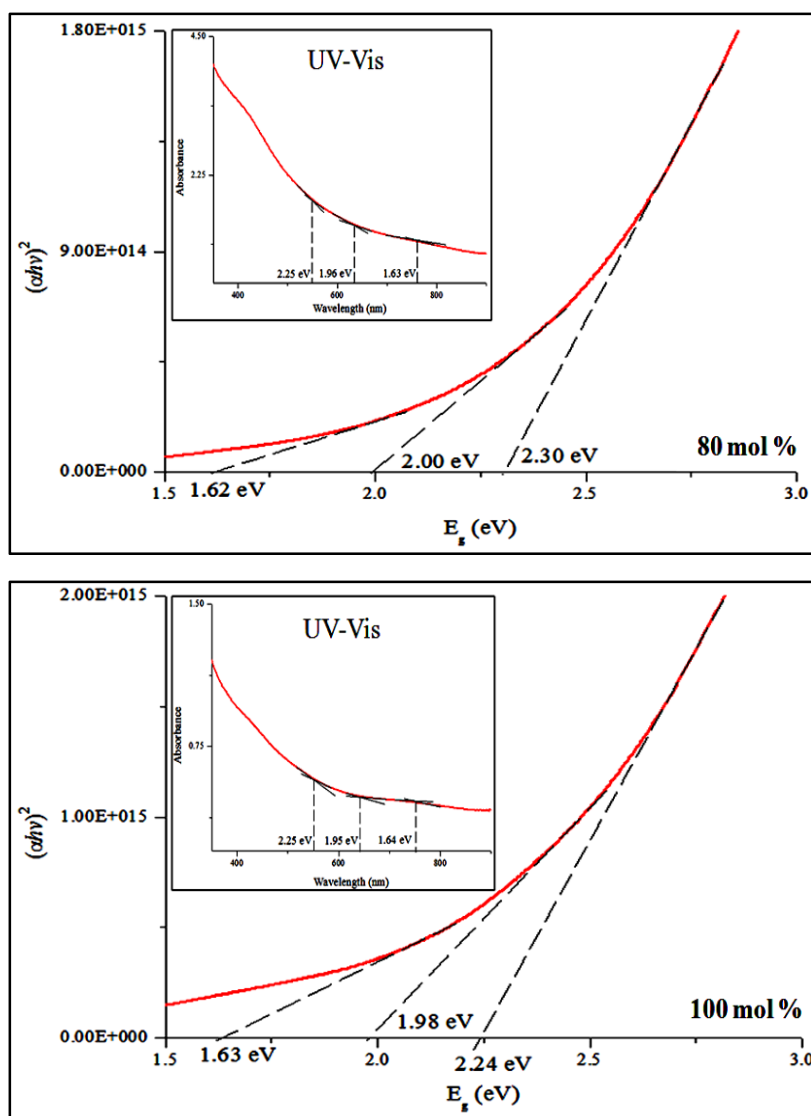
Figure 4.23: Tauc plot for 10, 20, 40, 80 and 100 mol% of Fe-doped thin films and the inset UV-Vis to confirm the band gap of the Fe-doped thin films.

4.3.8   Photoelectrochemical (PEC) Water Splitting Studies

Photoelectrochemical study had been carried out to evaluate the photocatalytic properties of the thin film under solar irradiation. Three types of experiments had been carried out namely linear sweep voltammetry (LSV), electrochemical impedance study (EIS) and Mott-Schottky plot. From the J-V

curves as shown in Figure 4.24, all thin films showed the presence of current density even in the dark conditions which possibly cause by the thin films itself can conduct electricity even without the presence of light. The presence of oxidized dopant, which were the Fe^{2+}/Fe^{3+}, may allow the electron transfer process occur and generate the current. Other than that, due to extra hole from the oxidized dopant may cause the enhancement of delocalization of electron (Neamen, 2012). This also could be the reason why the current density in the dark condition were close but not equal to the current in the light condition for all Fe-doped thin films. The 40 mol% Fe-doped thin film generated the highest current density of 1.353 mA/cm^2 at 0.6 V in the dark condition followed by 20, 80, 10 and 100 mol% Fe-doped thin films at current density of 1.120, 0.568, 0.559 and 0.332 mA/cm^2, respectively. On the other hand, when the light is on, the photocurrent density of all thin films was also increased gradually from – 0.6 to 0.6 V. Similarly, 40 mol% Fe-doped thin film able to generate the highest photocurrent density of 1.645 mA/cm^2 followed by 20, 80, 10 and 100 mol% with photocurrent density of 1.220, 0.811, 0.624 and 0.350 mA/cm^2, respectively. The current density generated in the dark and light conditions were tabulated in Table 4.5. It was proposed that the present of Fe^{2+}/Fe^{3+} in the 10, 20 and 40 mol% Fe-doped thin film can effectively enhance the electron transfer process. The Fe^{2+} is ready to transfer the electron to Fe^{3+}. The photocurrent density will be increased concomitantly (Miseki and Sayama, 2012). The presence of Fe^{2+}/Fe^{3+} could enhance the photocatalytic activity due to electron accepting effect from the reduction of Fe^{3+} to Fe^{2+} during hydroxide oxidation. This phenomenon will

minimize the reduction of the Fe-doped thin films during the redox process which will cause the thin film to exhaust slower compared to Fe-doped thin film without the presence of Fe^{2+}/Fe^{3+} (Arai et al., 2007). The Fe^{2+}/Fe^{3+} also acts as redox mediator where it can promote the oxidation of OH^- from the reduction for Fe^{3+} to Fe^{2+} (Miseki and Sayama, 2012). Apart from that, Fe^{3+} has strong electron trapping ability where it may oxidize the OH^- while Fe^{2+} has electron donating ability which caused reduction of water at high pH (Wang et al., 2017). The XPS spectrum of the 10 mol% Fe-doped thin film also had showed the present of low intensity of Fe^{2+}/Fe^{3+}. This observation can be used to explain why the 10 mol% Fe-doped thin film gave a slightly better performance when compared to 100 mol% Fe-doped thin film. It was also observed that 80 mol% had a better photocurrent density compare to the 10 mol% even though there was only Fe^{3+}. This means too small amount of dopant may not be optimal in enhancing the photocatalytic activity.
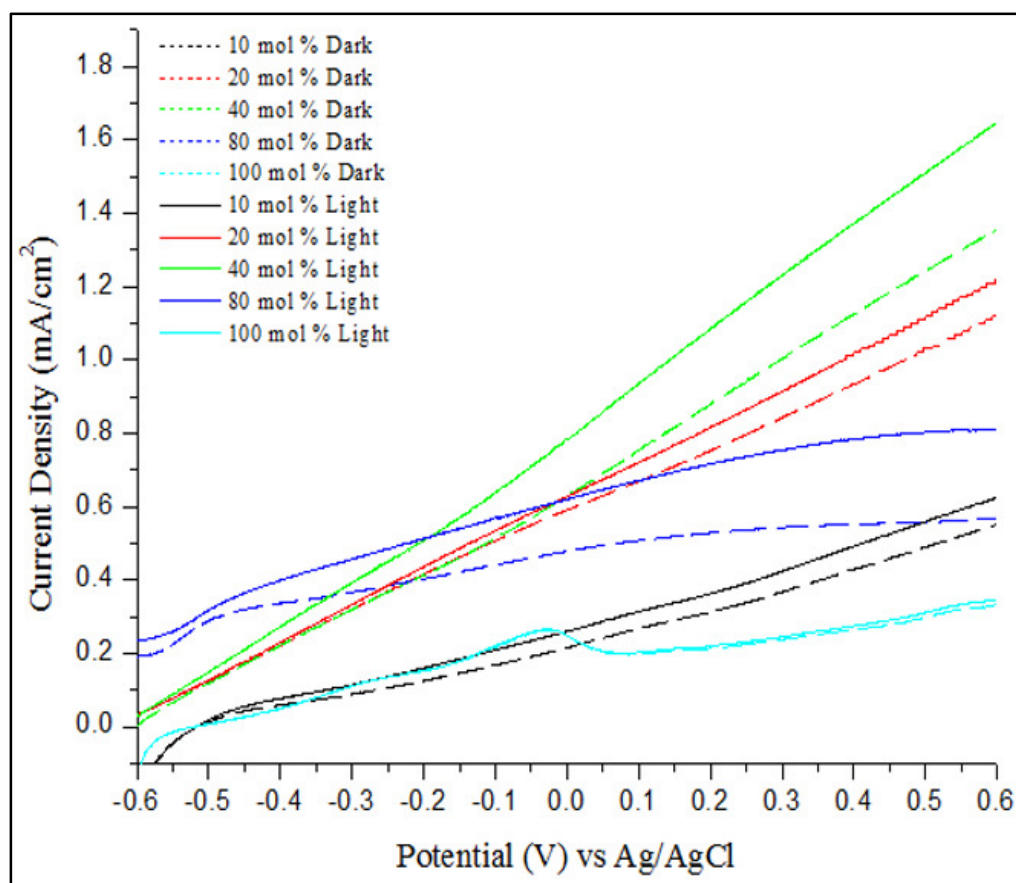
Figure 4.24: J-V curve for various mol% Fe-doped thin films.

The electrochemical impedance spectroscopy was analyzed to produce Bode and Nyquist plot for both dark and light conditions. The diameter size of the Nyquist plot is proportional with the impedance of the working electrode. It was observed in the Figure 4.25 that the 40 mol% Fe-doped thin film consisting the lowest thin film impedance. This observation could be due to the presence of Fe^{2+}/Fe^{3+} in thin film could enhance the electron flow process. As compared to 80

and 100 mol% Fe-doped thin films, which do not consists Fe^{2+}, the electron flow was less effective. Moreover, according to Van Zeghbroeck, the thin film resistance is $R_s = \frac{r}{t}$, where R_s, r and t is the thin film resistance, material resistivity and thin film thickness (Van Zeghbroeck, 2004). The thin film thickness can be referred at Figure 4.16 to 4.20 (b) and in Table 4.4. Based on the formula, the theoretical impedance of 100 mol% should be higher than 80 mol% since the thin film is thinner. However from the experiment, the 80 mol% Fe-doped thin film has larger impedance despite of having larger thickness compare to 100 mol% Fe-doped thin film. The actual reason for this phenomenon is still unclear. It was proposed that there is a possibility that high amount of dopant may cause the electron scattering by the dopant and therefore lower the electron mobility (Van Zeghbroeck, 2004). Nevertheless, the photocurrent density of 80 mol% is better as it showed a better light response compare to 100 mol% Fe-doped thin film. Furthermore, the 80 mol% Fe-doped thin film has the smallest particle size may allowed it to have more active site for the water splitting process which could enhance the photocatalytic activity.
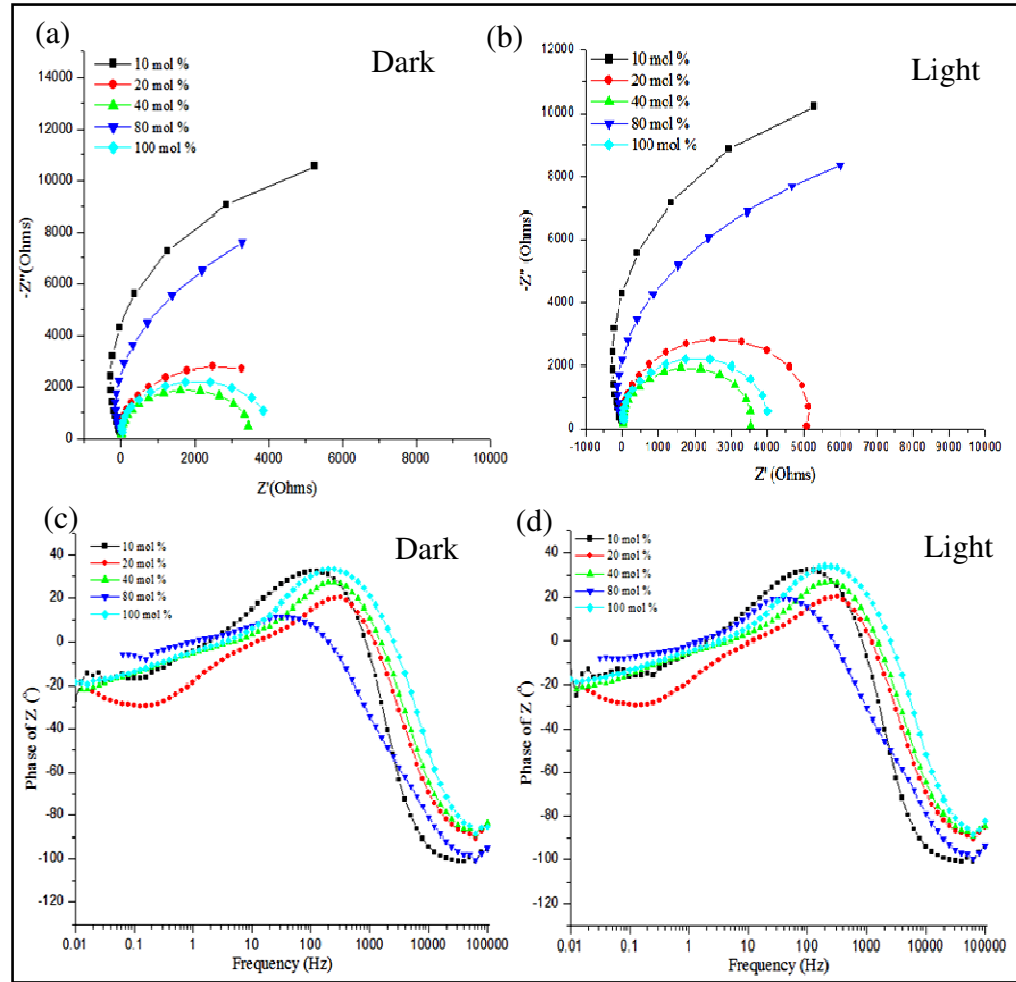
Figure 4.25: (a, b) Nyquist plot and (c,d) Bode plot for various mol% Fe-doped thin films in different conditions (dark and light).

The photocurrent density, photosensitivity, frequency maxima and charge life time can be calculated and the results were tabulated in Table 4.5. Even though the 40 mol% Fe-doped thin film showed the best photocurrent density, but 80 mol% has shown the lowest charge recombination rate based on the Bode plot and in other words it has the highest life time value. We proposed the presence of Fe^{2+}/Fe^{3+} not only increase the electron transfer efficiency but also could increase the charge recombination rate during the electron hole trapping process causing

smaller life time value. This was the reason why the thin film showed a relatively small charge lifetime at the range of 0.50 – 5.03 ms. Despite of having a lot of factors that may affect the photocurrent density such as thin film thickness, morphology and impedance, it was largely affected by the Fe-dopant oxidation state.

Table 4.5: Comparisons of PEC activities for various mol% Fe-doped thin films

Mol %	J_D (mA/cm^2) At 1.23 V vs RHE	J_L (mA/cm^2) At 1.23 V vs RHE	Photo-sensitivity J_L/J_D At 1.23V vs RHE	Frequency Maxima Hz	Life time $\tau = 1/2\pi\upsilon$ (ms)
10	0.559	0.624	1.155	124.59	1.28
20	1.120	1.220	1.086	316.51	0.50
40	1.353	1.645	1.037	254.83	0.62
80	0.568	0.811	1.390	31.62	5.03
100	0.332	0.350	1.054	217.37	0.73

The charge density was calculated using equation Eq. (4.3). The relative permittivity of the thin film was assumed to be 10. The slope value was obtained from the Mott-Schottky plot as shown in Figure 4.26. From the calculation, it was observed that the charge density for 10, 20, 40, 80 and 100 mol% Fe-doped thin film were 1.107×10^{19}, 4.407×10^{20}, 4.290×10^{20}, 2.207×10^{18} and 1.702×10^{19} cm^{-3}, respectively. The negative slope from the Mott-Schottky plot had indicated that the thin film is a p-type thin film (Lim et al., 2019)

$$N_D = \frac{1.41 \times 10^{32} \ (cm \times F^{-2} \times V^{-1})}{\varepsilon_r \times A^2 \ (cm^4) \times slope \ (F^{-2} \times V^{-1})} \qquad \text{Eq. (4.3)}$$
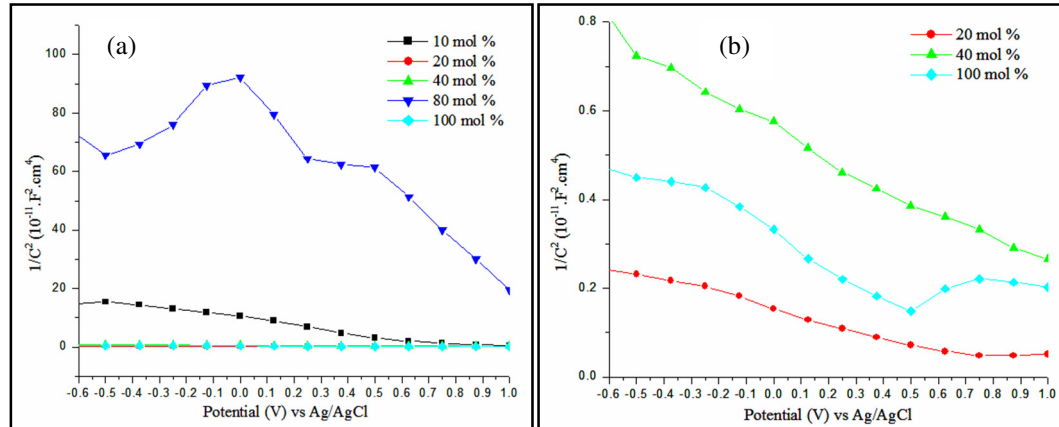
Figure 4.26: (a) Mott-Schottky plot for Fe-doped thin films; (b) Expanded view of Mott-Schottky plot for 20, 40 & 100 mol% Fe-doped thin films under light condition.

Table 4.6: Charge densities for Fe-doped thin films

Percentage of Fe doping (%)	Charge densities (cm^{-3})
10	1.107×10^{19}
20	4.047×10^{20}
40	4.290×10^{20}
80	2.207×10^{18}
100	1.702×10^{19}

4.3.9 Mechanism of Electron Transfer Process for Fe-series

The schematic diagram of the relative material in the thin film is shown in Figure 4.27. The band position for each of the material was calculated based on the literature by Dong's work in 2014. The theoretical valence band edge potential (E_{VB}) and the conduction band edge potential (E_{CB}) of semiconductor material can be calculated by using the equations 4.4 and 4.5

$$E_{CB} = X - E_c - 0.5E_g \quad \text{Eq. (4.4)}$$

101

$$E_{VB} = E_{CB} + E_g \qquad \text{Eq. (4.5)}$$

The X represents the absolute electronegativity of the material whereas E_c is the energy of the free electron in the hydrogen scale (4.5 eV). On the other hand, E_g is the band gap of the material. The electronegativity was calculated from the electron affinity and the first ionization energy of each of the elements of the material. An example for calculations for MoS_2 is shown as following:

Electron affinity of Mo, E_{EA} = 72.1 kJ/mol / 96.48 = 0.747 eV

First ionization of Mo, E_{ion} = 684.3 kJ/mol / 96.48 = 7.093 eV

Electronegativity of Mo, X_{Mo} = 0.5(E_{EA} + E_{ion}) = 3.92 eV

Similar calculations for S where the electronegativity of S, X_s = 6.22 eV

Therefore, the electronegativity for MoS_2 of X_{MoS_2} is:

$$X_{MoS_2} = (X_{Mo} \times X_S \times X_S)^{1/n}$$

$$= (3.92 \text{ eV} \times 6.22 \text{ eV} \times 6.22 \text{ eV})^{1/3}$$

$$= 5.33 \text{ eV}$$

The calculations details for all types of materials can be referred to appendix A. Thus by substituting the values, the conduction band potential and valence band potential were determined as -0.12 and 1.78 eV, respectively. As for Mo_2S_3, the conduction and valence band potential would be -0.48 and 1.82 eV, respectively. The conduction and valence band potential for $Fe(MoS_2)_2$ were -0.18 and 1.78 eV, respectively. The valence and conduction band potential for all

materials that were present in thin films are shown in Figure 4.27. As observed in Figure 4.27, the coupling of three different materials in the thin films could extend the visible light absorptions and improves the charge separation by the photoinduced heterojunction interfaces. The electron transfer process between different materials as shown in Figure 4.27 facilitate the charge separation mechanism at the heterojunction interface, and therefore suppresses the electron-holes recombination during light irradiation. During light irradiation, the electron holes separation occurs for all of the material. The electrons flow from the highest conduction band potential to the lowest conduction band and finally to the fluorine-doped tin oxide substrate (FTO). Electrons will eventually flow to the platinum electrode (Pt) where oxidation of hydrogen ions occurs to generate the hydrogen. Apart from electrons, the holes will also flow to the MoS_2 for water splitting process. This is known as the electron holes trapping process because it suppress (minimize) the electron-hole recombination as shown in the proposed z-scheme mechanism in Figure 4.27 thus improve the photocatalytic process.
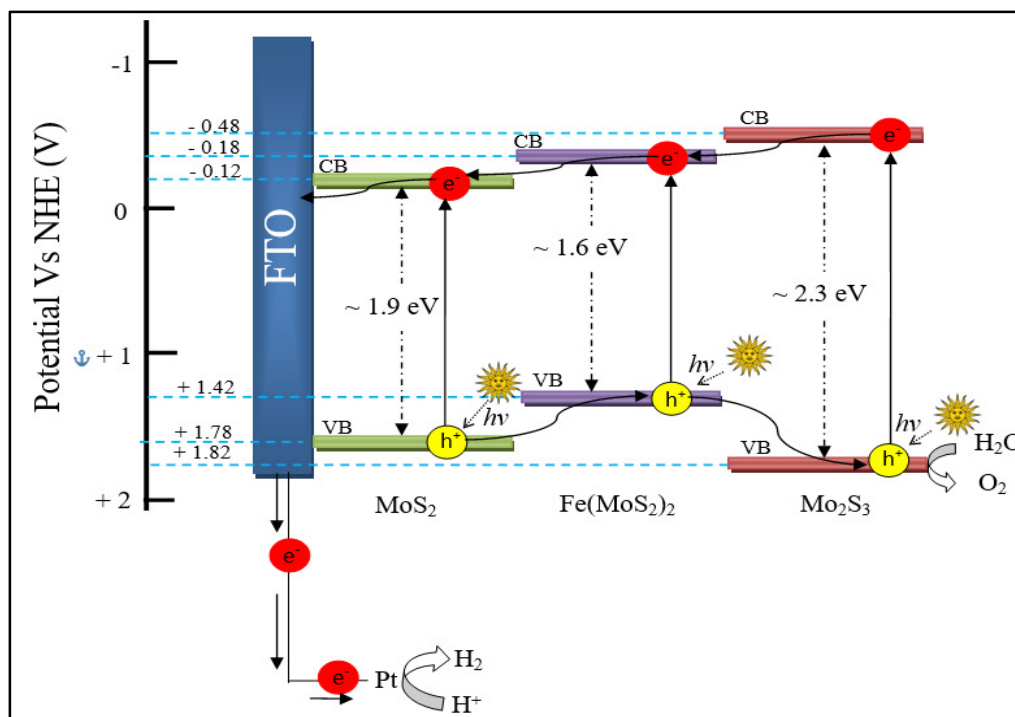
Figure 4.27: Proposed Z-scheme mechanism for Fe-doped thin film.

4.4 Characterization of Thin Films Prepared from $[(\eta^5\text{-Cp})Mo(SMe)_2]_2$ (2) with Different Mol% of Cobaltocene, Cp_2Co (Cp = cyclopentadiene)

Similar to iron series, cobalt series thin films were analyzed with XRD, Raman spectroscopy, XPS, EDX, AFM, SEM, UV-Vis spectroscopy as well as photoelectrochemical (PEC) water splitting studies. It was observed that the Co series thin films thickness are generally thicker as compared to the Fe series. Thus, Co series also has a better absorbance value compared to the Fe series. Moreover, the thin films also have better PEC water splitting activity as compared to the Fe series.

4.4.1   X-ray Diffraction Analysis (XRD)

The XRD pattern of the Co-doped thin films in various mol% Co-doping are shown in Figure 4.28 while the list of the characteristics peaks for different structures are tabulated in Table 4.7. Similar to Fe–doped thin films, even though the intensity of the FTO is very strong, the weak XRD pattern of rhombohedral MoS_2 (ICDD 01-077-0341) and monoclinic Mo_2S_3 (ICDD 01-078-1332) were indicated present in the thin film. The thin films also matched with the XRD pattern of monoclinic $Co(MoS_2)_2$ (ICDD 01-070-8640) where the characteristic peaks are observed at 15.44^o, 17.18^o, 25.72^o, 34.16^o, 37.96^o, 51.71^o and 65.66^o corresponded to (002), (-202), (-113), (221), (312), (600) and (-428), respectively. The comparison of 10 mol% Co-doped thin film, MoS_2/Mo_2S_3 and tetragonal SnO_2 (ICDD 01-077-052) from the FTO substrate is shown in Figure 4.29. The peaks at 2θ of 15.44^o and 25.72^o only found in $Co(MoS_2)_2$ which means the Co atom could be located in the interstitial site of MoS_2 between two layers of sulfur atoms (Dai et al., 2015; Feng et al., 2015; Topsøe et al., 1981; Xiong et al., 2018).
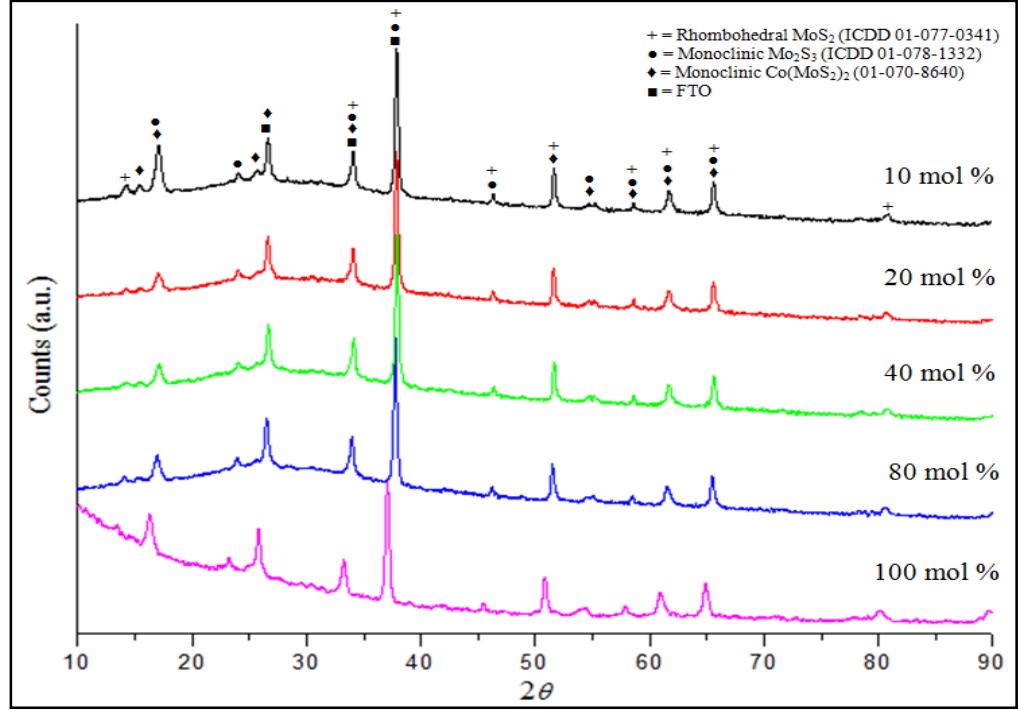
Figure 4.28: XRD pattern for 10, 20, 40, 80 and 100 mol% of Co-doped thin films.

Table 4.7: XRD characteristics peak list for Co-doped thin film

2θ	Assigned Peak
14.32	MoS_2
15.44	$Co(MoS_2)_2$
17.08	Mo_2S_3/ $Co(MoS_2)_2$
24.03	Mo_2S_3
25.72	$Co(MoS_2)_2$
26.62	$Co(MoS_2)_2$/ FTO
34.08	MoS_2 / Mo_2S_3 / $Co(MoS_2)_2$/ FTO
37.88	MoS_2 / Mo_2S_3/ $Co(MoS_2)_2$/ FTO
46.33	Mo_2S_3/ $Co(MoS_2)_2$
51.61	MoS_2/ Mo_2S_3/ $Co(MoS_2)_2$
55.19	Mo_2S_3/ $Co(MoS_2)_2$
58.59	MoS_2/ Mo_2S_3/ $Co(MoS_2)_2$
61.69	MoS_2/ Mo_2S_3/ $Co(MoS_2)_2$
65.56	MoS_2/ Mo_2S_3/ $Co(MoS_2)_2$
80.58	MoS_2
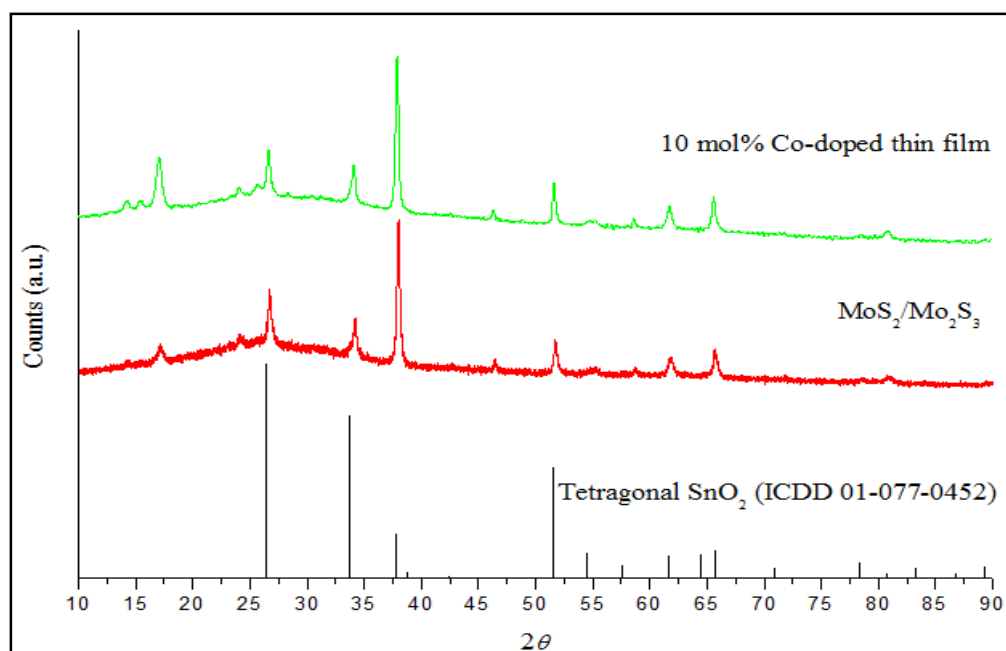
Figure 4.29: Comparison of 10 mol% Co-doped thin film, MoS_2/Mo_2S_3 and tetragonal SnO_2 (ICDD 01-077-052).

4.4.2   Raman Spectroscopy

The Co-doped thin films had been analyzed with Raman spectroscopy and its spectrum is shown in Figure 4.30. The Raman spectrum for Co-doped thin film is similar with the 80 mol% Fe-doped thin film. However, the peaks at 373.17 (E^1_{2g}) and 398.74 cm^{-1} (A_{1g}) which corresponded to MoS_2 which have a difference in value by 25.57 cm^{-1} indicating that it is a quadrilayer MoS_2. Similar observation was also reported by Li et al. (2012). On the other hand, the amorphous Mo-S bridging were recorded at 337.89 and 452.82 cm^{-1} (Khaemba, Neville and Morina, 2016) where the similar peak was also recorded in the Raman spectrum for 80 mol% Fe-doped thin film. Since Co-doped thin film and the Fe-

doped thin film have almost identical Raman spectrum, thus we proposed the absorption peak at 347.5 cm^{-1} is the Co-S bridging mode.
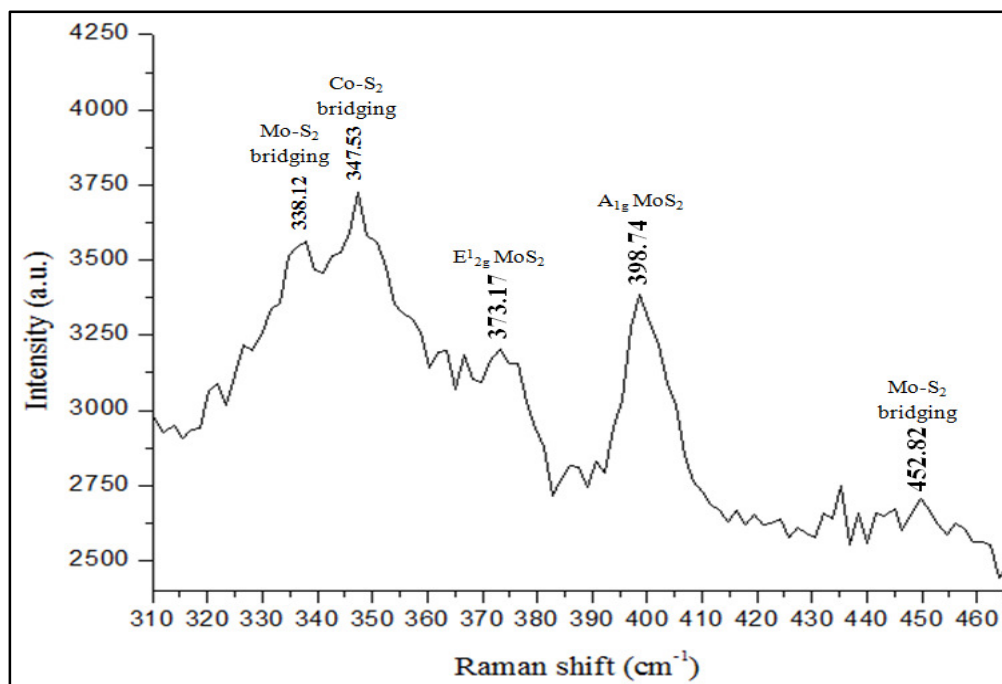
Figure 4.30: Raman spectroscopy of 100 mol % Co-doped thin film.

4.4.3   X-ray Photoelectron Spectroscopy (XPS) Analysis

The XPS spectrum for 10 and 100 mol% Co-doped thin films can be observed in Figure 4.31 and it was chosen for XPS analysis because it has a homogenous morphology. Despite of having different mol% of Co dopant incorporated into the thin film, both of the thin film had showed a similar XPS spectrum of element Co, Mo and S. It was observed in Figure 4.31 (a) that the peak at the binding energies of 780.89 and 796.39 eV were corresponded to the

Co^{2+} $2p_{3/2}$ and Co^{2+} $2p_{1/2}$ (Zheng et al., 2018; Ye et al., 2016). The peaks that were corresponded to CoMoS were at the binding energies of 777.90 and 798.94 eV. This finding indicated that the Mo atom in MoS_2/Mo_2S_3 lattice structure was substituted by the Co atom (Zheng et al., 2018). The satellite peaks in this figure are represented by the peak at binding energy of 783.13 and 803.01 eV (Ye et al., 2016). Satellite peak occurs when the core electron was photoionized and interacted with the valence electrons. The spectrum in Figure 4.31 (b) had showed that Mo^{3+} and Mo^{4+} are present in the thin film. The binding energies of Mo^{4+} $3d_{5/2}$ and Mo^{4+} $3d_{3/2}$ is at 228.20 and 231.69 eV respectively whereas the binding energies of Mo^{3+} $3d_{5/2}$ and Mo^{3+} $3d_{3/2}$ is at 231.69 and 232.72 eV respectively (Lim et al., 2019; Zhang et al., 2018; Zheng et al., 2018; Roger et al., 2017). The S $2p_{3/2}$ and S $2p_{1/2}$ as shown in Figure 4.31 (c) were assigned to the peak at the binding energies of 161.46 and 162.70 eV, respectively (Zheng et al., 2018).
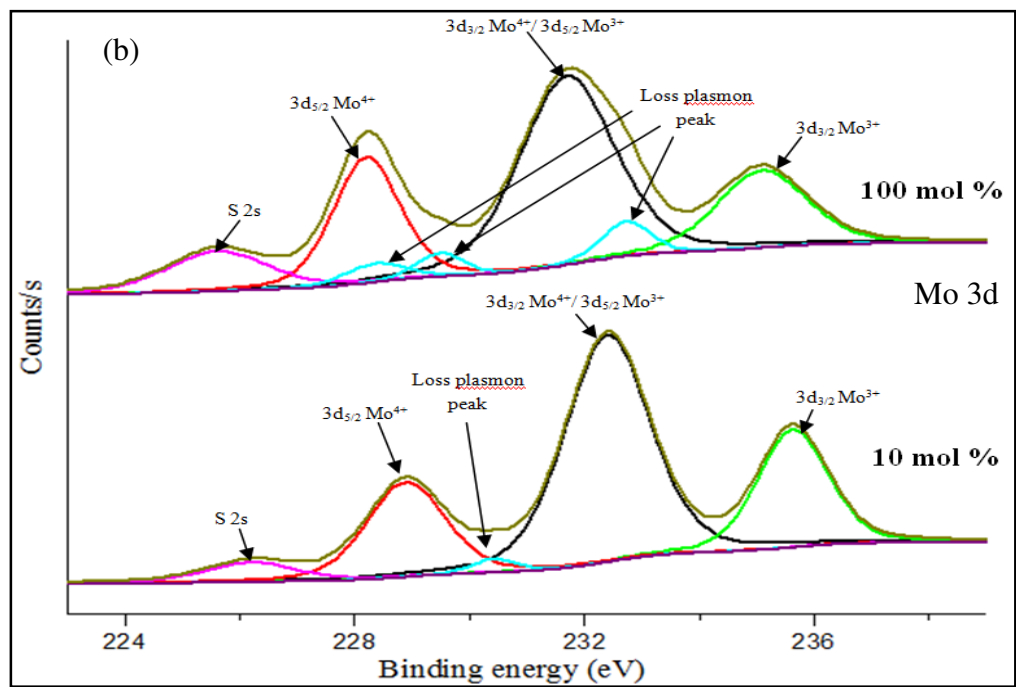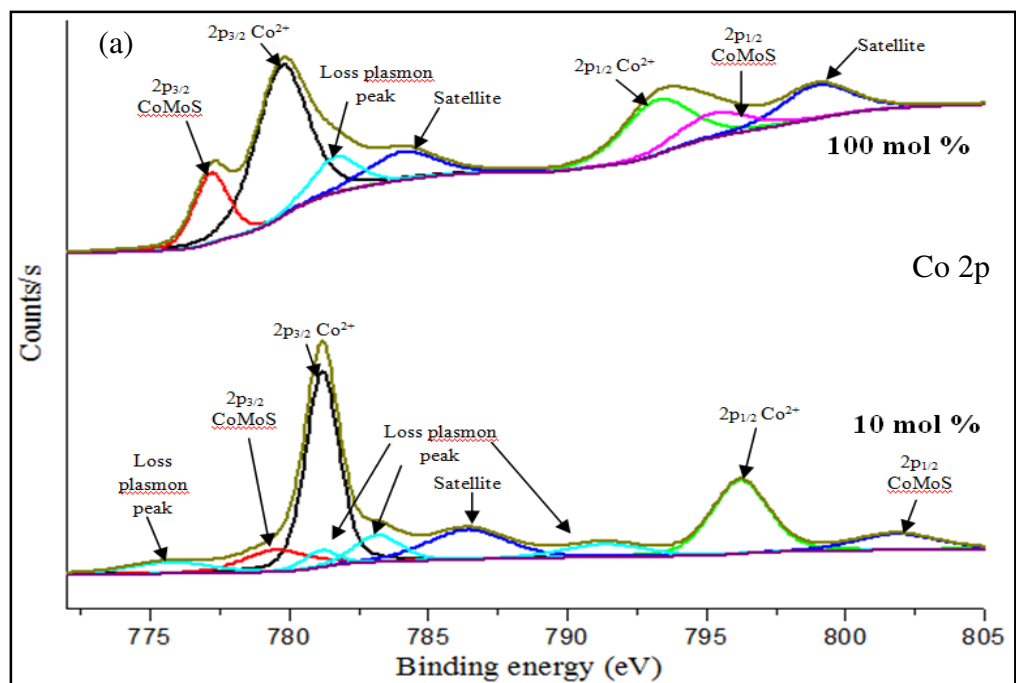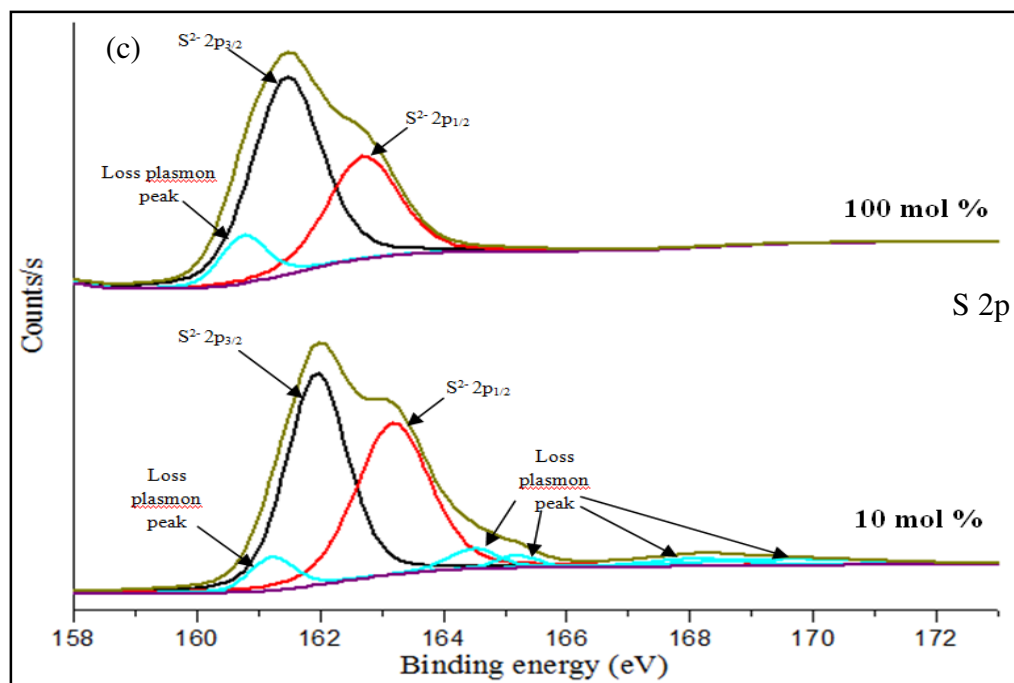
Figure 4.31: XPS spectrum for (a) Co 2p, (b) Mo 3d and (c) S 2p for 100 mol %
Co-doped thin film.

4.4.4 Energy Dispersive X-ray (EDX) Spectroscopy and Elemental Mapping Analysis

The Co-doped thin films had been analyzed with the EDX and elemental mapping analyses. It was observed that the atomic percentage (at %) of Co incorporated into thin films shows a trend where increasing of cobaltocene in the feed will increase the at % of Co as well. The cobaltocene with 10, 20, 40, 80 and 100 mol% in the feed gave 0.95, 1.92, 2.41, 5.06 and 5.85 at% of Co, respectively. Table 4.8 shows the at % of Mo, Co and S for different mol% Co-doped thin film. Figures 4.32 and 4.33 represent the EDX spectrum and elemental mapping, for

the 10, 20, 40, 80 and 100 mol% of Co-doped thin films. As shown in the elemental mapping Mo, Co and S are distributed evenly on the film.

Table 4.8: EDX result for various mol% of Co-doped thin films

Mol % of Co-doped thin film	Elements	Atomic % (at %)
10	Mo	39.02
	Co	0.95
	S	60.04
20	Mo	40.24
	Co	1.92
	S	57.84
40	Mo	38.01
	Co	2.41
	S	59.37
80	Mo	38.82
	Co	5.06
	S	56.12
100	Mo	36.64
	Co	5.85
	S	57.51
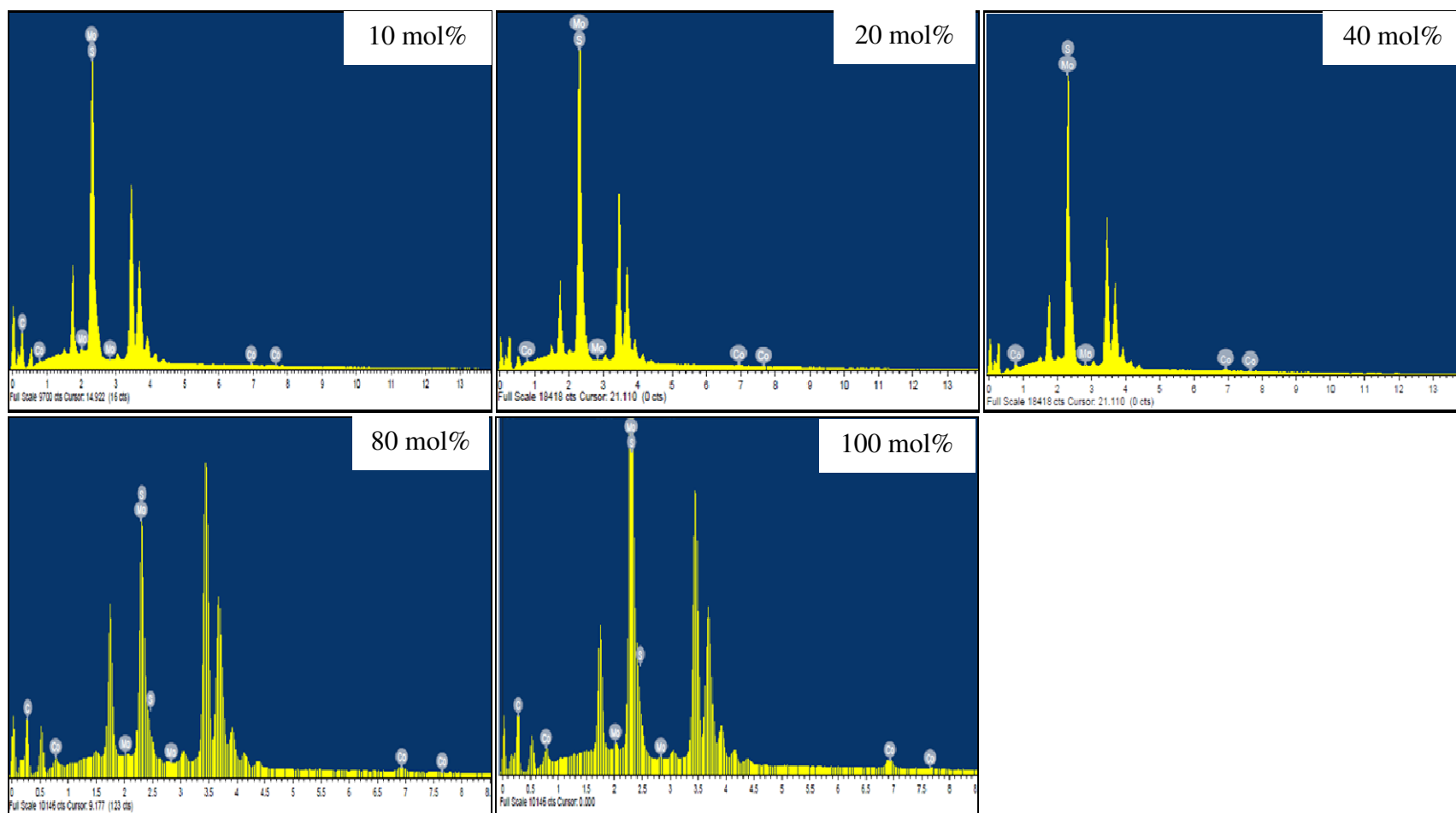
Figure 4.32: EDX graph for various mol% Co-doped thin films.

10 mol % Co-doped thin film
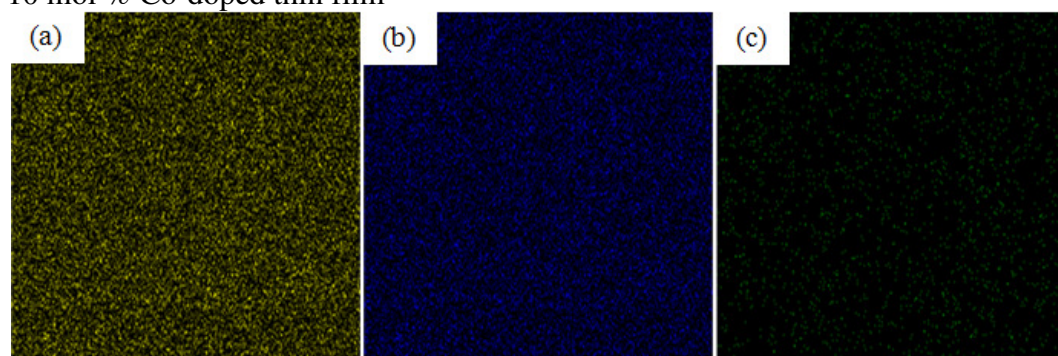
20 mol % Co-doped thin film
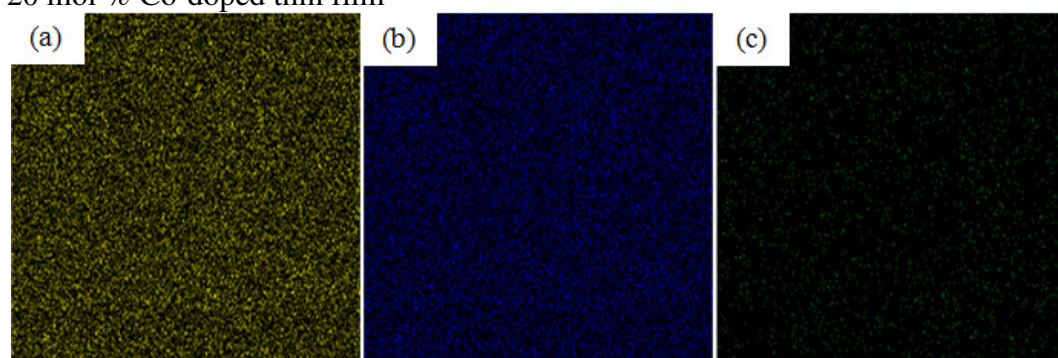
40 mol % Co-doped thin film
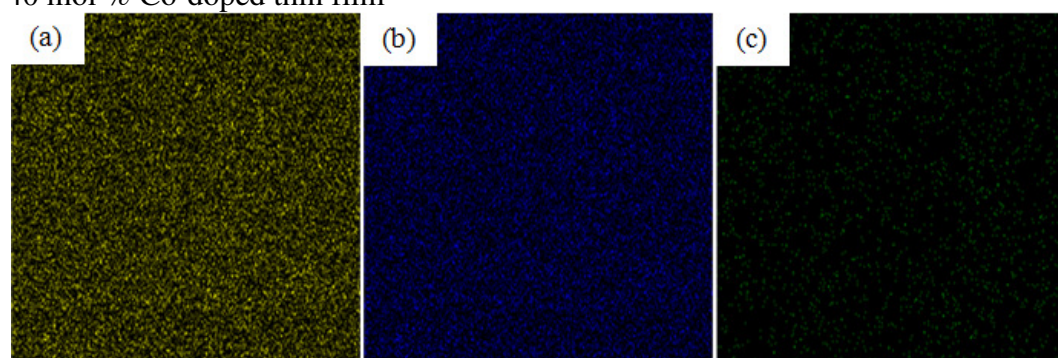
80 mol % Co-doped thin film
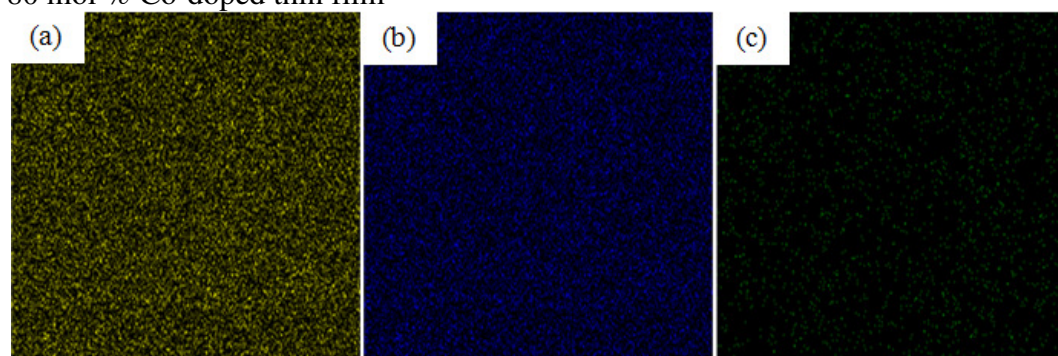
100 mol % Co-doped thin film
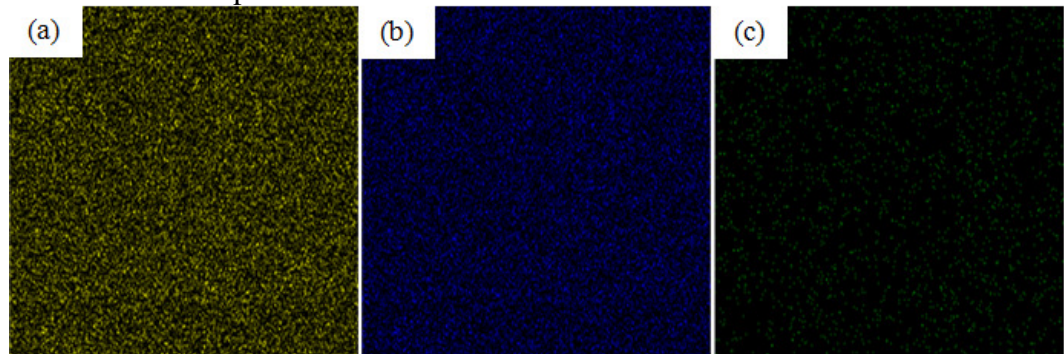
Figure 4.33: EDX elemental mapping for various mol% Fe-doped thin film (a) sulfur, (b) molybdenum and (c) iron.

4.4.5 Atomic Force Microscopy (AFM) Analysis

The surface morphology for Co-doped thin films were found to be similar with Fe-doped film where the granular surface morphology was observed (see 2D images in Figure 4.34). Figure 4.35 shows the line profile for 10, 20, 40, 80 and 100 mol% of Co-doped thin films where it was observed that all thin films were distributed homogenously. The 3D images in Figure 4.36 had showed that the granular surface morphology was actually made up of standing rod morphology with valley between them which was similar to Fe-doped thin films AFM analyses. The roughness of all thin films in the Co series was tabulated in Table 4.9 where it was observed that all thin films had small roughness value with slight differences.

10 mol%

20 mol %

40 mol%

80 mol%
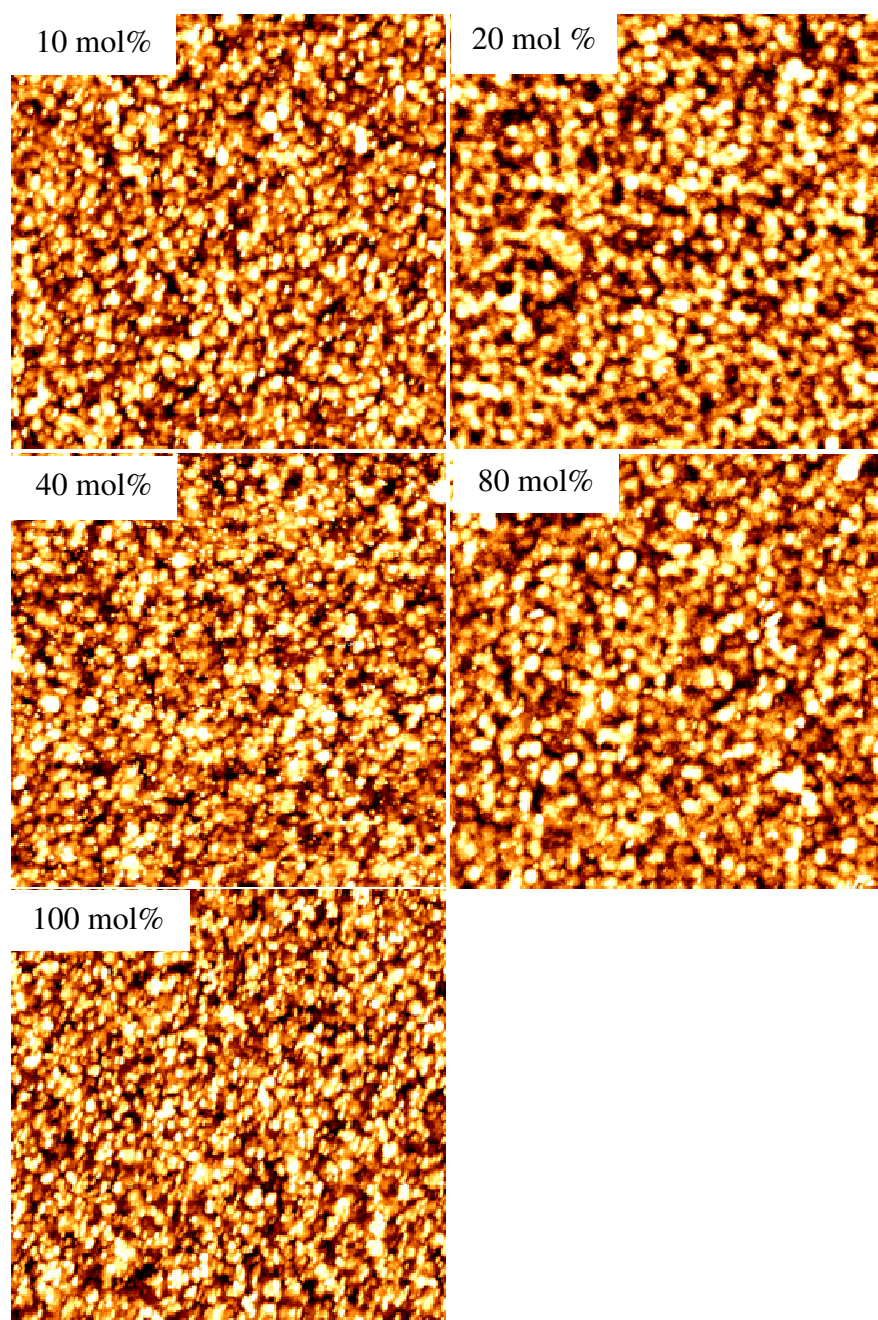
100 mol%

Figure 4.34: AFM 2D images for 10, 20, 40, 80 and 100 mol % of Co-doped thin films.
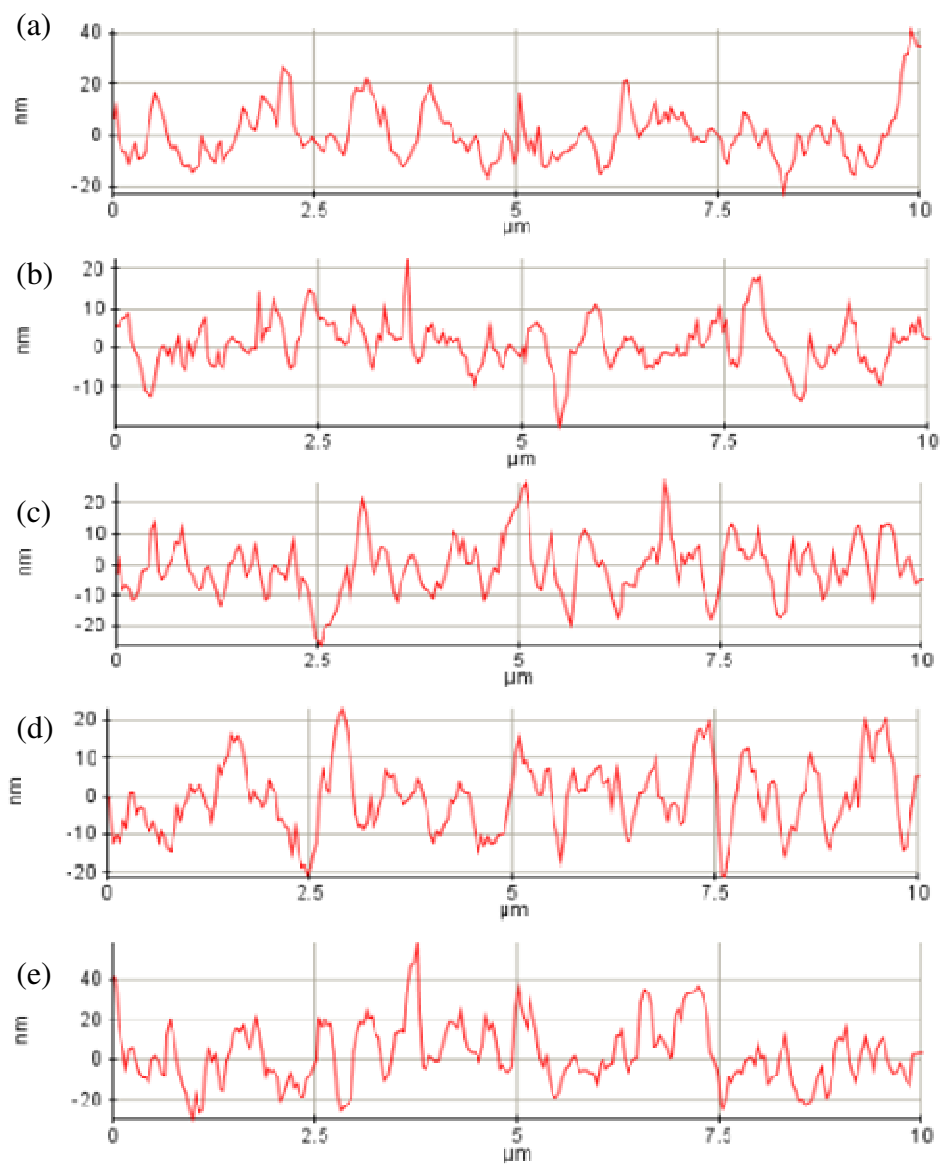
Figure 4.35: Line profile for (a) 10, (b) 20, (c) 40, (d) 80 and (e) 100 mol% of Co-doped thin films.
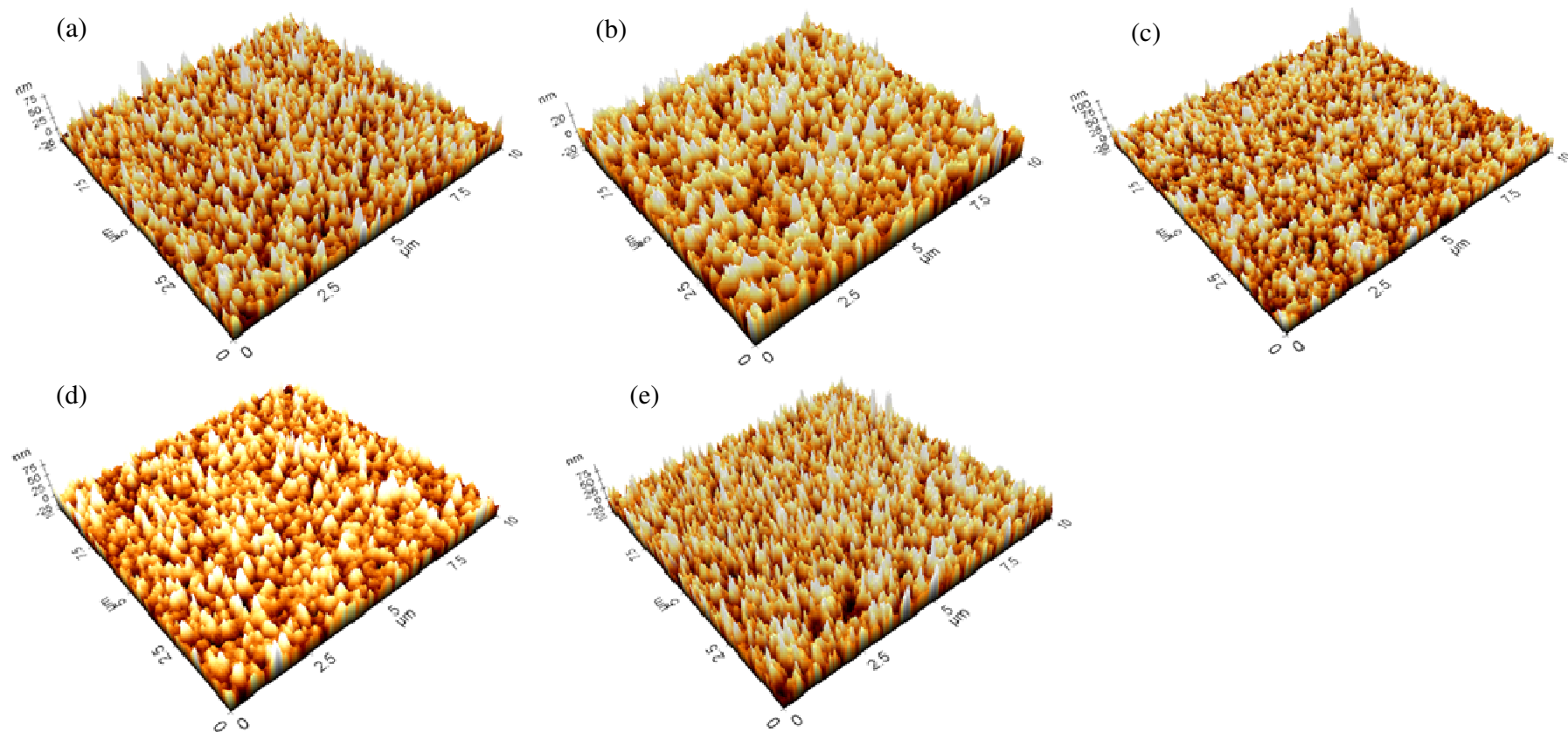
Figure 4.36: AFM 3D images for (a) 10 (b) 20, (c) 40 (d) 80 and (e) 100 mol% of Co-doped thin films.

Table 4.9: Ra, Rq, Rpv, Rv and Rp for various mol% of Co-doped thin films

Mol %	Statistics	Value (nm)
10	Roughness average, Ra, (nm)	7.925
	Root mean square, Rq, (nm)	10.340
	Maximum profile height, Rpv, (nm)	64.017
	Maximum valley depth, Rv, (nm)	23.008
	Maximum peak height, Rp, (nm)	41.009
20	Roughness average, Ra, (nm)	4.610
	Root mean square, Rq, (nm)	6.092
	Maximum profile height, Rpv, (nm)	42.147
	Maximum valley depth, Rv, (nm)	19.724
	Maximum peak height, Rp, (nm)	22.423
40	Roughness average, Ra, (nm)	7.097
	Root mean square, Rq, (nm)	9.167
	Maximum profile height, Rpv, (nm)	52.722
	Maximum valley depth, Rv, (nm)	26.115
	Maximum peak height, Rp, (nm)	26.607
80	Roughness average, Ra, (nm)	7.231
	Root mean square, Rq, (nm)	9.056
	Maximum profile height, Rpv, (nm)	44.051
	Maximum valley depth, Rv, (nm)	21.181
	Maximum peak heaigh, Rp, (nm)	22.870
100	Roughness average, Ra, (nm)	12.224
	Root mean square, Rq, (nm)	15.498
	Maximum profile height, Rpv, (nm)	87.843
	Maximum valley depth, Rv, (nm)	29.843
	Maximum peak height, Rp, (nm)	58.001

4.4.6 Scanning Electron Microscopy (SEM) Analysis

Scanning electron microscopy analysis had been carried out for Co-doped thin films and the images for their surface morphology as well as their cross-sectional thickness were shown in Figure 4.37 to 4.41. The rod-like and the granular morphologies are present in the SEM images for 10 mol% Co-doped thin film. As the doping of cobalt increases to 20 mol%, the rod-like morphology diminishes and the fine granular morphology with even distribution was formed instead. Despite of having different Co at % present in the thin films for the 20, 40, 80 and 100 mol% Co-doped thin films, their morphologies are similar. The cross-section thickness for 10, 20, 40, 80 and 100 mol% Co-doped thin films are 373, 430, 424, 416 and 485 nm, respectively. These observations indicated that Co dopant generally has a better growth promotional effect when compared to Fe dopant and different amount of Co-dopant that was incorporated into the thin film has a random effect on the thin film thickness. Similar to the Fe series, addition of different amount of Co dopant gave rise to balance the attractive Van der Waals force, repulsive steric force and electric-double-layer force which resulted in equilibrium film thickness (Clarke, 1989; Tanaka et al., 1994)
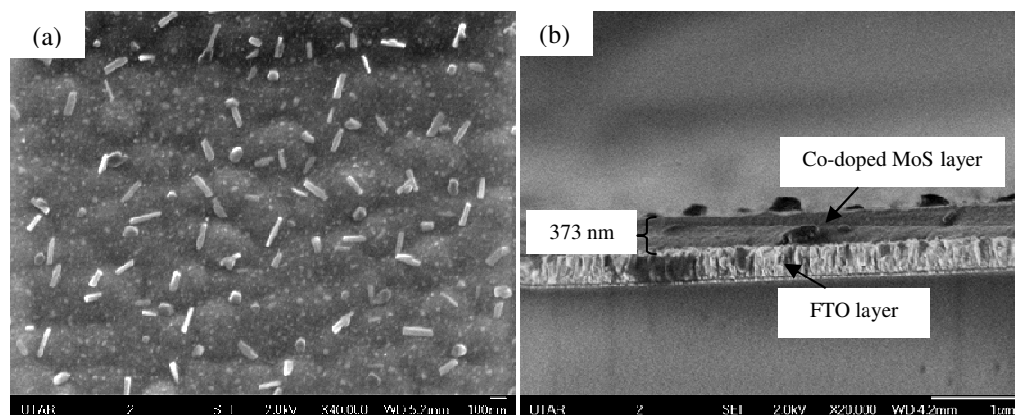
Figure 4.37: SEM images for 10 mol% Co-doped thin film for (a) surface morphology and (b) cross section thickness.
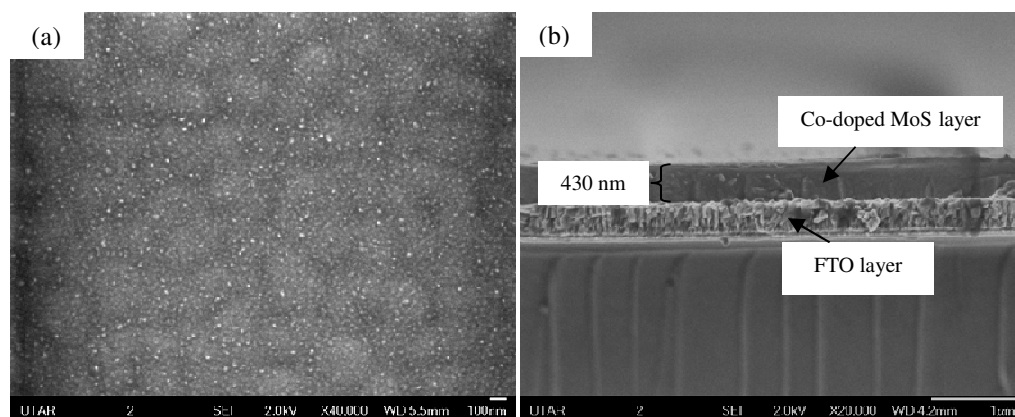
Figure 4.38: SEM images for 20 mol% Co-doped thin film for (a) surface morphology and (b) cross section thickness.
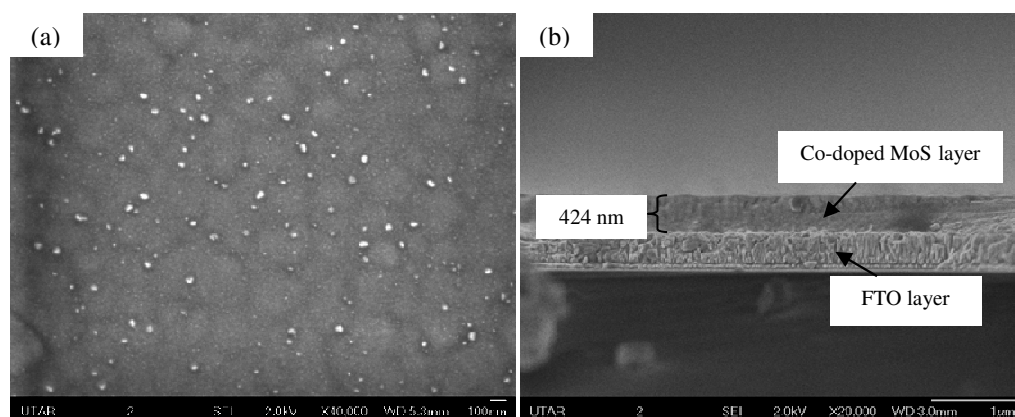
Figure 4.39: SEM images for 40 mol% Co-doped thin film for (a) surface morphology and (b) cross section thickness.
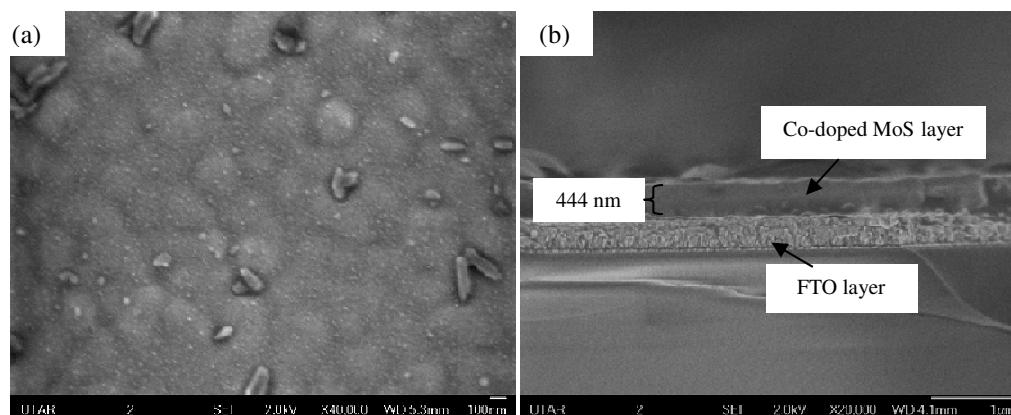
Figure 4.40: SEM images for 80 mol% Co-doped thin film for (a) surface morphology and (b) cross section thickness.
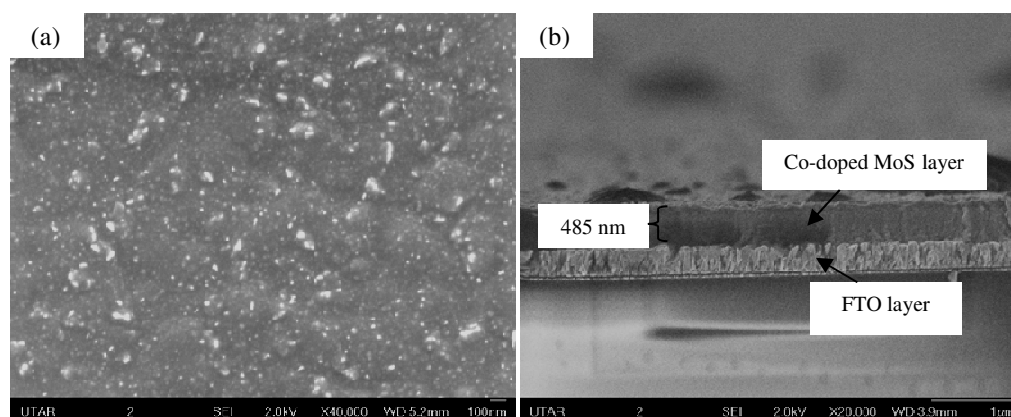
Figure 4.41: SEM images for 100 mol% Co-doped thin film for (a) surface morphology and (b) cross section thickness.

Histogram as shown in Figure 4.42 was plotted based on the SEM images to find out the majority of the particle sizes. Particle size is one of the factors that have an effect on the photoelectrochemical activity of the thin film during the PEC process. This is because the size is proportional to the surface area at the interface of the thin film and the surrounding electrolytes. It was observed in Figure 4.40 that the particle sizes of all the Co-doped thin films were generally smaller compared to the Fe-doped thin films. The particles sizes for 10, 20, 40, 80 and 100 mol% Co-doped thin films are 120, 40, 40, 20 and 40 nm, respectively.
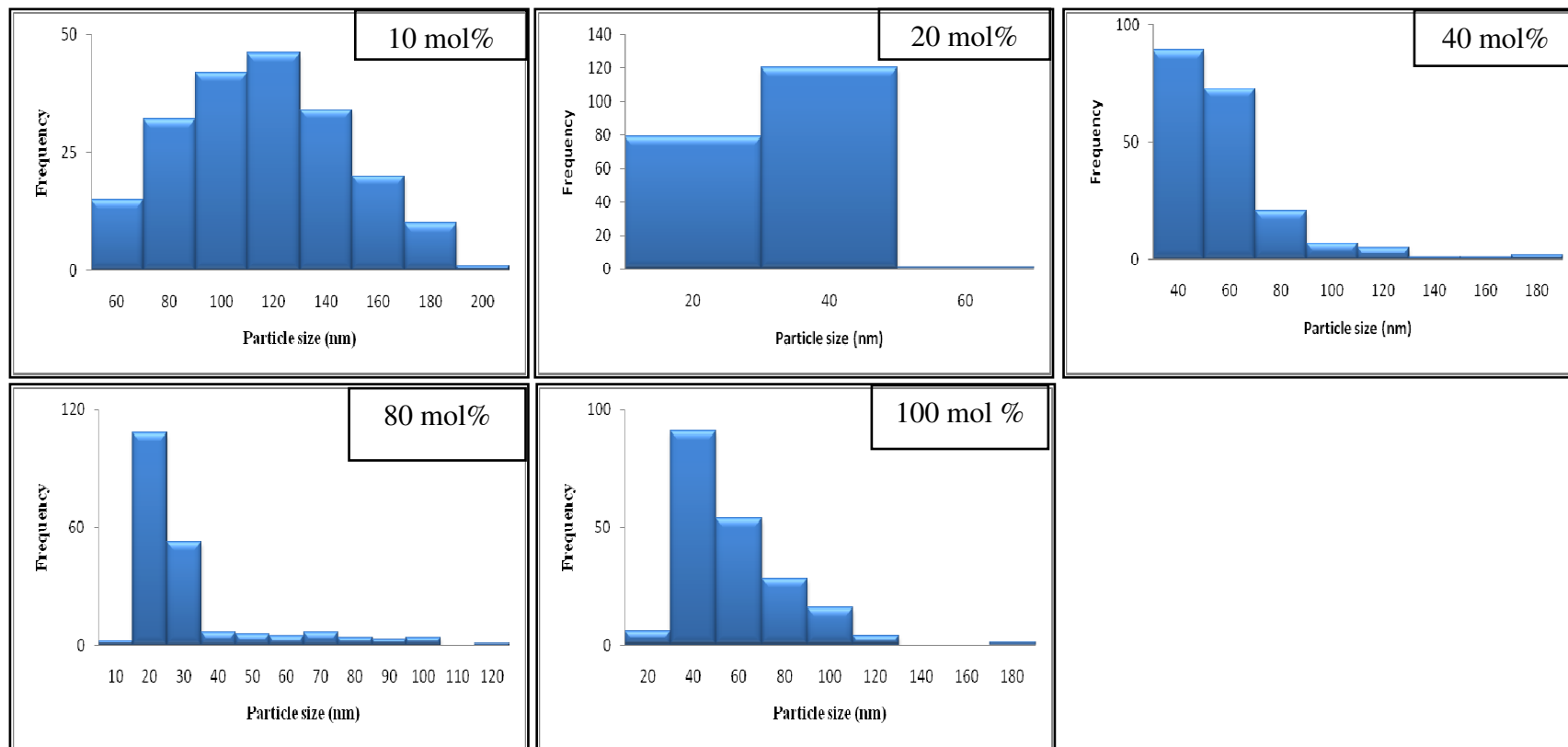
Figure 4.42: Histogram for various mol% Co-doped thin films.

4.4.7 UV-Vis Spectroscopy Analysis

The optical properties of the thin films were evaluated via UV-Vis spectroscopy. It was observed in the UV-Vis spectrum in Figure 4.43 that the 40 mol% Co-doped thin film had showed the highest absorptivity whereas the 80 mol% Co-doped thin film had showed the lowest absorptivity. The second highest absorptivity was the 100 mol% Co-doped thin film followed by the 20 and 10 mol% Co-doped thin films. It is noted that the absorbance value is not proportional to the thin film's thickness. We proposed that the insignificant difference in absorbance value could be due to the small difference in cross section thickness of the thin film. The difference in the absorbance value was largely due to absorption coefficient of the thin films. The band gap values were similarly determined as with the Fe-doped thin films. They were determined directly from the UV-Vis spectrum by using (Eq. 1) and Tauc plot method from (Eq. 2) as shown in chapter 4.3.7. The Tauc plots for all Co-doped thin films were shown in Figure 4.44. It was observed that both of these methods had showed that all thin films have three band gaps value which were corresponded to the material that were present in the thin films. The band gap at ~1.60, ~1.90 and 2.30 eV were corresponded to the $Co(MoS_2)_2$, MoS_2 and Mo_2S_3, respectively. The band gap values with different mol% of Co dopant incorporated into the thin films were tabulated in Table 4.10.
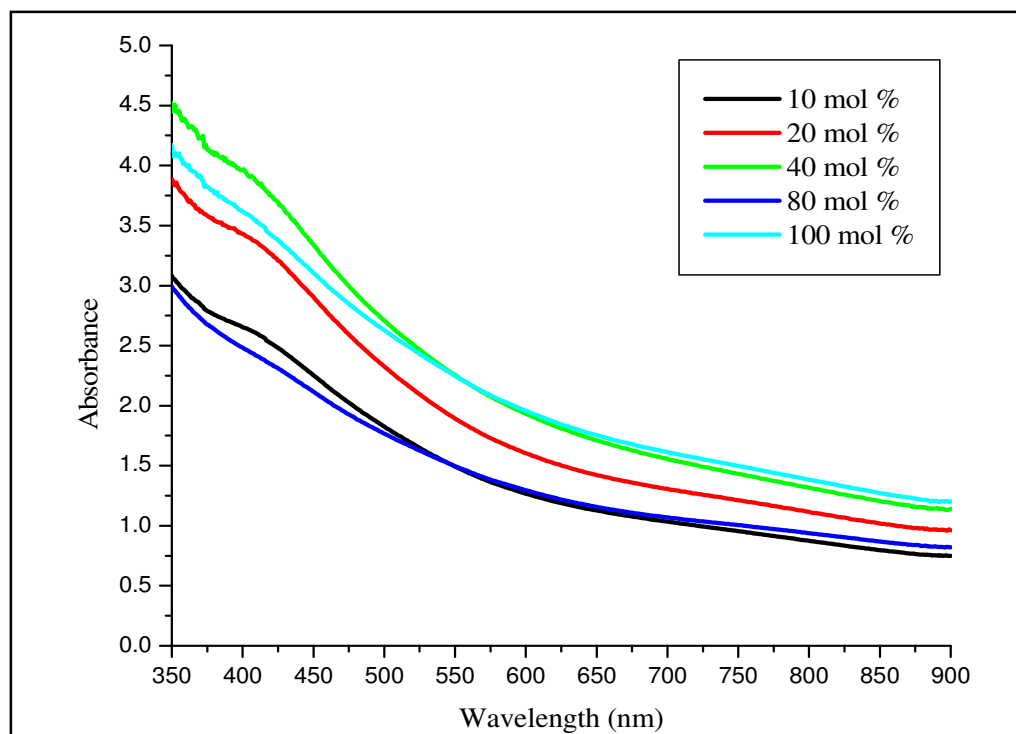
Figure 4.43: UV-Vis for 10, 20, 40, 80 and 100 mol% of Co-doped thin films.

Table 4.10: Band gaps corresponding to the various mol% of Co-doped thin films

Mol % of Co doping	Cross section thickness (nm)	Band gap (eV)		
10	373	1.64	2.07	2.30
20	430	1.68	2.04	2.32
40	424	1.58	1.93	2.26
80	444	1.64	1.98	2.30
100	485	1.58	2.00	2.23
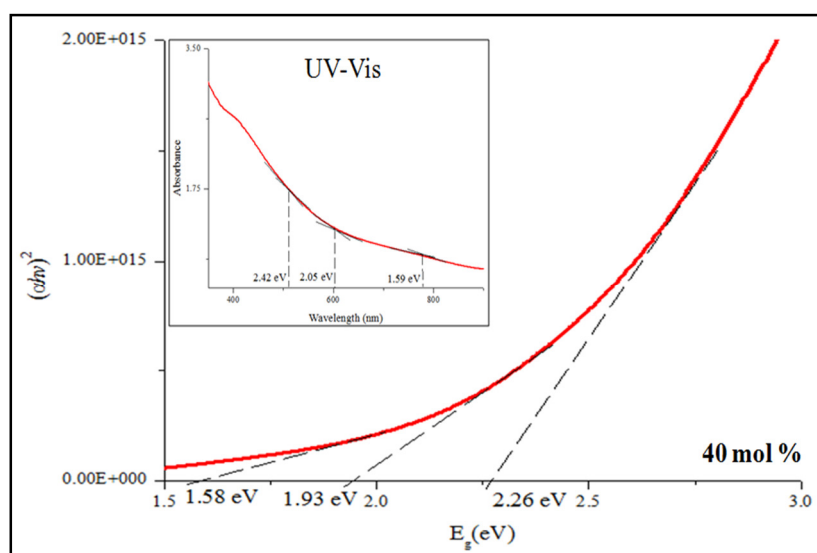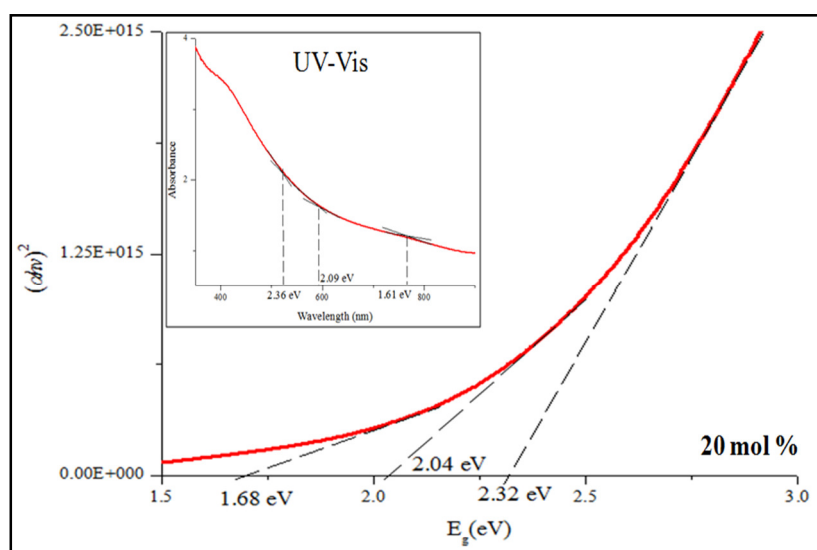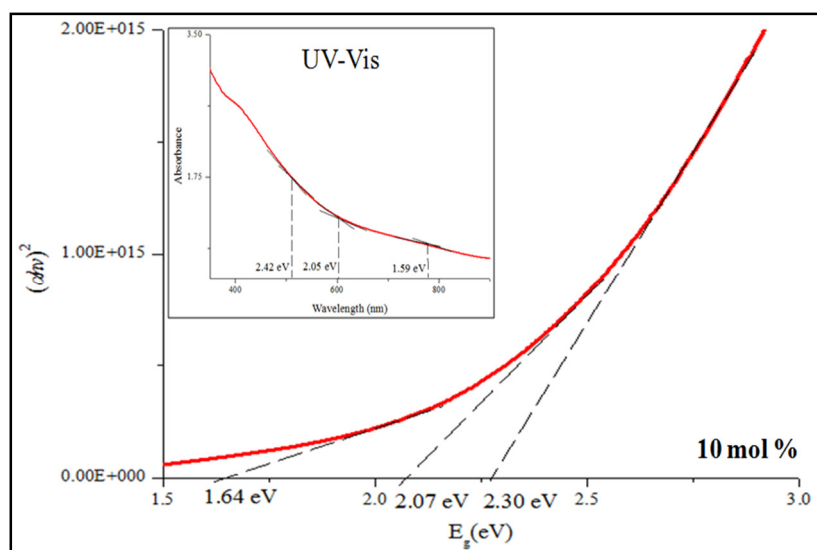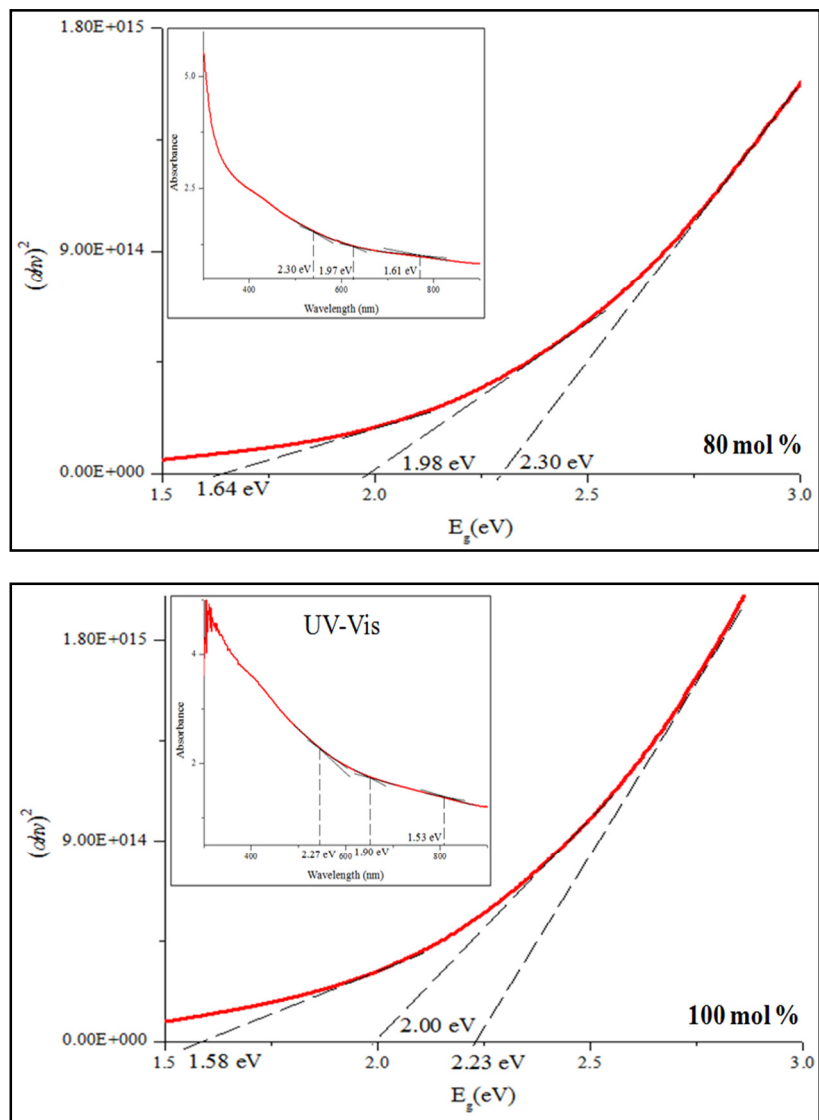
Figure 4.44: Tauc plot for 10, 20, 40, 80 and 100 mol % of Co-doped thin films and the inset UV-Vis graph to confirm the band gap of the respective thin films.

4.4.8 Photoelectrochemical (PEC) Water Splitting Studies

The J-V curve for Co-doped thin film can be observed in Figure 4.45. Generally, the current density in light condition is slightly higher than dark condition and there was a gradual increases of current density from the potential of -0.6 to 0.6 V under both light and dark conditions. In comparison with the Fe-doped thin films, the Co-doped thin films generally have a higher current density value. In dark condition, the photocurrent densities that were generated by 10, 20, 40, 80 and 100 mol% Co-doped thin films were recorded at 2.411, 2.049, 0.229, 2.005 and 2.073 mA/cm^2, respectively. In the lighted condition, the photocurrent densities generated were 2.497, 2.130, 0.238, 2.097 and 2.195 mA/cm^2, respectively. The 10 mol% Co-doped thin film showed the highest current density because it has highest electron mobility as compared to other thin films. The 10 mol% Co dopant gave the highest photocurrent density showed this is the optimal amount to be incorporated into the thin film. In contrast, for thin film with higher amount of Co dopant, the electron mobility decreases due to electron scattering causes by the ionized dopant atom and therefore the electron mobility became lower (Van Zeghbroeck, 2004). Similar observation also applied to 20, 80 and 100 mol% Co-doped thin film where the photocurrent density reached plateau value despite of increasing amount of Co dopant. It is noteworthy that the 40 mol% Co-doped thin film showed the unexpectedly lowest value of photocurrent density which could be due to the defect of the thin film. This thin film was expected to have similar value with the 20, 80 and 100 mol% where the photocurrent density

beyond 20 mol % Fe doping would be almost similar in value (plateau). The photocurrent density was tabulated in Table 4.11. The photosensitivity of the thin film can be estimated from the ratio of the photocurrent density in the light and dark conditions were tabulated in the Table 4.11.
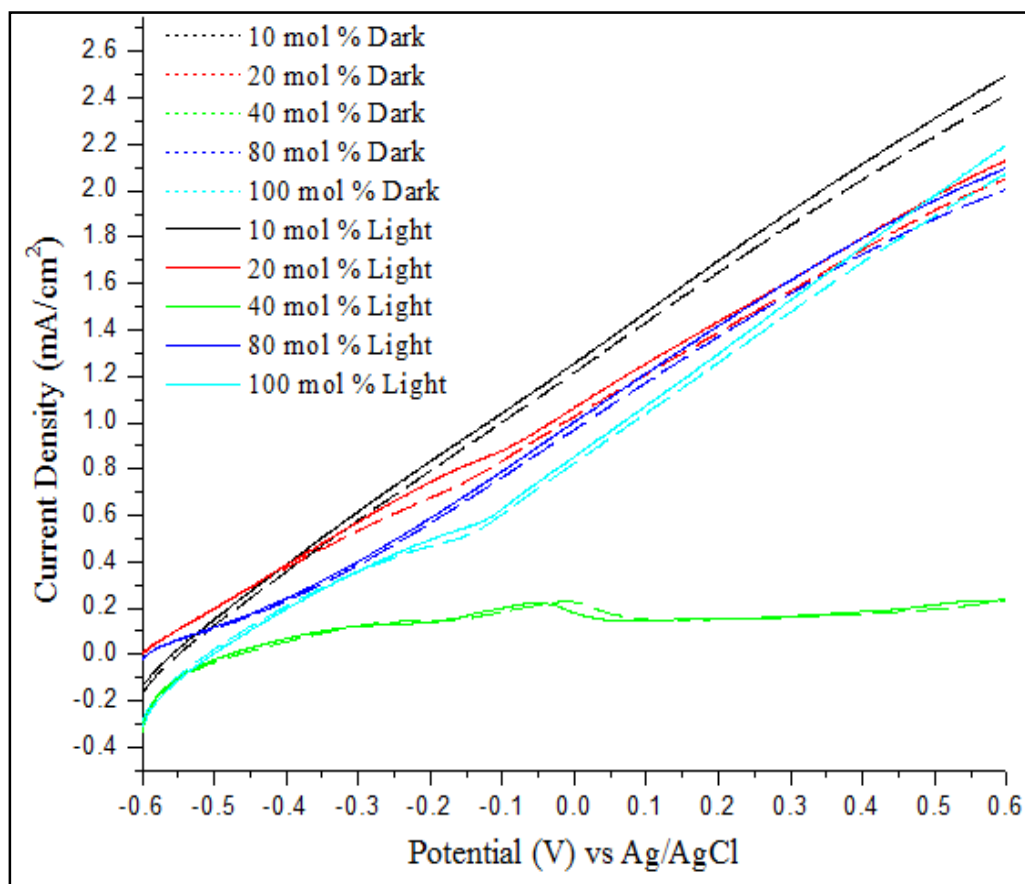
Figure 4.45: J-V curve for various mol% Co-doped thin films.

The Bode and Nyquist plot for both dark and light conditions were shown in Figure 4.46. It was observed that the 10 mol% Co-doped thin film has higher impedance (charge transport resistance) in comparison with the 80 and 100 mol%

Co-doped thin films even though it has the highest photocurrent density value in this Co-doped thin film series. This implies that the photocurrent density of 10 mol% Co-doped thin film was largely affected by the amount of Co dopant (at %) that was present in the thin film instead of the thin film impedance. As for the 20, 80 and 100 mol% Co-doped thin films, there was a difference in impedance despite having similar photocurrent density value. The 20 mol% Co-doped thin film was observed to have the highest resistance followed by the 80 and 100 mol% Co-doped thin films. According to Van Zeghbroeck, the sheet resistance, R_s, of a homogenous thin film with material resistivity, r, and thickness, t, is given by the formula of $R_s = \frac{r}{t}$ (Van Zeghbroeck, 2004). Therefore, the resistance for the 20, 80 and 100 mol % Co-doped thin film is inversely proportional to the film thickness.
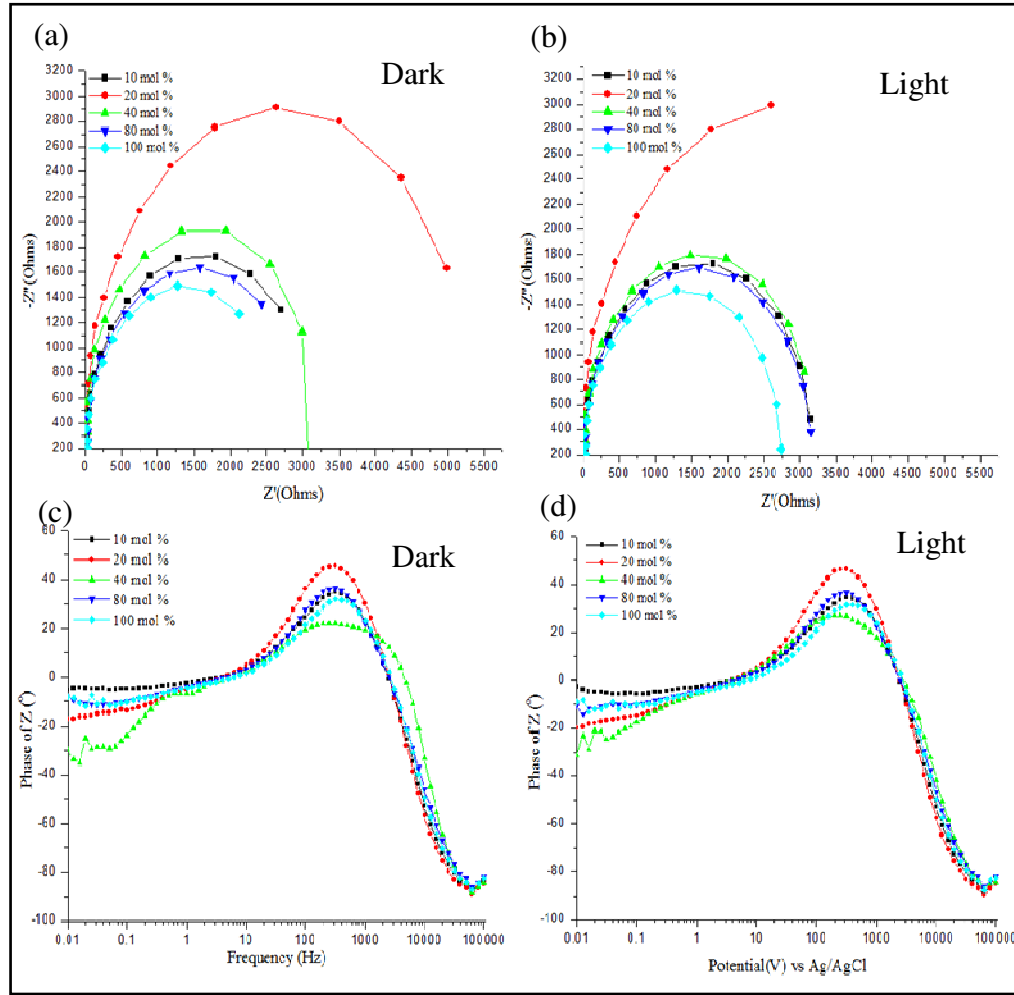
Figure 4.46: (a,b) Nyquist plots and (c,d) Bode plots for various mol% Co-doped thin films in different conditions (dark and light).

Table 4.11: Comparisons of PEC activities for various mol% Co-doped thin films

Mol %	J_D (mA/cm^2) At 1.23 V vs RHE	J_L (mA/cm^2) At 1.23 V vs RHE	Photo-sensitivity J_L/J_D At 1.23V vs RHE	Frequency Maxima Hz	Life time $\tau = 1/2\pi\upsilon$ (ms)
10	2.411	2.497	1.035	313.229	0.508
20	2.049	2.130	1.039	302.700	0.525
40	0.229	0.238	1.039	216.56	0.730
80	2.005	2.097	1.045	314.328	0.506
100	2.073	2.195	1.059	362.795	0.439

Similarly, the charge density for Co-doped thin films also had been calculated with Eq. 4.2 and the relative permittivity of the thin film was assumed to be 10. The slope value was obtained from the Mott-Schottky plot as shown in Figure 4.47. From the calculation, it was observed that the charge density for 10, 20, 40, 80 and 100 mol% Co-doped thin films were 1.4605×10^{21}, 5.2261×10^{20}, 1.0500×10^{20}, 1.4605×10^{21} and 5.2261×10^{20} cm^{-3}, respectively. The charge density values were tabulated in Table 4.12. It was significant that the 10 and 80 mol% Co-doped thin film had same and highest charge density value even though 10 mol% Co-doped thin film has the highest photocurrent density. We proposed that it was due to the 80 mol% having the smallest particle size in this thin film series at 20 nm while the 10 mol% has particle size of 120 nm (refer to Table 4.10). The particle size is reciprocal to the surface area at the interface of thin film and the surrounding electrolytes. Therefore, 80 mol% Co-doped thin film has the largest surface area at the interface which would cause the charge density to be the highest despite of the lower photocurrent density and large impedance when compared to the 10 mol% Co-doped thin film. The negative slope from the Mott-Schottky plot had indicated that the thin film is a p-type thin film (Lim et al., 2019)
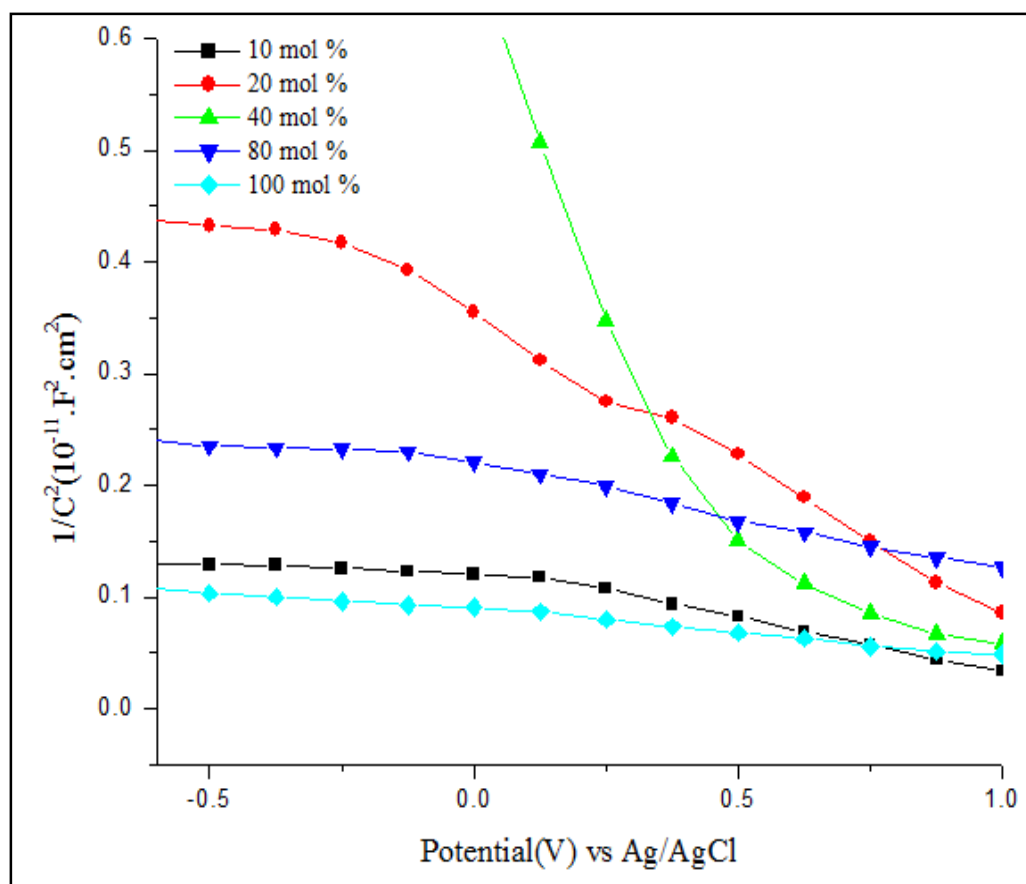
Figure 4.47: Mott-Schottky plot for Co-doped thin films.

Table 4.12: Charge densities for various mol% of Co-doped thin films

Percentage of Co doping (%)	Charge densities (cm^{-3})
10	1.4605×10^{21}
20	5.2261×10^{20}
40	1.0500×10^{20}
80	1.4605×10^{21}
100	5.2261×10^{20}

4.4.9   Mechanism of Electron Transfer Process for Co-series

The proposed z-scheme mechanism for Co-doped thin film is shown in Figure 4.48. The conduction and valence band potential for $Co(MoS_2)_2$ were determined as -0.12 and 1.46 eV, respectively. It was proposed that when the thin film was irradiated with light electron-holes separation occurs for all of the materials in the thin film. The electrons at the conduction band and holes at the valence bands flow from Mo_2S_3, $Co(MoS_2)_2$ and MoS_2. This creates the electron and holes trapping (electron hole trapping process) to suppress the electron-holes recombination and therefore increases the photocatalytic activity. Apart from that, the spectral absorption range and charge separation due to coupling of three different materials with different band gaps which also could increases the photocatalytical activity. While the holes act as the oxidizing agent to oxidized water, the electrons will eventually flow to the FTO substrate and then to platinum electrode (Pt) to reduce hydrogen ions.
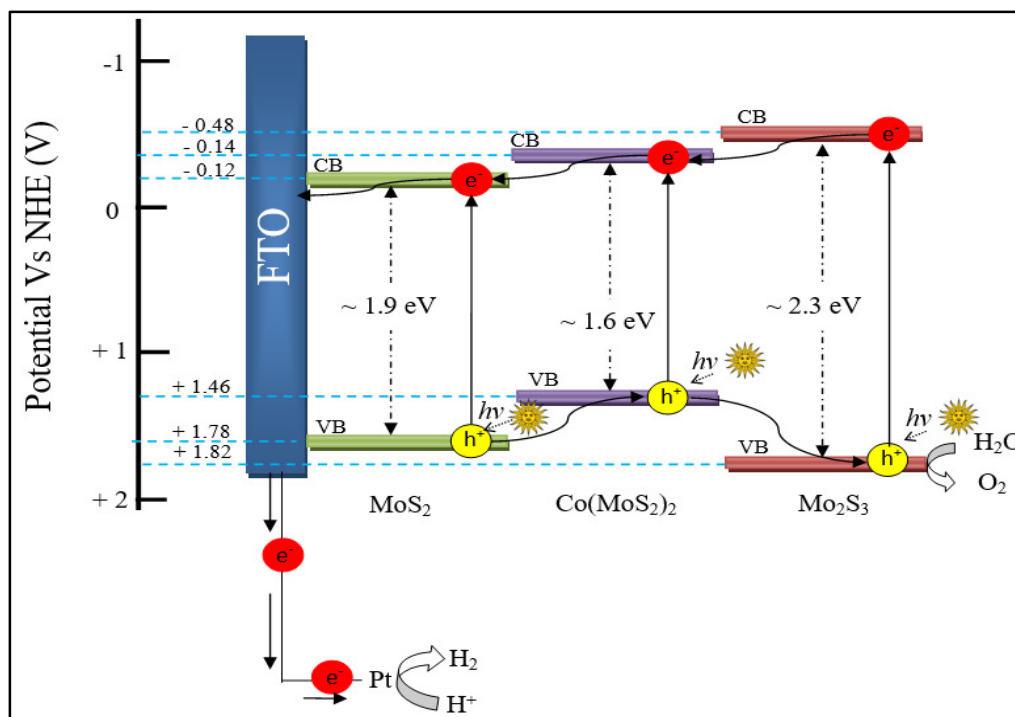
Figure 4.48: Proposed Z-scheme mechanism for Co-doped thin film.

4.5 Characterization of Thin Films Prepared from $[(\eta^5\text{-Cp})Mo(SMe)_2]_2$ (2) with Different Mol% of Nickelocene Cp_2Ni (Cp = cyclopentadiene)

The last element in the iron triads group would be the nickel (Ni) and this element was doped into the thin films to compare the Ni-doped thin film series properties in different mol % of doping. This series of thin film were analyzed with XRD, Raman spectroscopy, XPS, EDX, AFM, SEM, UV-Vis spectroscopy as well as photoelectrochemical (PEC) water splitting studies. Unlike Fe and Co series thin film it was observed that the Ni series thin films were undergo transition of morphology from granular to flakes morphology (will be explained in section 4.5.5 and 4.5.6). Generally, the PEC activity of this thin film series is

weaker than the Co-doped thin films series but stronger than the Fe-doped thin film series.

4.5.1   X-ray Diffraction Analysis (XRD)

Figure 4.49 shows the XRD pattern for Ni-doped thin film samples while the comparison of 10 mol% Ni-doped thin film, MoS_2/Mo_2S_3 and tetragonal SnO_2 (ICDD 01-077-052) is shown in Figure 4.50. In the Figure 4.49, other than the strong FTO background peaks, the weak XRD patterns of rhombohedral MoS_2 (ICDD 01-077-0341) and monoclinic Mo_2S_3 (ICDD 01-078-1332) were present in the XRD pattern for Ni-doped thin films. However, this time the $Ni(MoS_2)_2$ type structure was not detected but the rhombohedral Mo_3NiS_4 (ICDD 01-088-1802) were observed. The XRD pattern characteristic peaks for Mo_3NiS_4 were observed at 15.55°, 17.11°, 26.58°, 34.01°, 51.56°, 54.84°, 61.65° and 65.53° which corresponded to (101), (110), (003), (21-2), (32-2), (006), (23-4) and (51-2), respectively. $M(MoS_2)_2$ type structure was not formed in Ni series which could be due to nickel which gave a different growth promotional effect as can be seen in SEM and AFM image where Fe and Co doping gave granular morphology while Ni doping gave flakes-like morphology. The XRD characteristic peaks list for the Ni-doped thin film are tabulated in Table 4.13. The films do not show the presence of Ni species such as NiS_2 which implies that the Ni is accommodated in the MoNiS phase.
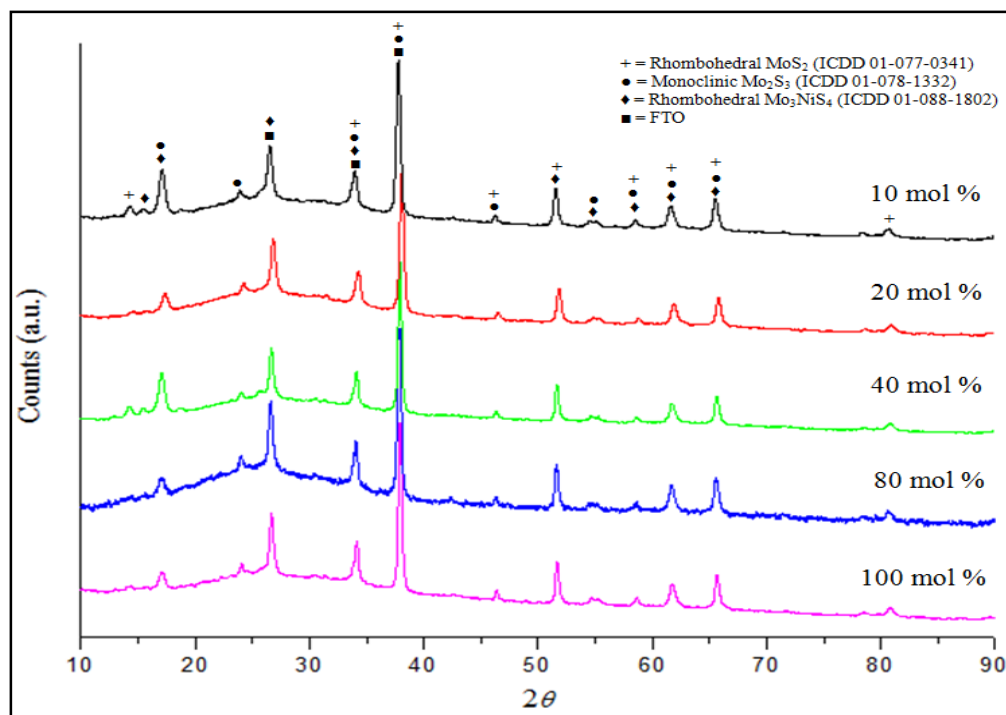
Figure 4.49: XRD diffraction pattern for 10, 20, 40, 80 and 100 mol% of Ni-doped thin films.

Table 4.13: XRD characteristic peak list for Ni-doped thin film

2θ	Assigned Peak
14.28	MoS_2
15.55	Mo_3NiS_4
17.11	Mo_2S_3/ Mo_3NiS_4
23.91	Mo_2S_3
26.62	Mo_3NiS_4/ FTO
33.96	MoS_2 / Mo_2S_3 / Mo_3NiS_4/ FTO
37.78	MoS_2 / Mo_2S_3/ Mo_3NiS_4/ FTO
46.24	Mo_2S_3/ Mo_3NiS_4
51.53	MoS_2/ Mo_2S_3/ Mo_3NiS_4
55.19	Mo_2S_3/ Mo_3NiS_4
58.53	MoS_2/ Mo_2S_3/ Mo_3NiS_4
61.60	MoS_2/ Mo_2S_3/ Mo_3NiS_4
65.51	MoS_2/ Mo_2S_3/ Mo_3NiS_4
80.70	MoS_2
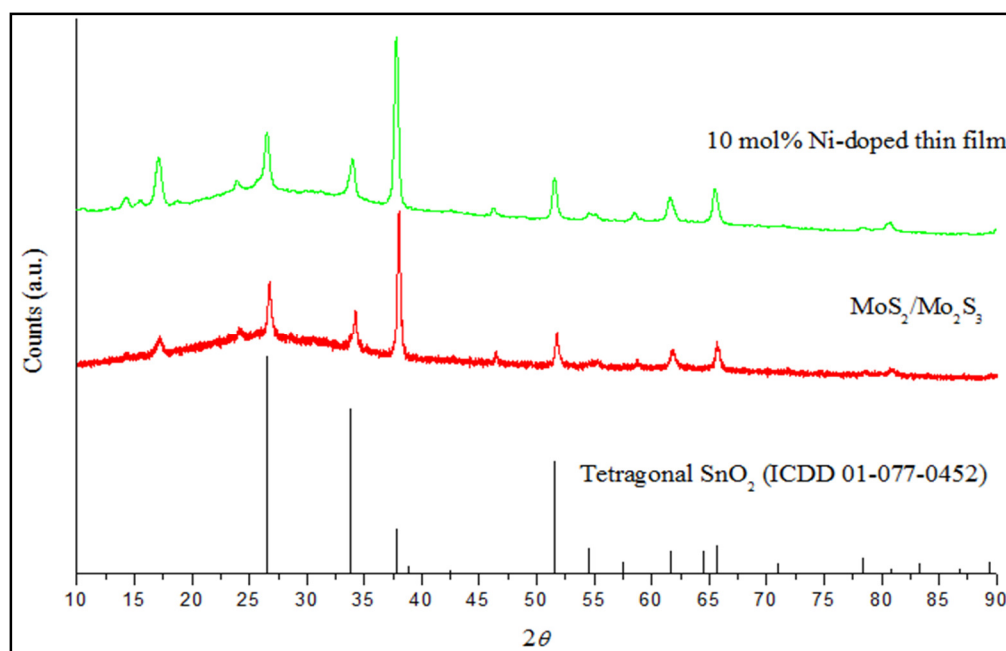
Figure 4.50: Comparison of 10 mol% Ni-doped thin film, MoS_2/Mo_2S_3 and tetragonal SnO_2 (ICDD 01-077-052).

4.5.2 Raman Spectroscopy

As for 80 mol% Ni-doped thin film shown in Figure 4.51, it was observed that the film had a similar result with the Fe- and Co-doped thin films. The peak values at 377.97 and 400.34 cm^{-1} are corresponded to the typical E^1_{2g} and A_{1g} of MoS_2. The difference between E^1_{2g} and A_{1g} of MoS_2 in 22.37 cm^{-1} indicating the MoS_2 was in bilayer form after compared to the literatures value (Lim et al., 2019; Li et al., 2012). Moreover, the broad peaks of MoS_2 indicated the present of Mo_2S_3 was overlapped with MoS_2. On the other hand, the peaks at 339.50 and 448.06 cm^{-1} showed the presence of $Mo-S_2$ bridging in the thin film. The peak recorded at 347.53 cm^{-1} is attributed to the $Ni-S_2$ bridging. From the above

138

mentioned observations, we concluded that Ni was successfully doped into MoS_2/Mo_2S_3 thin films.
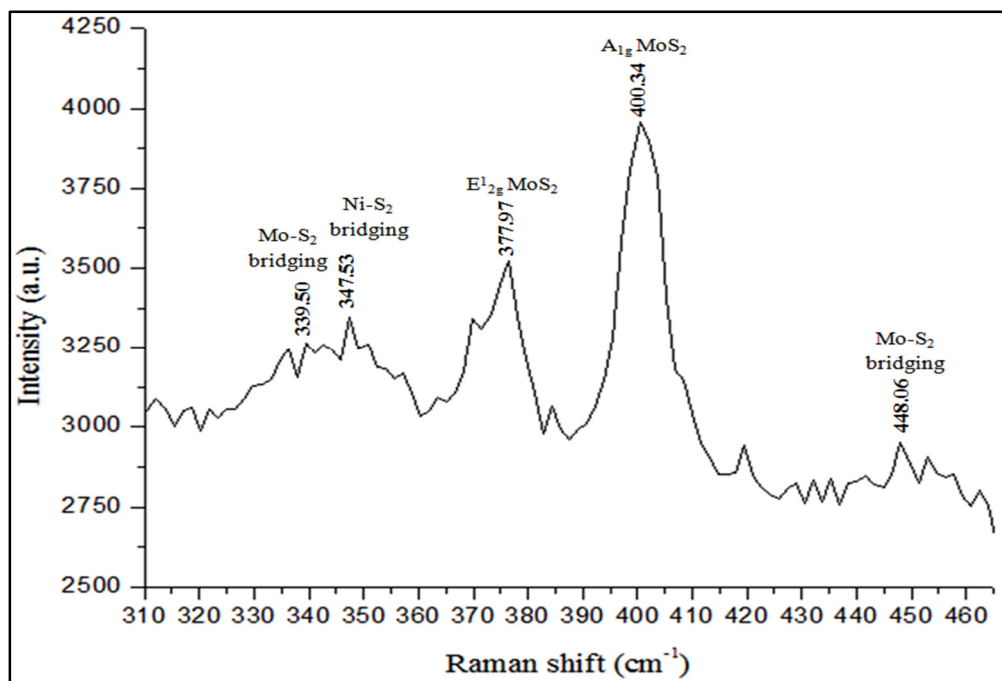
Figure 4.51: Raman spectroscopy of 80 mol % Ni-doped thin film.

It was noted that the Raman spectrum for Fe, Co and Ni doped thin films are almost identical for different types of bonding mode. We proposed this observation is due to similar atomic radii of Fe, Co and Ni, allowed them also sharing the similar chemical and physical properties. However, the value between E^1_{2g} and A_{1g} of MoS_2 for Fe, Co and Ni doped thin films are not identical where Fe, Co and Ni-doped thin film gave the difference of 19.17 cm^{-1} (monolayer), 25.27 cm^{-1} (quadrilayer) and 22.37 cm^{-1} (bilayer), respectively. It was also worth

noting that these difference values are higher when compared to the literatures values by ~1.17 cm^{-1}. We suggest this could be due to the fact that the metal doping had affected the stacking of MoS_2 layer whereas the literatures values are based on the pure MoS_2.

4.5.3 X-ray Photoelectron Spectroscopy (XPS) Analysis

Both the 10 and 100 mol% Ni-doped thin film were represented in Figure 4.52. These thin films shared the same XPS spectrums indicating that all thin films in the Ni-doped series are the same despite of different at % that was present in the thin film, this observation will be discussed in section 4.4.4. The peaks that were observed at the binding energies of 855.84 and 879.37 eV were corresponded to the Ni^{3+} $2p_{3/2}$ and Ni^{3+} $2p_{1/2}$. As for the divalent nickel, the Ni^{2+} $2p_{3/2}$ and Ni^{2+} $2p_{1/2}$ is at the binding energies of 852.44 and 870.28 eV respectively (Kong et al., 2018). The NiMoS binding energy as shown in Figure 4.52 (a) was at binding energies of 853.50 and 873.63 eV (Sizova and Maksimov, 2016). Figure 4.52 (b) showed a similar pattern with Fe- and Co-doped thin film XPS spectrums where Mo^{4+} and Mo^{3+} were present in the thin film. The peaks at the binding energy of 228.83 and 231.84 eV were assigned to Mo^{4+} $3d_{5/2}$ and Mo^{4+} $3d_{3/2}$ respectively. The Mo^{3+} $3d_{5/2}$ and Mo^{3+} $3d_{3/2}$ were assigned to 233.30 and 231.84 eV, respectively. As for S^{2-} $2p_{3/2}$ and S^{2-} $2p_{1/2}$, as shown in Figure 4.52

(c), they were assigned to the peaks with binding energy of 161.72 and 162.73 eV, respectively.
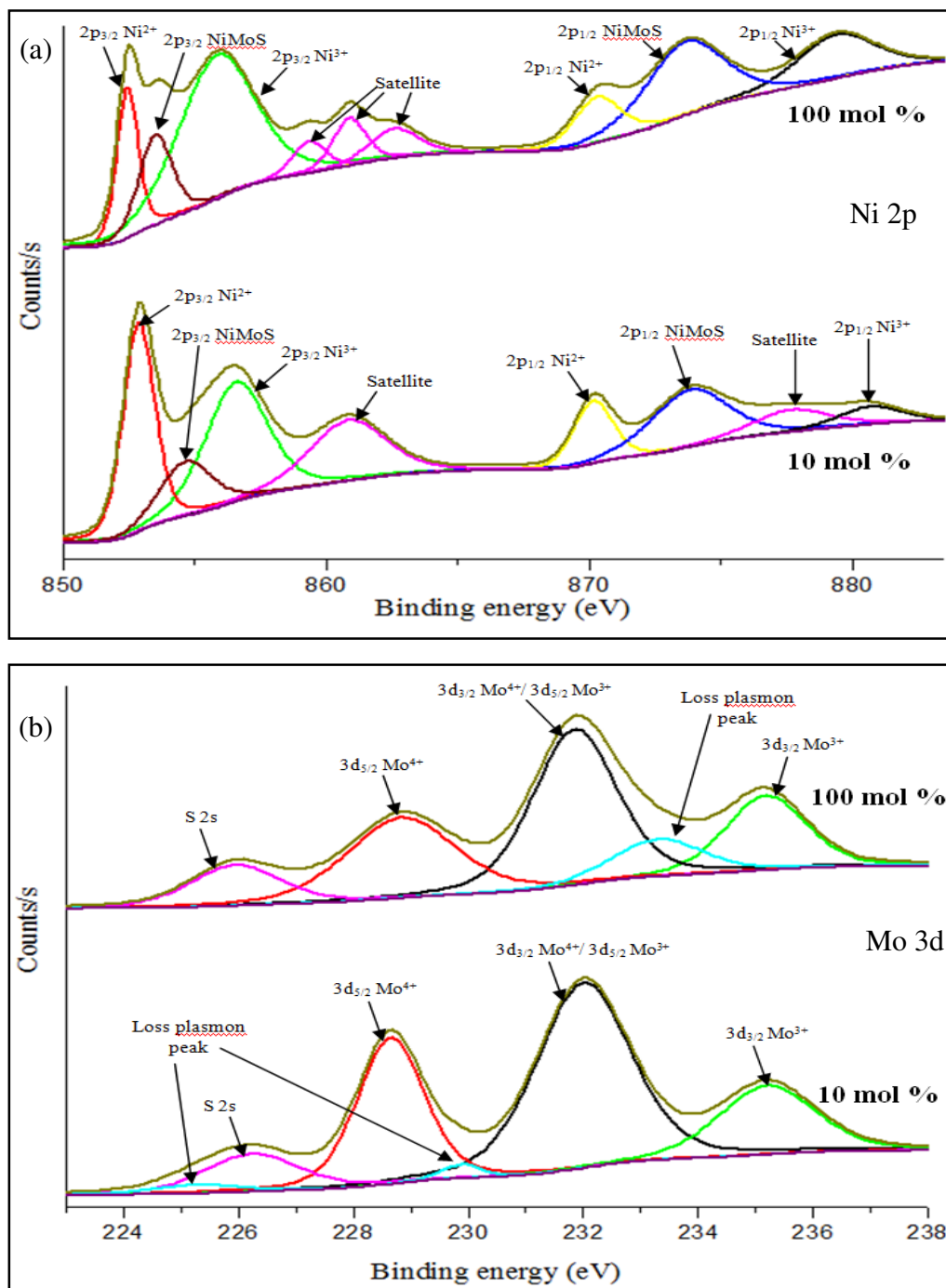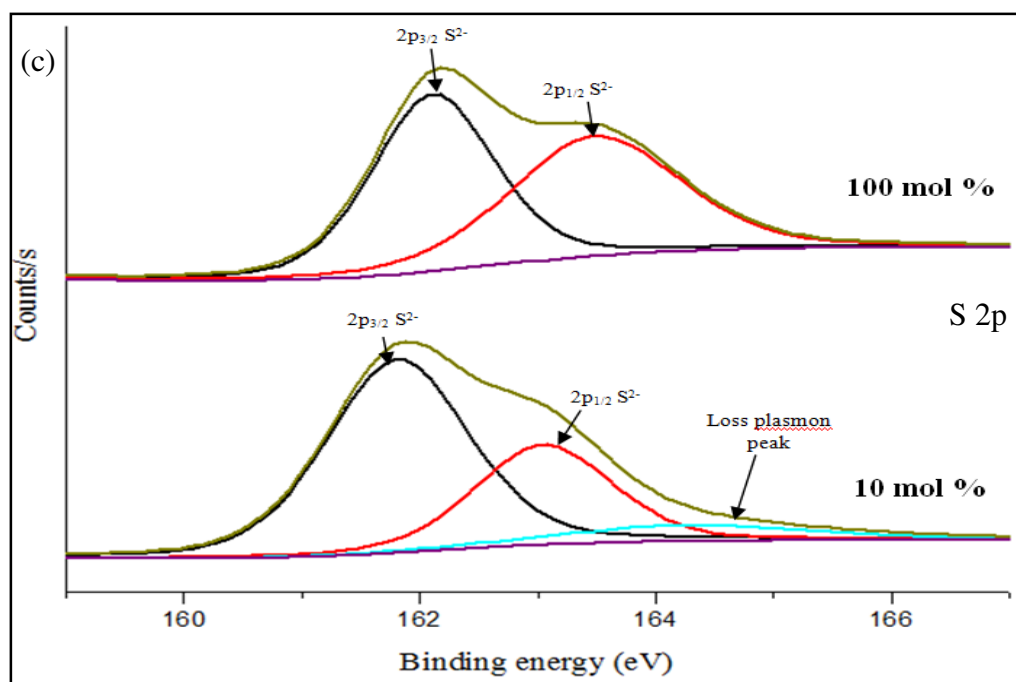
Figure 4.52: XPS spectrum for (a) Ni 2p, (b) Mo 3d and (c) S 2p for 80 mol% Ni-doped thin film

There are slight differences for the XPS spectrum S 2p of all of the thin films as the Co- and Ni-doped thin films does not show the S^{2-} corresponded to the Mo_2S_3. This could be due to the machine limitation as the analysis was based on the surface where the sampling depth was in between 3-10 nm. Moreover, the roughness and surface morphology could also affect the XPS analysis.

4.5.4 Energy Dispersive X-ray (EDX) Spectroscopy and Elemental Mapping Analysis

From the EDX spectroscopy, it was observed that the atomic percentage (at %) of Ni in Ni-doped thin film is proportional to the mol% of nickelocene in the feed. Increasing of the feed also increases the Ni at% for 10, 20, 40, 80 and 100 mol% Ni-doped thin films, where 0.91, 2.71, 4.67, 6.31 and 6.69 at % were detected, respectively. Despite of having different at% of Ni dopants that were present in the thin films in the Ni-doped thin films series, it was observed that the element Ni, Mo and S are distributed homogenously for all thin films based on the elemental mapping analyses. The at % for Ni-doped thin films were shown in Table 4.14 whereas Figures 4.53 and 4.54 showed the EDX graph and elemental mapping, respectively.

Table 4.14: EDX result for various mol% Ni-doped thin films

Mol % of Ni-doped thin film	Elements	Atomic % (at %)
10	Mo	38.35
	Ni	0.91
	S	60.74
20	Mo	38.12
	Ni	2.71
	S	59.17
40	Mo	37.32
	Ni	4.67
	S	58.01
80	Mo	35.43
	Ni	6.31
	S	58.26
100	Mo	36.59
	Ni	6.69
	S	56.72
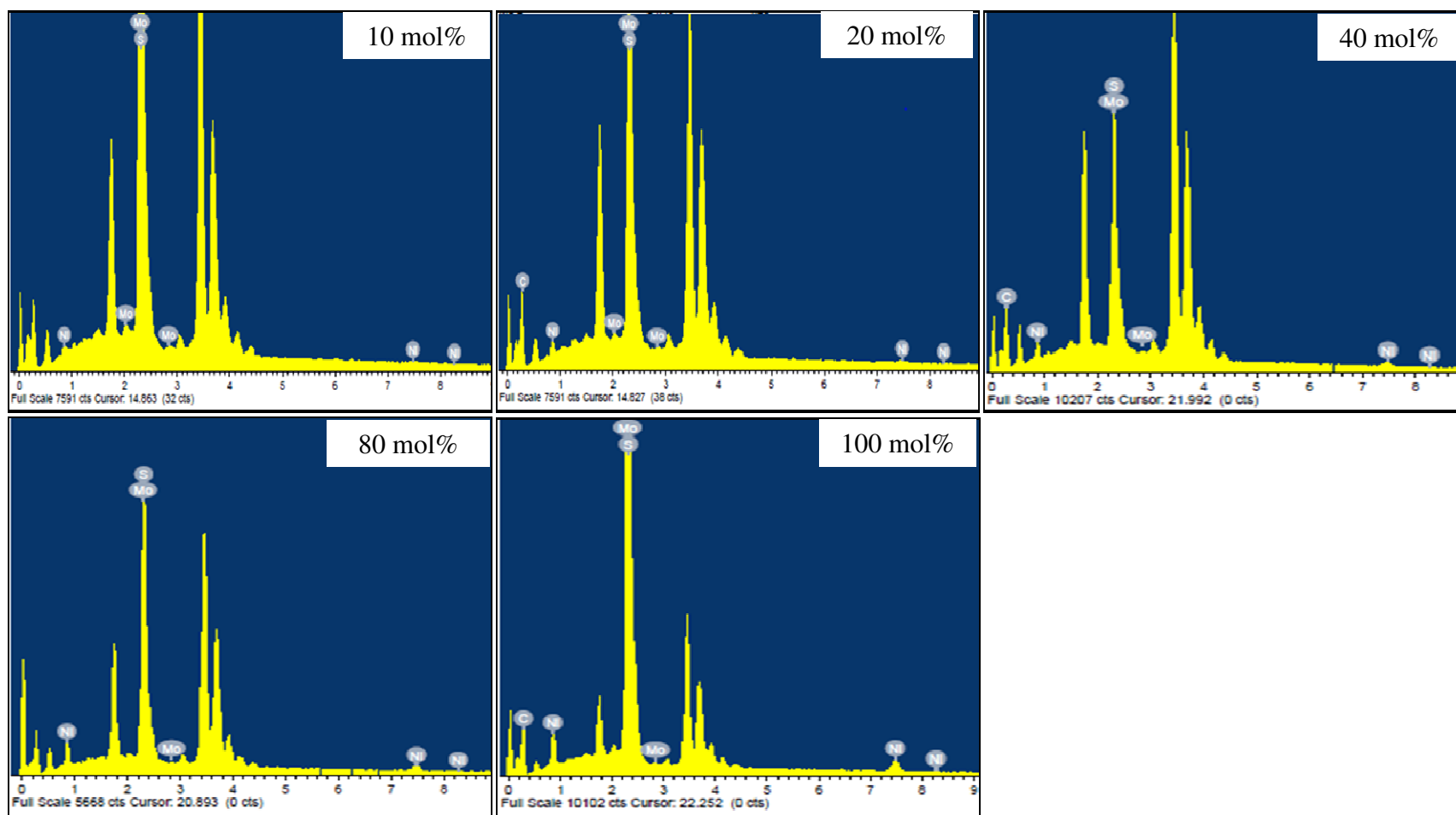
Figure 4.53: EDX spectrum for various mol% Ni-doped thin films.

10 mol % Ni-doped thin film
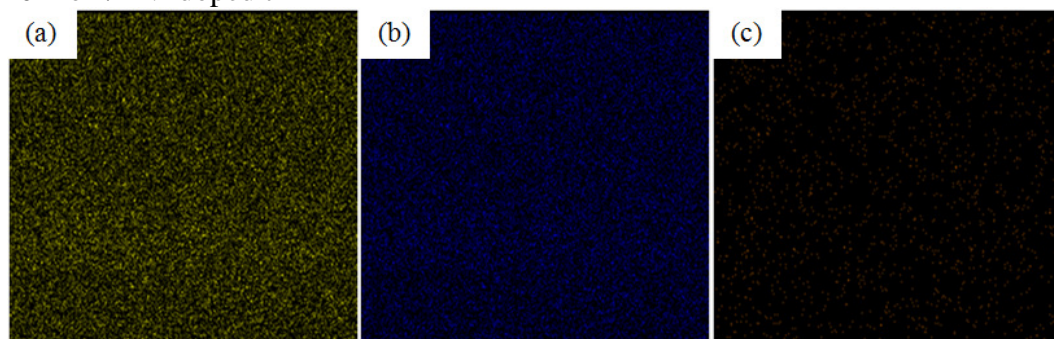
20 mol % Ni-doped thin film
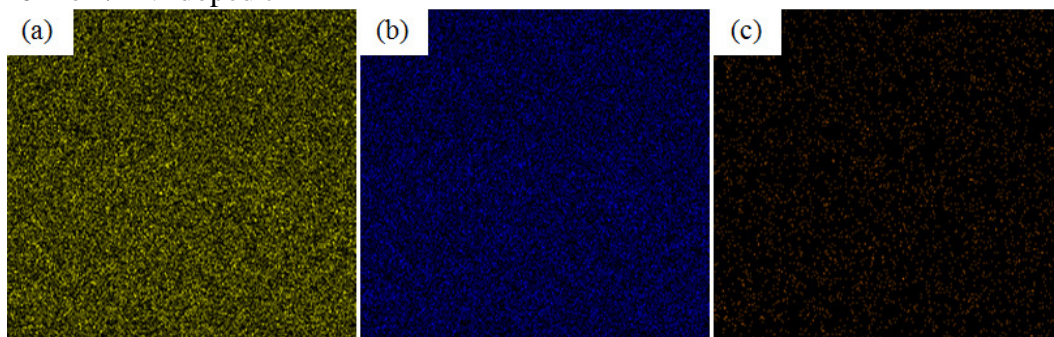
40 mol % Ni-doped thin film
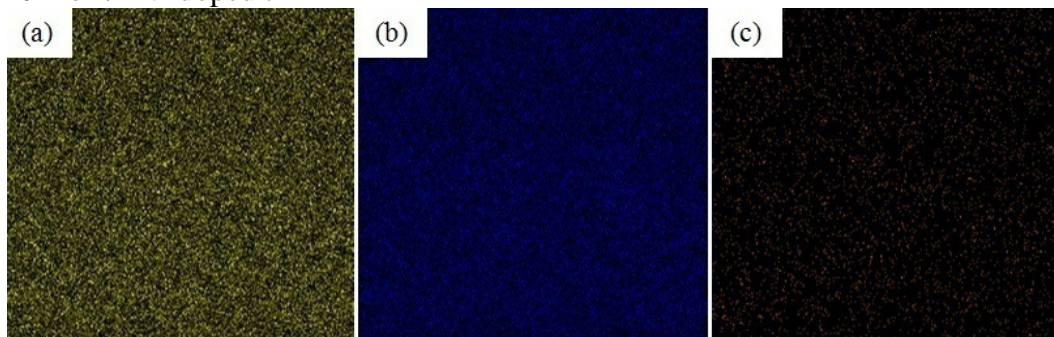
80 mol % Ni-doped thin film
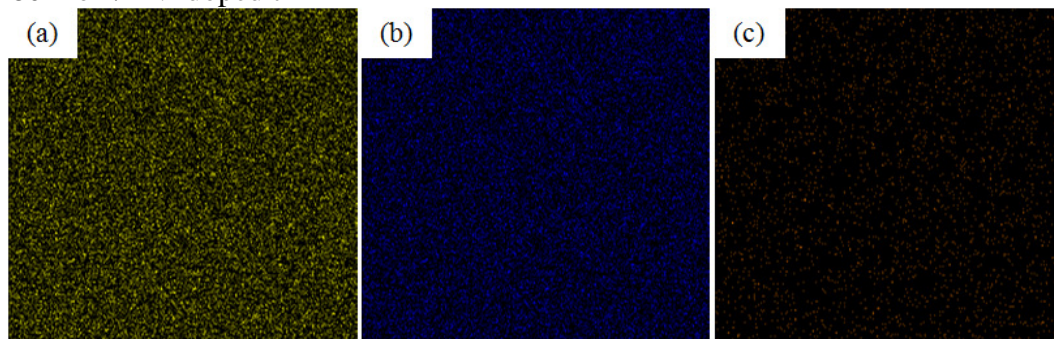
100 mol % Ni-doped thin film
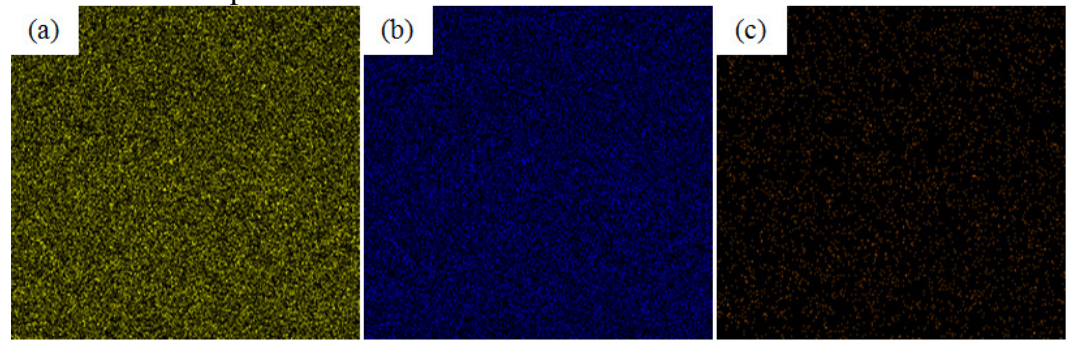
Figure 4.54: EDX graph for Ni-doped thin film (a) sulfur, (b) molybdenum and (c) nickel.

4.5.5 Atomic Force Microscopy (AFM) Analysis

Doping of Ni into the thin films had resulted from granular surface morphology into flake like surface morphology starting with 40 mol% Ni-doped thin film. Apart from that, the Ni-doped thin films are rougher compared to the Fe- and Co-doped thin films. Table 4.15 showed the Ra, Rq, Rpv, Rv and Rp for Ni-doped thin films while Figures 4.55 and 4.56 showed the 2D AFM images and line profile for different mol% Ni-doped thin films. The 3D AFM images can be observed in Figure 4.57. It can be observed that the 100 mol% Ni-doped thin film had the highest roughness as compared to other mol% of Ni-doped thin films indicating that it may easily corrode as compared to other thin films that have lower roughness. This could be due to the different growth promotional effect of Ni when compare to Fe and Co.

10 mol %

20 mol %

40 mol %

80 mol %
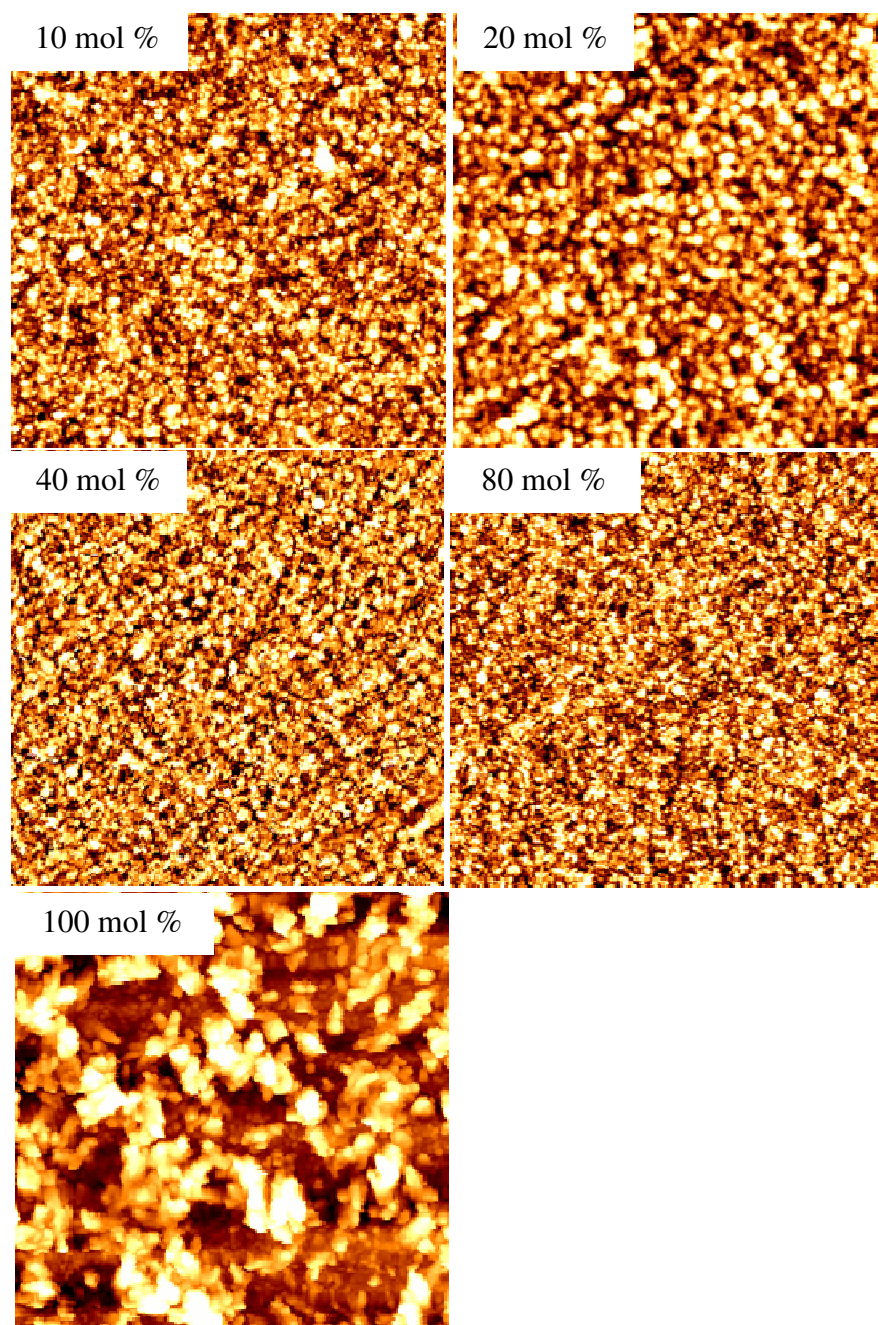
100 mol %

Figure 4.55: AFM 2D images for 10, 20, 40, 80 and 100 mol % of Ni-doped thin films.
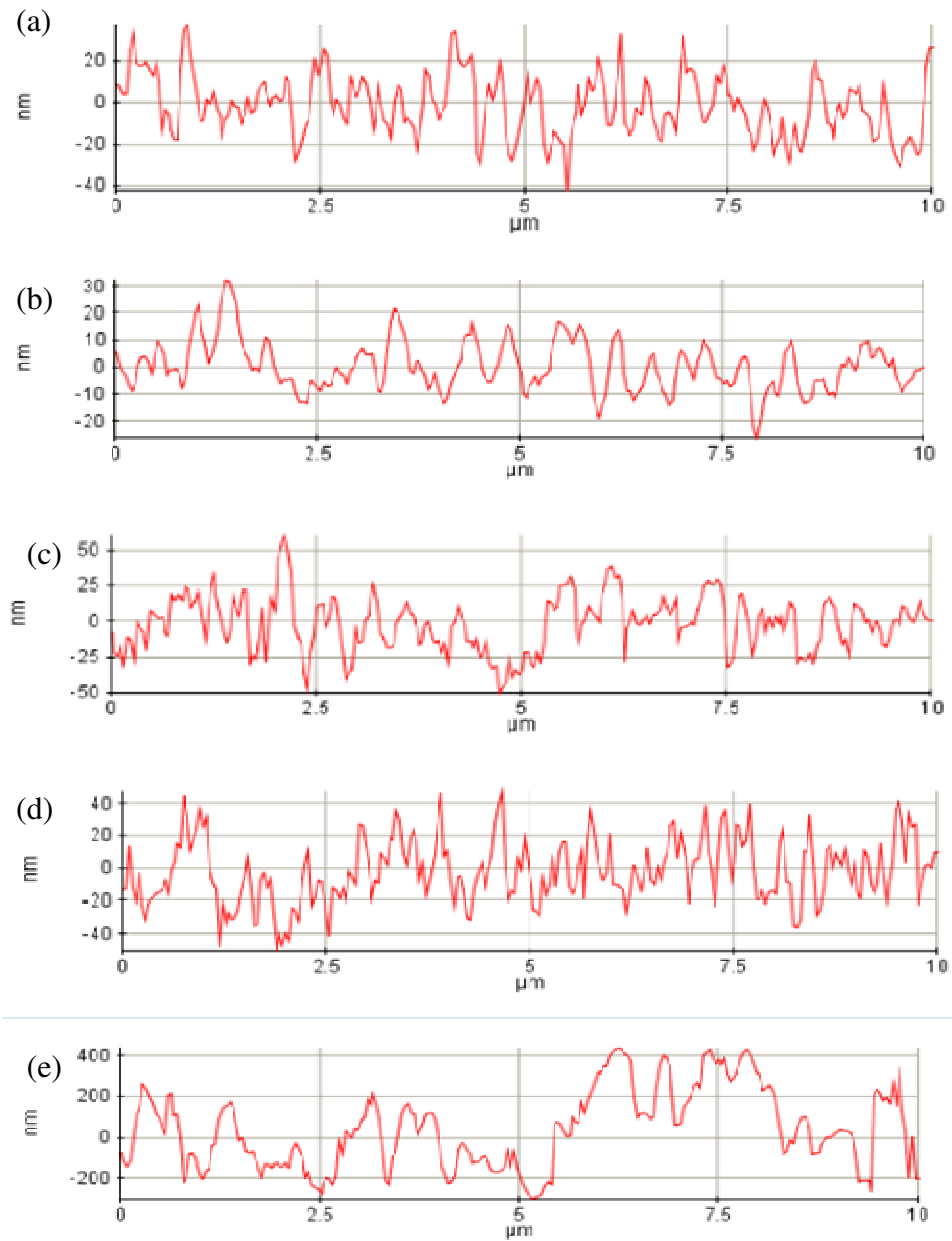
Figure 4.56: Line profile for (a) 10, (b) 20, (c) 40, (d) 80 and (e) 100 mol% of Ni-doped thin films.
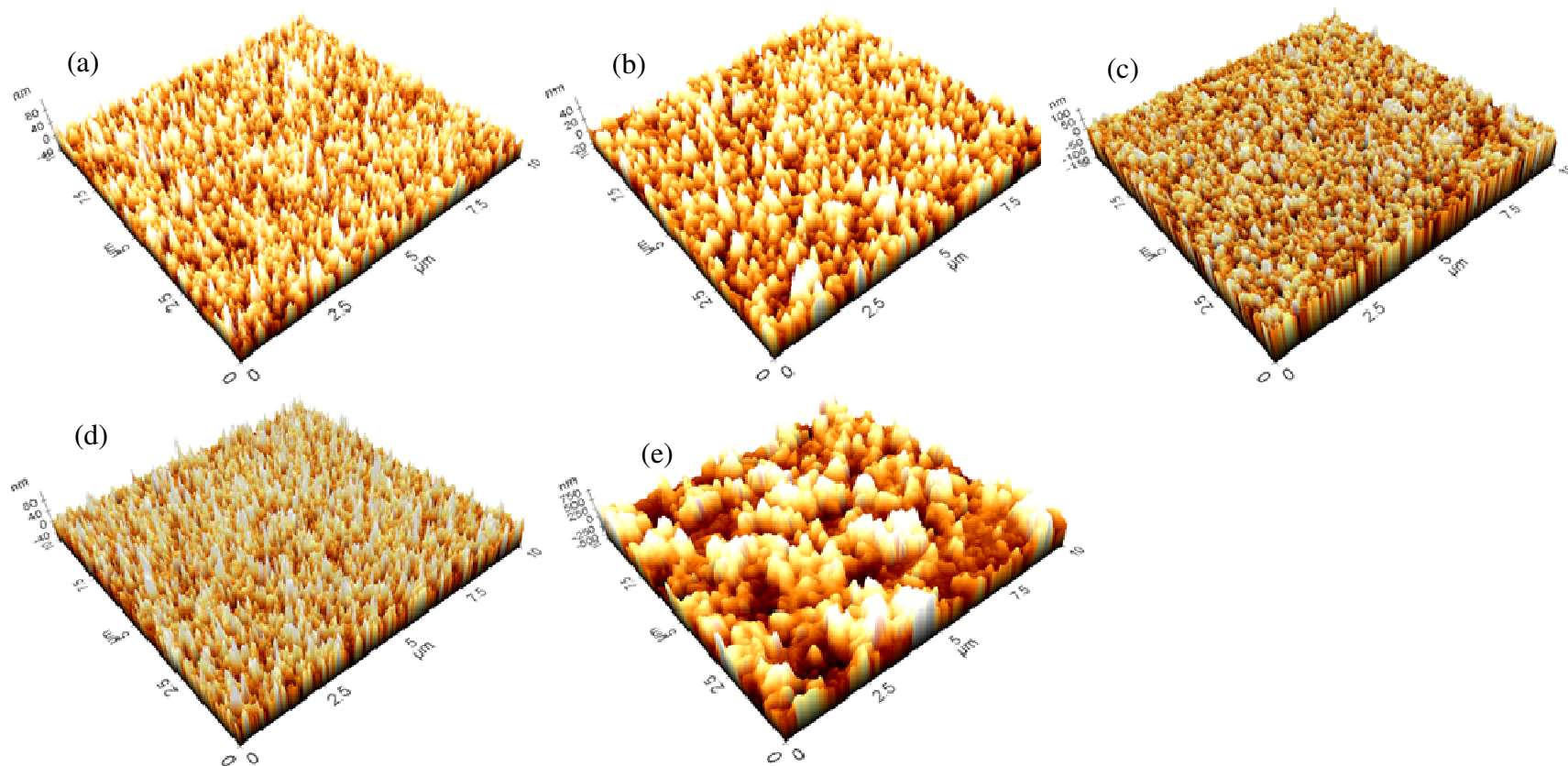
Figure 4.57: AFM 3D images for (a, b) 10 (c, d) 20, (e, f) 40 (g, h) 80 and (i, j) 100 mol% of Ni-doped thin films.

Table 4.15: Ra, Rq, Rpv, Rv and Rp for various mol% of Ni-doped thin films

Mol %	Statistics	Value (nm)
10	Roughness average, Ra, (nm)	11.780
	Root mean square, Rq, (nm)	14.466
	Maximum profile height, Rpv, (nm)	78.905
	Maximum valley depth, Rv, (nm)	42.303
	Maximum peak height, Rp, (nm)	36.602
20	Roughness average, Ra, (nm)	7.439
	Root mean square, Rq, (nm)	9.419
	Maximum profile height, Rpv, (nm)	58.584
	Maximum valley depth, Rv, (nm)	26.362
	Maximum peak height, Rp, (nm)	32.223
40	Roughness average, Ra, (nm)	15.275
	Root mean square, Rq, (nm)	19.252
	Maximum profile height, Rpv, (nm)	110.020
	Maximum valley depth, Rv, (nm)	50.185
	Maximum peak height, Rp, (nm)	59.836
80	Roughness average, Ra, (nm)	15.950
	Root mean square, Rq, (nm)	19.706
	Maximum profile height, Rpv, (nm)	98.440
	Maximum valley depth, Rv, (nm)	50.899
	Maximum peak heaigh, Rp, (nm)	47.541
100	Roughness average, Ra, (nm)	162.299
	Root mean square, Rq, (nm)	194.353
	Maximum profile height, Rpv, (nm)	747.301
	Maximum valley depth, Rv, (nm)	310.437
	Maximum peak height, Rp, (nm)	436.864

4.5.6 Scanning Electron Microscopy (SEM) Analysis

Figures 4.58 – 4.62 had depicted that the morphology tends to be flakes-like. As the mol% of Ni dopant was increased as the, Ni mol% increases together with the particle size. From Figure 4.58, 10 mol% Ni-doped thin film has a granular morphology. When the mol% was increased to 20 mol%, the morphology changes to rod-like. When the doping is increased to 40 mol%, it gave a flake-like morphology. The particle size of flakes increases at 80 mol% (refer to the histogram in Figure 4.63). Specifically, the majority of the particle sizes for 10, 20, 40, 80 and 100 mol% of Ni-doped thin films were 80, 120, 120, 120 and 800 nm, respectively. The growth promotional effect of Ni in thin films was explained in terms of a model originally proposed by Salitra and co-workers (Salitra et al., 1993) known as Van der Waals rheotaxy (vdWR) (Galun et al., 1995; Tenne et al., 1996). As for thin film thickness, competition between the attractive Van der Waals force, repulsive steric force and electric-double-layer force caused the equilibrium film thickness (Clarke, 1989; Tanaka et al., 1994). The thin nickel layer at the interface becomes slowly sulfurized and forms a liquid film when the sulfur concentration is close to the eutectic point, which is at 645 ^{o}C. The crystallization and c orientation of the films are enhanced by crystal growth on a liquid NiS_x interfacial films, function as a rheotaxy process flux mediums (Regula et al., 1997).
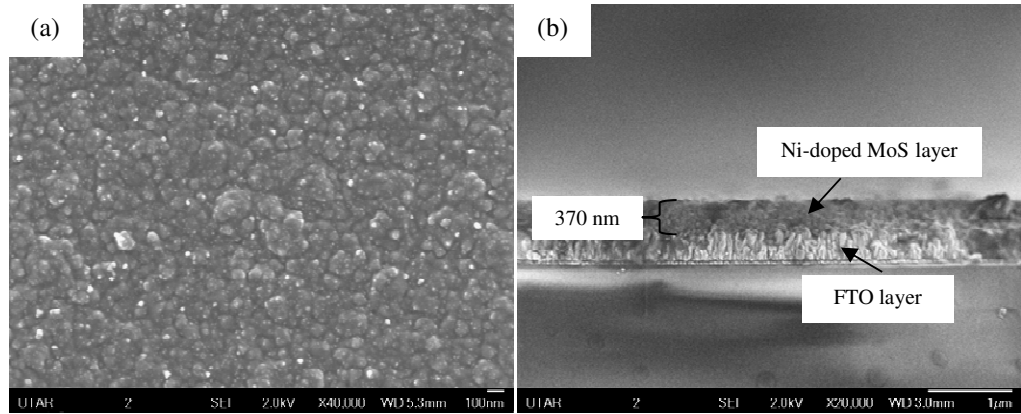
Figure 4.58: SEM images for 10 mol% Ni-doped thin film for (a) surface morphology and (b) cross section thickness.
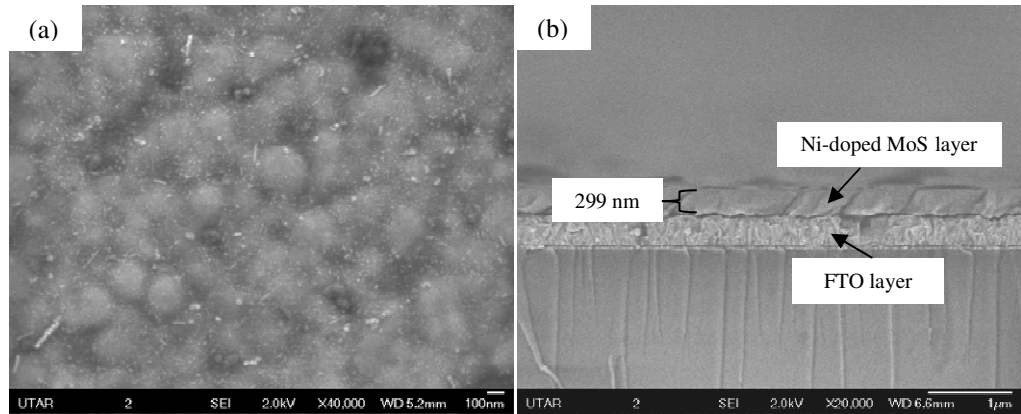
Figure 4.59: SEM images for 20 mol% Ni-doped thin film for (a) surface morphology and (b) cross section thickness.
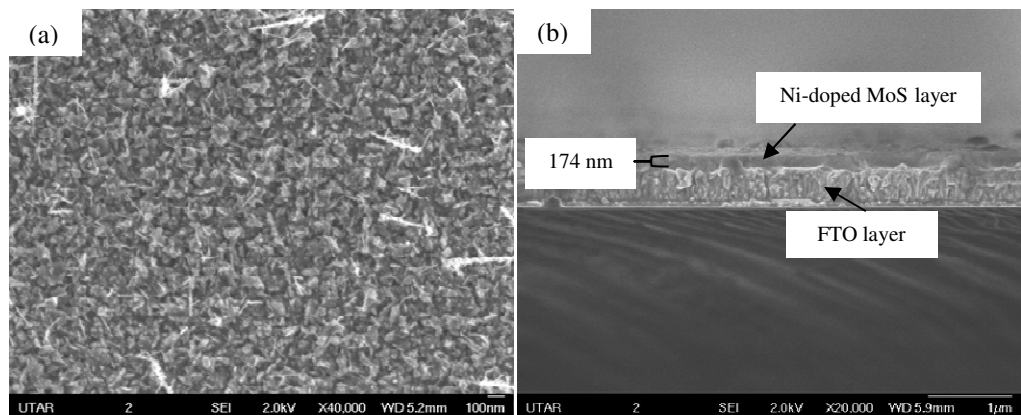
Figure 4.60: SEM images for 40 mol% Ni-doped thin film for (a) surface morphology and (b) cross section thickness.
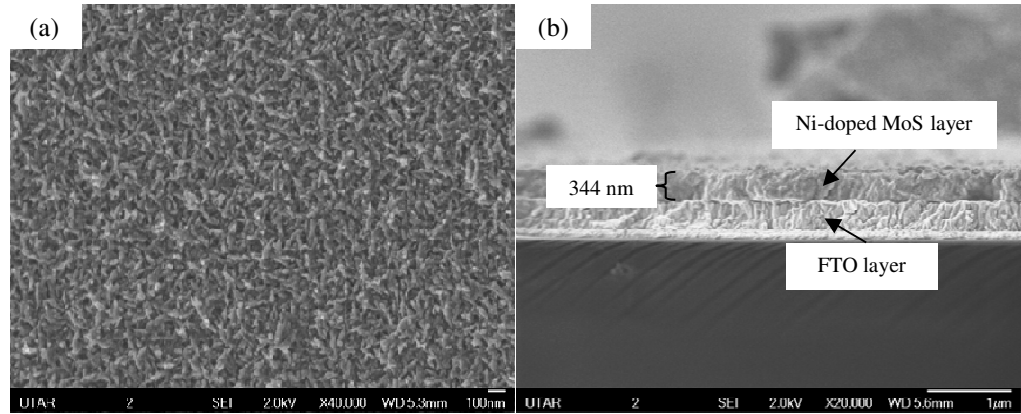
Figure 4.61: SEM images for 80 mol% Ni-doped thin film for (a) surface morphology and (b) cross section thickness.
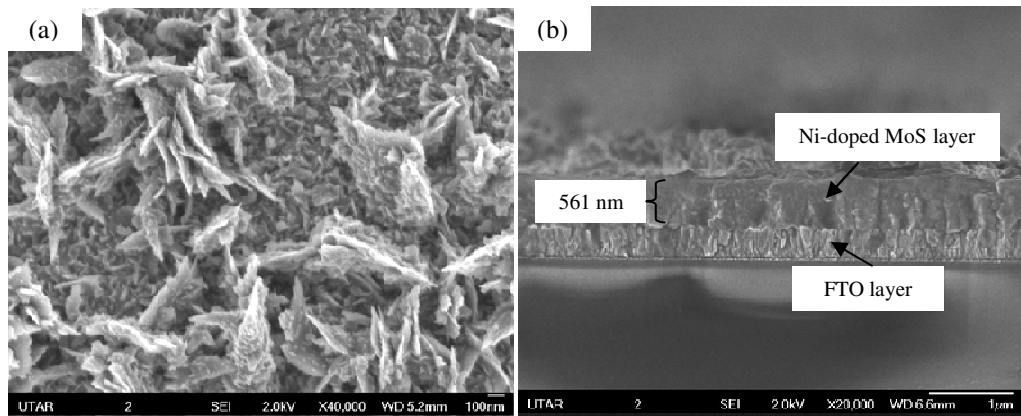
Figure 4.62: SEM images for 100 mol% Ni-doped thin film for (a) surface morphology and (b) cross section thickness.
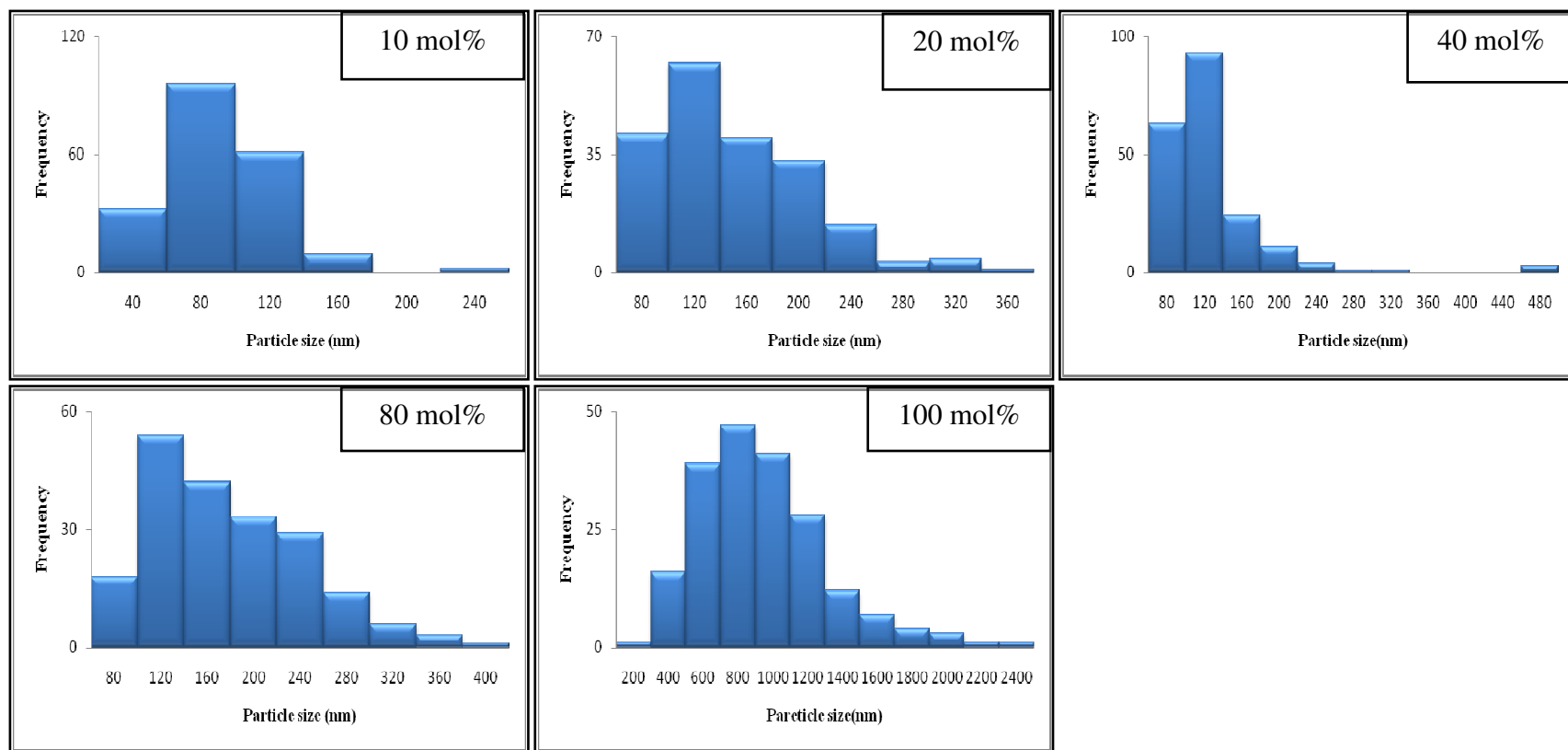
Figure 4.63: Histogram for various mol% Ni-doped thin films.

The SEM images for all thin films are in agreement with the findings for AFM. The dual source precursor approach gives a possibility to dope transition metal into MoS_2/Mo_2S_3 thin films leading to morphological and crystallographic changes which may improves the mechanical properties (Tedstone et al., 2014) as well as improves the photocatalytic activity of the thin films (Kudo and Miseki, 2009). Photocatalyst with different morphologies generally can affect the photocatalytic performance due to the active sites, active facets, associated adsorption and desorption ability to reactant.

4.5.7　UV-Vis Spectroscopy Analysis

The UV-Vis spectroscopy analyses were performed for Ni-doped thin films as shown in Figure 4.64. It showed that the 100 mol% Ni-doped thin film has the highest absorbance value while the 40 mol% Ni-doped thin film has the lowest absorbance valued. The 10, 80 and 20 mol% Ni-doped thin films showed the second, third and fourth highest absorbance value respectively. The absorbance of the thin films is proportional to its thickness which is in agreement with the Beer-Lambert's law. Tauc plot was constructed based on the UV-Vis finding in order to investigate the band gap of the thin film. Table 4.16 was tabulated corresponding to the band gaps and thickness of different mol% of Ni-doped thin films. The Tauc plot shown in Figure 4.65 and it was observed that there were three types of band gap values according to the materials present in the

thin films. Band gap values at ~1.60, ~1.90 and ~2.30 eV were corresponded to

Mo$_3$NiS$_4$, MoS$_2$ and Mo$_2$S$_3$, respectively.
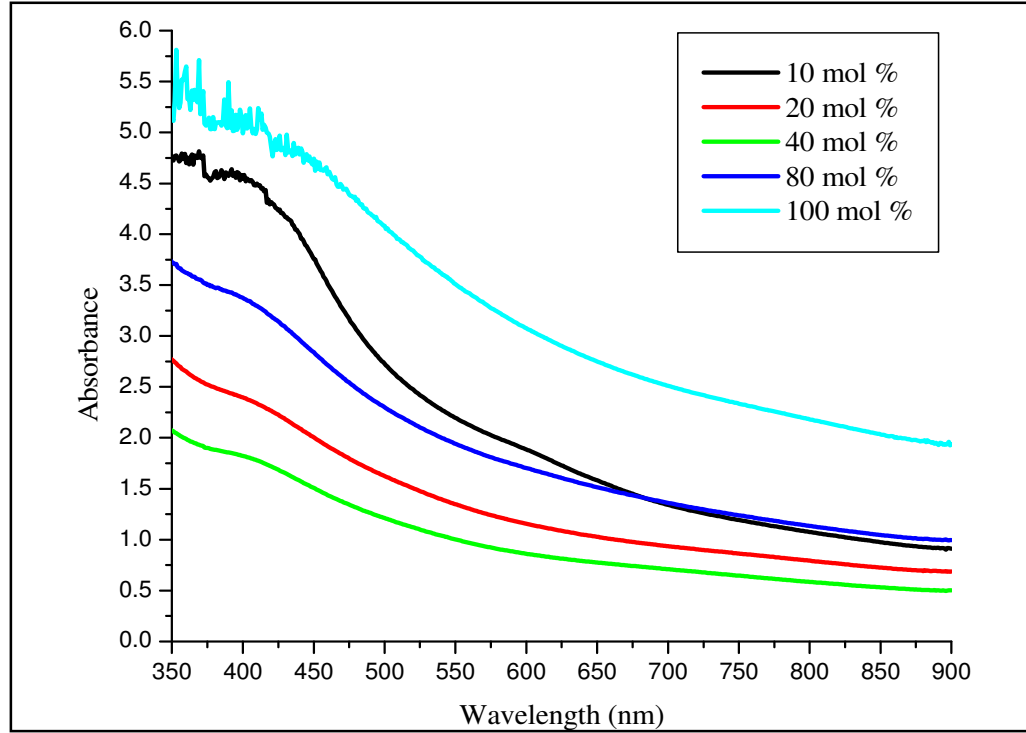
Figure 4.64: UV-Vis for 10, 20, 40, 80 and 100 mol% of Ni-doped thin films.

Table 4.16: Band gaps correspond to various mol% of Ni-doped thin films

Mol % of Co doping	Cross section thickness (nm)	Band gap (eV)		
10	370	1.68	1.92	2.21
20	299	1.62	1.89	2.21
40	174	1.61	1.94	2.21
80	344	1.62	1.97	2.22
100	561	1.66	1.90	2.16
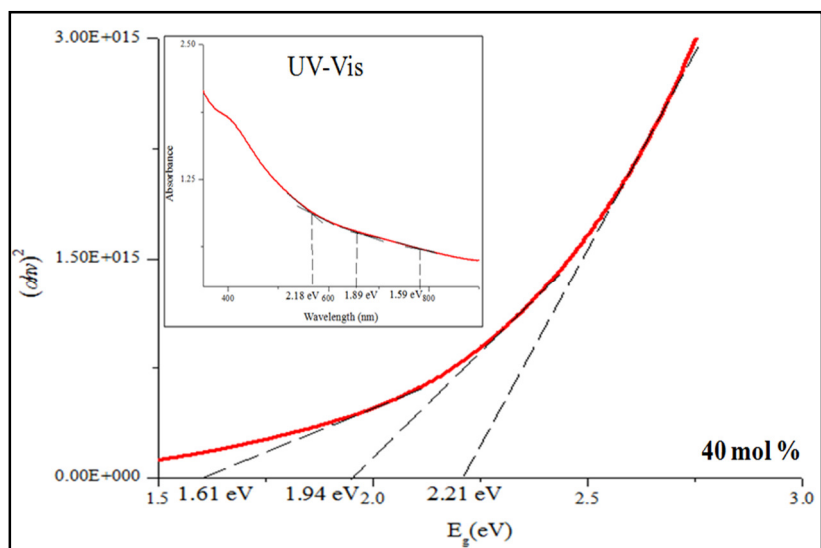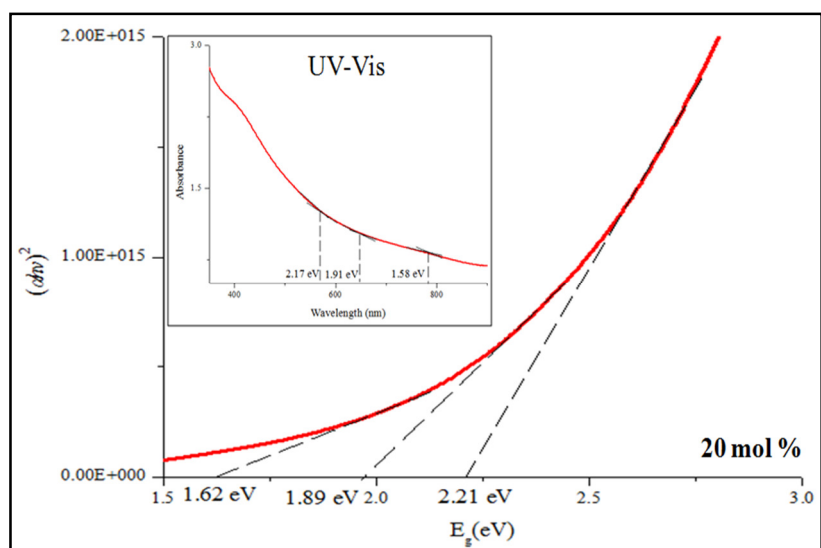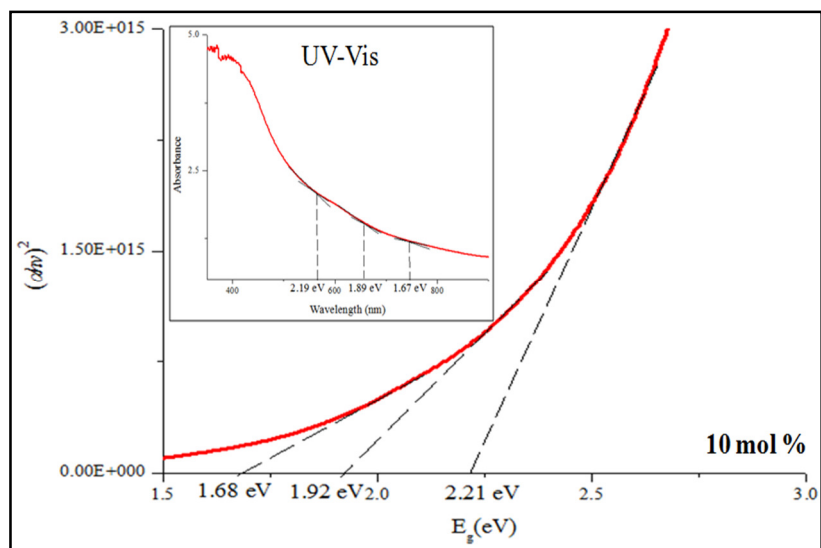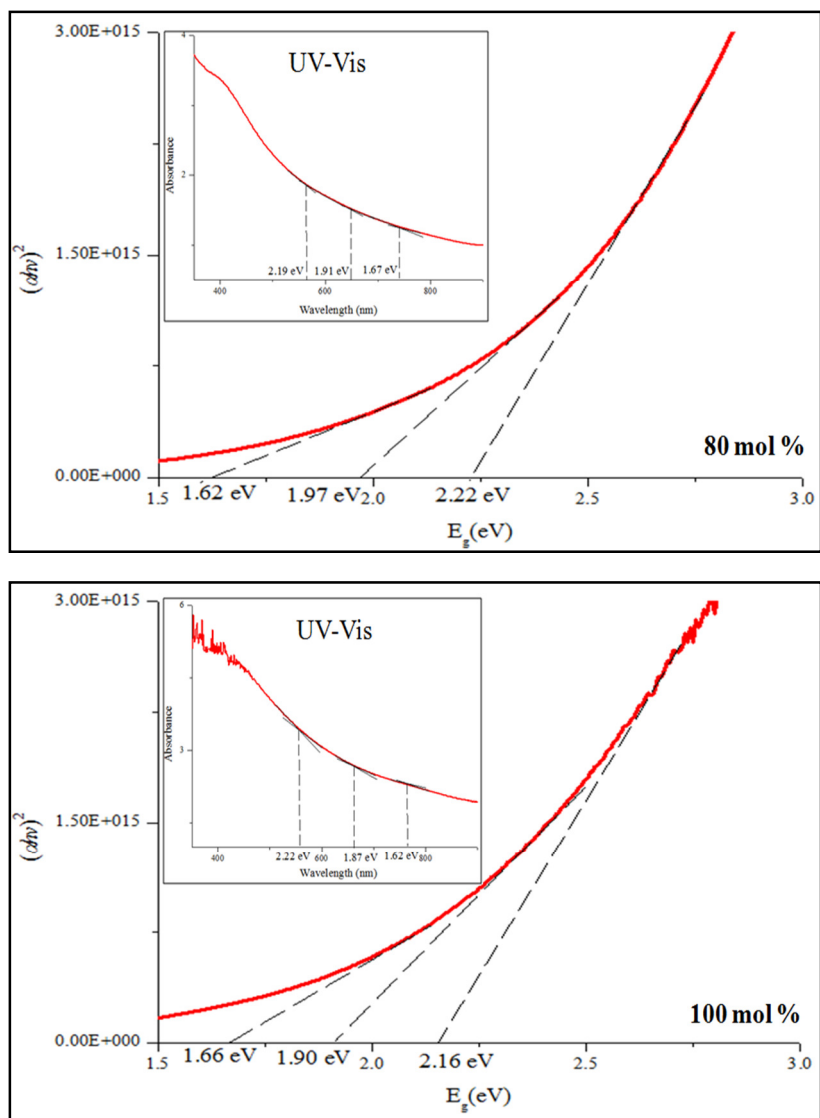
Figure 4.65: Tauc plot for 10, 20, 40, 80, and 100 mol% of Ni-doped thin films.

4.5.8 Photoelectrochemical (PEC) Water Splitting Studies

From the J-V curves of Ni-doped thin films conducted in both dark and light conditions as shown in Figure 4.66, the 10 mol% Ni-doped thin film showed the highest current density which was 1.445 and 1.560 mA/cm^2 in dark and light conditions, respectively. It has the highest charge density because according to Van Zeghbroeck high amount of dopant resulted in electron scattering which will reduce the electron mobility. Therefore, the lowest amount of dopants in Ni-doped thin films series gave better current density as it will promote photoelectrochemical activity by electron hole trapping process (Van Zeghbroeck, 2004). The 20 mol% Ni-doped thin film gave the lowest current density of 0.194 (dark) and 0.199 (light) mA/cm^2. A drastic change in current density was observed when the Ni dopant was increased to 40 mol% resulting in the current density surges to 0.516 and 0.534 mA/cm^2 in dark and light condition, respectively. This could be due to changes from the granular to flakes morphology as it exhibits more active sites for water splitting process. As the dopant percentage increases to 80 and 100 mol%, the current density decreases to 0.325 and 0.263 mA/cm^2, respectively, in dark condition while in light condition the current density was 0.336 and 0.308 mA/cm^2, respectively. The current density for Ni series was tabulated in Table 4.17.
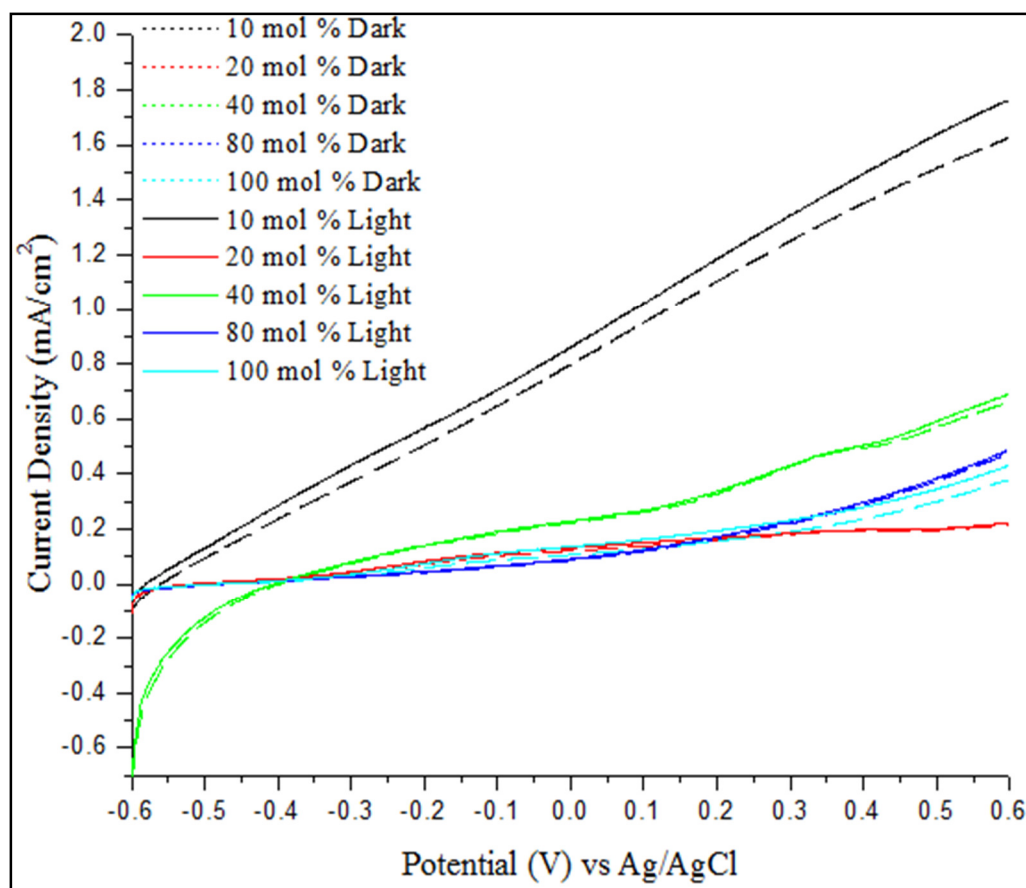
Figure 4.66: J-V curve for various mol% Ni-doped thin films.

It is observed in the Figure 4.67 that the 10 mol% Ni-doped thin film has showed the lowest impedance with the smallest diameter while the 20 mol% Ni-doped thin film had showed the highest impedance in the Ni series. It was noted that 10 and 20 mol% Ni-doped thin films have different morphology compared to 40, 80 and 100 mol% Ni-doped thin films. Thus, the impedance as well as other photocatalytic activities may not be comparable. This is because the flakes morphology generally has a lower impedance when compare to the granular morphology as it has larger surface area at the interface of the thin film and the surrounding electrolyte during the PEC process. As for 40, 80 and 100 mol% Ni-

doped thin film in dark condition, 100 mol% Ni-doped thin film showed the lowest impedance followed by 80 mol% and eventually 40 mol% Ni-doped thin film. This is in agreement with Van Zeghbroeck's statement where the sheet resistivity is inversely proportional to the thin film thickness based on the formula $R_s = \frac{r}{t}$, where R_s, r and t is sheet resistivity, resistance and thin film thickness, respectively (Van Zeghbroeck, 2004). However, the impedance of 100 mol% Ni-doped thin film became slightly higher than 80 mol% Ni-doped thin film in light condition. This could be due to the fact that 100 mol% Ni-doped thin film has a non-homogenous morphology. Notably even though the impedance increases inversely with the thin film thickness, the current density is affected by electron mobility which was affected by the amount of dopant in the thin film (Van Zeghroeck, 2004). Bode plot was used to find out the lifetime of the electron-hole separation of the tin films. From the lifetime, 20 mol% has lifetime of 0.628 ms which is slightly higher than 10 mol% which was 0.505. Nevertheless, the electron mobility which was affected by the amount of dopant has more significant effect in current density of the thin film because higher amount of dopant may cause electron scattering by the dopant and eventually leads to lower electron mobility. This observation can be seen for 20, 40, 80 and 100 mol% Ni-doped thin films. It was noteworthy that all thin films in the Ni-doped thin films series also showed a relatively small charge lifetime because it was proposed that the presence of dopant could also act as the recombination site during the electron hole trapping process.
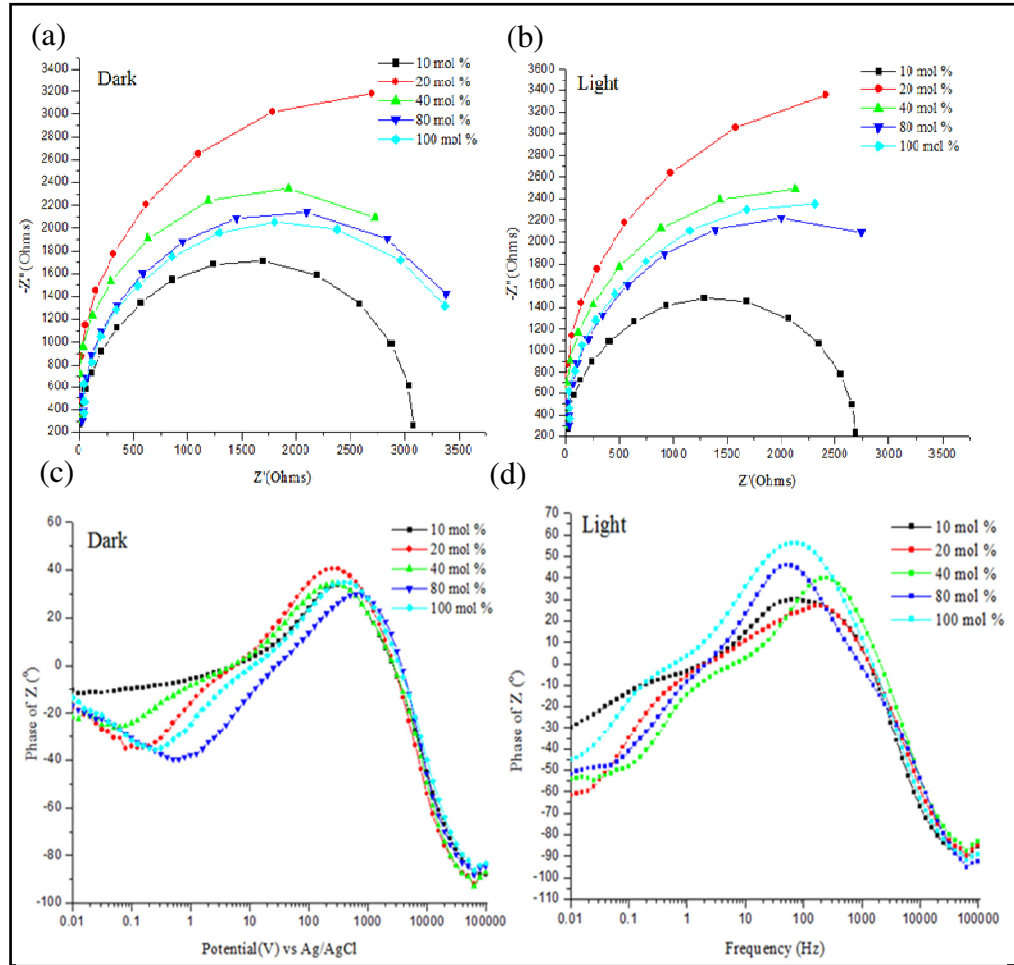
Figure 4.67: (a,b) Nyquist plots and (c,d) Bode plots for various mol% of Ni-doped thin films in different conditions (dark and light).

Table 4.17: Comparisons of PEC activities for various mol% Ni-doped thin film

Mol %	J_D (mA/cm^2) At 1.23 V vs RHE	J_L (mA/cm^2) At 1.23 V vs RHE	Photo-sensitivity J_L/J_D At 1.23V vs RHE	Frequency Maxima Hz	Life time $\tau = 1/2\pi\upsilon$ (ms)
10	1.445	1.560	1.080	315.284	0.505
20	0.194	0.199	1.026	253.582	0.628
40	0.516	0.534	1.035	252.036	0.631
80	0.325	0.336	1.034	648.128	0.246
100	0.263	0.308	1.171	417.348	0.381

The charge densities were determined from the Mott-Schottky plot. From the calculation, it was observed that the charge density for 10, 20, 40, 80 and 100 mol% Ni-doped were 6.1929×10^{20}, 7.3140×10^{19}, 4.3302×10^{20}, 6.4846×10^{20} and 1.5270×10^{20} cm^{-3}, respectively. The charge density was tabulated in Table 4.18. Similar to Fe and Co series, the negative slope from the Mott-Schottky plot had indicated that the thin film is a p-type semiconductor (Lim et al., 2019). The charge density from the Mott-Schottky plot is in agreement with the current density where current density was proportional to the charge density. However, 80 mol% Ni-doped thin film showed an unusual charge density as it has the highest value even though the 10 mol% has the highest photocurrent density value. One of the possible factor that cause the 80 mol% has the highest charge density would be its flakes morphology where it would have a larger surface area at the interface of thin film and surrounding electrolytes when compare to the 10 mol% Ni-doped thin film which have a granular morphology. It should be noted that the disadvantage of Mott-Schottky analysis is complicated depending on the sample composition and morphology. According to Chen et al., the ideal sample for Mott-Schottky analysis should be single-crystal material with high crystallinity as well as moderate amount of dopant (Chen, Dinh and Miller, 2013). The non-ideal samples may require full evaluation of the frequency range which may take decades, followed by fitting with appropriate data with complicated circuit model (Macdonal and Barsukov, 2005; Le Formal et al., 2011).
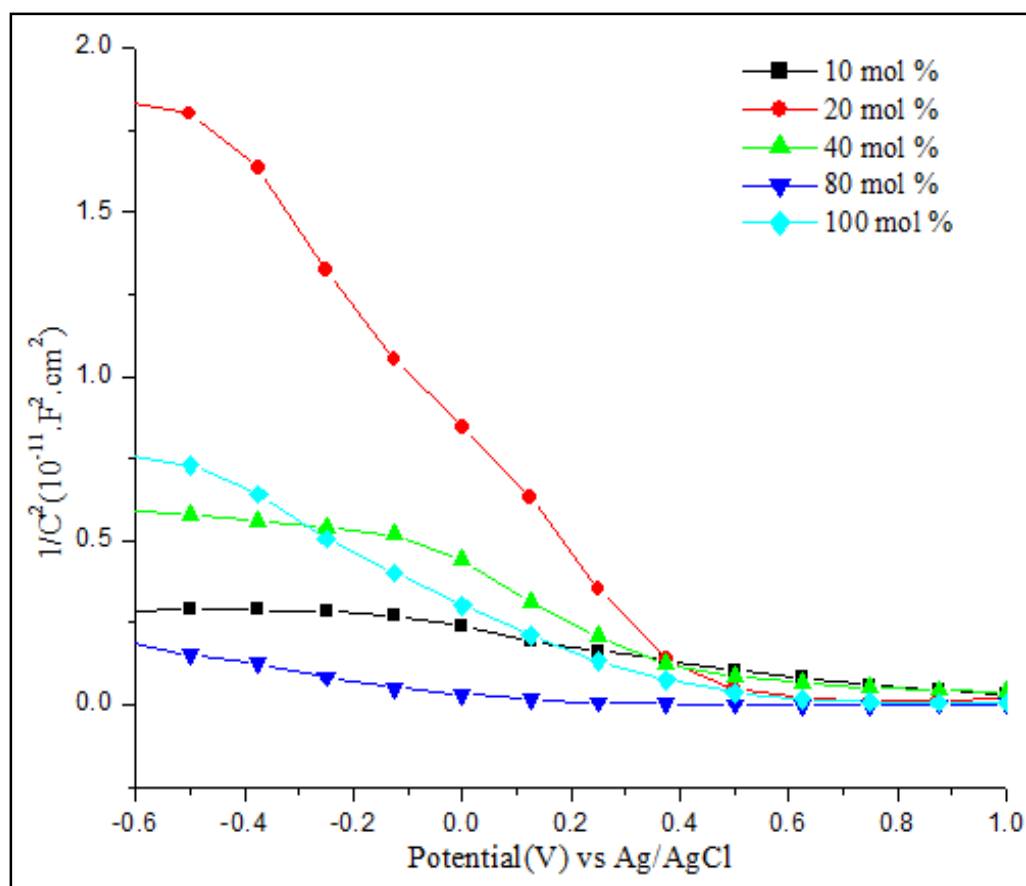
Figure 4.68: Mott-Schottky plot for Ni-doped thin films.

Table 4.18: Charge densities for various mol% of Ni-doped thin films

Percentage of Ni doping (%)	Charge densities (cm^{-3})
10	6.1929×10^{20}
20	7.3140×10^{19}
40	4.3302×10^{20}
80	6.4846×10^{20}
100	1.5270×10^{20}

4.5.9 Mechanism of Electron Transfer Process for Ni-series

The conduction and valence band potential of Mo_3NiS_4 were -0.11 and 1.49 eV, respectively. The electrons and holes flow for the Ni-doped thin film is shown in figure 4.69 where the flow was from Mo_2S_3, Mo_3NiS_4 and then to MoS_2. The coupling of three different band gaps could extend the spectral range of absorption and improves the electron-holes separation. Moreover, the electron-holes recombination was also suppressed due to electron and holes trapping since they will be photo-induced into the neighboring material. The electrons will eventually flow into the fluorine-doped tin oxide substrate and then to the platinum (Pt) electrode for redox process.
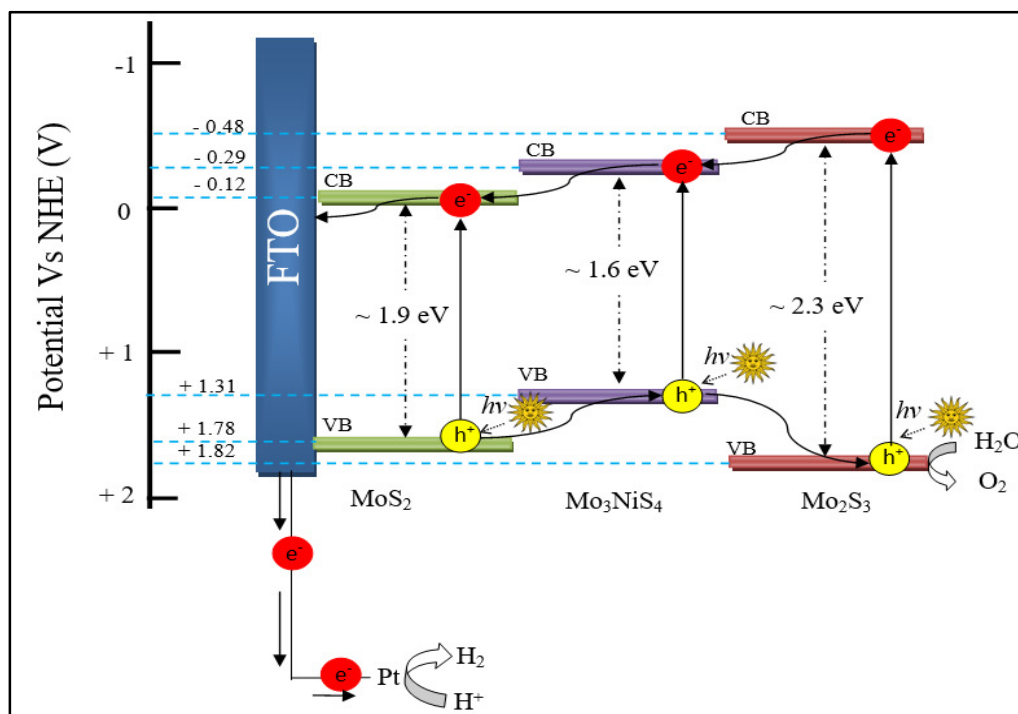
Figure 4.69: Proposed Z-scheme mechanism for Ni-doped thin film.

4.6 Comparison of Fe-, Co- and Ni-doped Thin Film Series for Photoelectrochemical Activity

Despite of different dopant may alter the physical and optical properties of MoS_2/Mo_2S_3 thin films that will eventually affect the photoelectrochemical activity, the types of dopants and the amount of dopants that was doped into the thin films has the largest significant impact. It was observed that the 40 mol% Fe-doped thin film showed the best photoelectrochemical activity in the Fe-doped thin film series. As for the Co- and Ni-doped thin films series, the best photoelectrochemical activity was 10 mol% Co- and Ni-doped thin films. The current density in the dark condition at 0.6 V for Fe-, Co- and Ni-doped thin film were 1.353, 2.411 and 1.445 mA/cm^2, respectively. In light conditions, the photocurrent density at 0.6 V for Fe-, Co- and Ni-doped thin film were 1.645, 2,497 and 1.560 mA/cm^2, respectively. Therefore, the best dopant for enhancing the MoS_2/Mo_2S_3 thin film would be the Co dopant, followed by Ni and Fe dopant. This was in accordance to the elemental conductivity of the iron triads where the conductivity for Fe, Co and Ni is 1.0×10^7, 1.7×10^7, 1.4×10^7 S/m, respectively (Petrucci, Cunningham and Moore., 1989). It was worth to emphasize that even though the photocurrent density of 40 mol% was Fe-doped thin film was slightly higher compared to the 10 mol% Ni-doped thin film, the at % of Fe-doped thin film was higher compare to the latter. Table 4.19 was tabulated for comparison of different types of dopant for its photocatalytic activity in dark and light conditions.

Table 4.19: Comparison of different types of dopant for its photocatalytic activity in dark and light conditions

Series (Atomic percentage of respective dopant)	Photocurrent density at 0.6 V (mA/cm^2)	
	Dark	Light
40 mol % Fe-doped thin film (2.43 at %)	1.353	1.645
10 mol % Co-doped thin film (0.91 at %)	2.411	2.597
10 mol %Ni-doped thin film (0.95 at %)	1.445	1.560

CHAPTER 5

CONCLUSIONS

The iron triads which are Fe, Co and Ni were successfully doped into a mixture of MoS_2/Mo_2S_3. It was observed that different dopants in different mol% may give wider range of physical and optical properties of the thin films. In this study, it was concluded that the 10 mol% Co-doped thin film showed the best photocatalytic activity with the photocurrent density of 2.497 mA/cm^2 in light condition. For Fe-doped thin film, the 40 mol% Fe-doped thin film has highest the photocurrent density of 1.645 mA/cm^2 at 0.6 V in light conditions. Finally, for the Ni series, the 10 mol% Ni-doped thin film had shown its highest photocurrent density of 1.560 mA/cm^2 at 0.6 V in light conditions. The performance of the M-doped thin film (M = Fe, Co, Ni) was found to be related to their nature in the electrical conductivity where Co has the highest electrical conductivity of 1.7×10^7 S/m followed by Ni and Fe with the electrical conductivity of 1.4×10^7 and 1.0×10^7 S/m, respectively.

FUTURE STUDY

From this study, it was observed that the type of dopants and its amount give different effects on the photocatalytic activity for MoS_2/Mo_2S_3. Therefore, it is interesting to study (tandem) multi-junction thin films where two or more materials with different band gaps/absorption spectra layered on top of each other. This type of thin film can capture more of the incident light as compared to the single material. Apart from water splitting, the semiconductor is applicable to increase the efficiency of silicon photovoltaic cell to convert solar energy into electrical energy. The most common single junction solar cell will be made out of silicon. Thus, it will be interesting to layer the MoS_2/Mo_2S_3 on the silicon wafer to study the power conversion of solar energy to electrical energy since it was found that MoS_2/Mo_2S_3 involves electron-hole separation where the concept is similar to the photovoltaic cell.

REFERENCES

Al-Dulaimi, N., Lewis, D.J., Zhong, X.L., Malik, M.A. and O'Brien, P., 2016. Chemical vapor deposition of rhenium disulfide and rhenium-doped molybdenum disulfide thin films using single-source precursors. *Journal of Materials Chemistry*, *4*(12), pp.2312-2318.

Aljarb, A., Cao, Z., Tang, H.L., Huang, J.K., Li, M., Hu, W., Cavallo, L. and Li, L.J., 2017. Substrate Lattice-Guided Seed Formation Controls the Orientation of 2D Transition-Metal Dichalcogenides. *ACS nano*, *11*(9), pp.9215-9222.

Andoshe, D.M., Jeon, J.M., Kim, S.Y. and Jang, H.W., 2015. Two-dimensional transition metal dichalcogenide nanomaterials for solar water splitting. *Electronic Materials Letters*, *11*(3), pp.323-335.

Babu, G., Masurkar, N., Al Salem, H. and Arava, L.M.R., 2016. Transition metal dichalcogenide atomic layers for lithium polysulfides electrocatalysis. *Journal of the American Chemical Society*, *139*(1), pp.171-178.

Bamwenda, G.R., Tsubota, S., Nakamura, T. and Haruta, M., 1995. Photoassisted hydrogen production from a water-ethanol solution: a comparison of activities of Au-TiO_2 and Pt-TiO_2. *Journal of Photochemistry and Photobiology A: Chemistry*, *89*(2), pp.177-189.

Bhattacharjee, A., Rooj, A., Roy, D., & Roy, M., 2014. Thermal decomposition study of ferrocene [$(C_5H_5)_2Fe$]. *Journal of Experimental Physics*, *2014*.

Birdwhistell, R., Hackett, P. and Manning, A.R., 1978. A simple and effective preparation of (η-$RC_5H_4)_2M_2(CO)_6$ complexes (M = Cr, Mo, and W). *Journal of Organometallic Chemistry*, *157*(2), pp.239-241.

Bonde, J., Mosses, P.G., Jaramillo, T.F., Norskov, J.K. and Chorkendorff, I., 2009. Hydrogen evolution on nano-particulate transitionmetal sulfides. *Faraday discussions, 140,* pp. 219-231.

Bujang, A.S., Bern, C.J. and Brumm, T.J., 2016. Summary of energy demand and renewable energy policies in Malaysia. *Renewable and Sustainable Energy Reviews, 53,* pp. 1459-1467.

Cai, Z., Liu, B., Zou, X. and Cheng, H.M., 2018. Chemical vapor deposition growth and applications of two-dimensional materials and their heterostructures. *Chemical reviews.*

Cain, J.D., Shi, F., Wu, J. and Dravid, V.P., 2016. Growth mechanism of transition metal dichalcogenide monolayers: the role of self-seeding fullerene nuclei. *ACS nano*, *10*(5), pp.5440-5445.

Chen, J., Zhao, X., Tan, S.J., Xu, H., Wu, B., Liu, B., Fu, D., Fu, W., Geng, D., Liu, Y. and Liu, W., 2017. Chemical vapor deposition of large-size monolayer MoSe$_2$ crystals on molten glass. *Journal of the American Chemical Society*, *139*(3), pp.1073-1076.

Chen, L., Liu, B., Abbas, A.N., Ma, Y., Fang, X., Liu, Y. and Zhou, C., 2014. Screw-dislocation-driven growth of two-dimensional few-layer and pyramid-like WSe$_2$ by sulfur-assisted chemical vapor deposition. *ACS nano*, *8*(11), pp.11543-11551.

Chen, X., Li, C., Gratzel, M., Kostecki, R. and Mao, S.S., 2012. Nanomaterials for renewable energy production and storage. *Chemical Society Reviews*, 41(23), pp. 7909-7937.

Chen, Z., Dinh, H.N. and Miller, E., 2013. *Photoelectrochemical water splitting* (pp. 68-72). New York: Springer.

Cheng, J., Jiang, T., Ji, Q., Zhang, Y., Li, Z., Shan, Y., Zhang, Y., Gong, X., Liu, W. and Wu, S., 2015. Kinetic Nature of Grain Boundary Formation in As-Grown MoS2 Monolayers. *Advanced Materials*, *27*(27), pp.4069-4074

Choy, K.L., 2003. Chemical vapour deposition of coatings. *Progress in materials science*, *48*(2), pp.57-170.

Clarke, D.R., 1989. Intergranular phases in polycrystalline ceramics. *Surfaces and Interfaces of Ceramic Materials* (pp. 57-79) Springer, Dordrecht.

Colmenares, J.C., Luque, R., Campelo, J.M., Colmenares, F., Karpiński, Z. and Romero, A.A., 2009. Nanostructured photocatalysts and their applications in the photocatalytic transformation of lignocellulosic biomass: an overview. *Materials*, *2*(4), pp.2228-2258.

Dai, X., Du, K., Li, Z., Liu, M., Ma, Y., Sun, H., Zhang, X. and Yang, Y., 2015. Co-doped MoS_2 nanosheets with the dominant CoMoS phase coated on carbon as an excellent electrocatalyst for hydrogen evolution. *ACS applied materials & interfaces*, *7*(49), pp.27242-27253.

Deepak, F.L., Esparza, R., Borges, B., Lopez-Lozano, X. and Jose-Yacaman, M., 2011. Direct imaging and identification of individual dopant atoms in MoS_2 and WS_2 catalysts by aberration corrected scanning transmission electron microscopy. *American Chemical Society Catalysis*, 1(5), pp.537-543.

Domen, K., Naito, S., Soma, M., Onishi, T. and Tamaru, K., 1980. Photocatalytic decomposition of water vapour on an $NiO–SrTiO_3$ catalyst. *Journal of the Chemical Society, Chemical Communications*, (12), pp.543-544.

Dong, H., Chen, G., Sun, J., Feng, Y., Li, C. and Lv, C., 2014. Stability, durability and regeneration ability of a novel Ag-based photocatalyst, $Ag_2Nb_4O_{11}$. *Chemical Communications*, *50*(50), pp.6596-6599.

Dumcenco, D., Ovchinnikov, D., Marinov, K., Lazic, P., Gibertini, M., Marzari, N., Sanchez, O.L., Kung, Y.C., Krasnozhon, D., Chen, M.W. and Bertolazzi, S., 2015. Large-area epitaxial monolayer MoS2. *ACS nano*, *9*(4), pp.4611-4620.

Eda, G., Ball, J., Mattevi, C., Acik, M., Artigilia, L, Granozzi, G., Chabal, Y., Anthopoulos, T.D. and Chhowalla, M., 2011. Partially oxidized graphene as precursor to graphene. *Journal of MaterialsChemistr,21*(30), pp. 11217-11223.

Eichfeld, S.M., Hossain, L., Lin, Y.C., Piasecki, A.F., Kupp, B., Birdwell, A.G., Burke, R.A., Lu, N., Peng, X., Li, J. and Azcatl, A., 2015. Highly scalable, atomically thin WSe2 grown via metal–organic chemical vapor deposition. *ACS nano*, *9*(2), pp.2080-2087.

Elias, A.L., Perea-Lopez, N., Castro-Beltran, A., Berkdemir. A., Lv, R., Feng, S., Long, A.D., Hayashi, T., Kim, Y.A., Endo, M. and Gutierrez, H.R., 2013. Controlled synthesis and transfer of large-area WS2 sheets: from single layer to few layes. *ACS nano, 7*(6), pp. 5235-5242.

Feng, J.X., Xu, H., Dong, Y.T., Lu, X.F., Tong, Y.X. and Li, G.R., 2017. Efficient hydrogen evolution electrocatalysis using cobalt nanotubes decorated with titanium dioxide nanodots. *Angewandte Chemie International Edition*, *56*(11), pp.2960-2964.

Feng, L.L., Li, G.D., Liu, Y., Wu, Y., Chen, H., Wang, Y., Zou, Y.C., Wang, D. and Zou, X., 2015. Carbon-armored Co9S8 nanoparticles as all-pH efficient and durable H2-evolving electrocatalysts. *ACS applied materials & interfaces*, *7*(1), pp.980-988.

Fujishima, A. and Honda, K., 1972. Electrochemical photolysis of water at a semiconductor electrode. *nature*, 238(5358), pp.37.

Galun, E., Cohen, H., Margulis, L., Vilan, A., Tsirlina, T., Hodes, G., Tenne, R., Hershkinfel, M., Jaegermann, W. and Ellmer, K., 1995. Crystallization of layered metal-dichalcogenides films on amorphous substrates. *Applied physics letters*, 67(23), pp. 3474-3476.

Gao, Y., Hong, Y.L., Yin, L.C., Wu, Z., Yang, Z., Chen, M.L., Liu, Z., Ma, T., Sun, D.M., Ni, Z. and Ma, X.L., 2017. Ultrafast Growth of High-Quality Monolayer WSe$_2$ on Au. *Advanced Materials*, *29*(29), p.1700990.

Gao, Y., Liu, Z., Sun, D.M., Huang, L., Ma, L.P., Yin, L.C., Ma, T., Zhang, Z., Ma, X.L., Peng, L.M. and Cheng, H.M., 2015. Large-area synthesis of high-quality and uniform monolayer WS$_2$ on reusable Au foils. *Nature communications*, *6*, p.8569.

Gong, Y., Li, B., Ye, G., Yang, S., Zou, X., Lei, S., Jin, Z., Bianco, E., Vinod, S., Yakobson, B.I. and Lou, J., 2017. Direct growth of MoS$_2$ single crystals on polyimide substrates. *2D Materials*, *4*(2), p.021028.

Grosvenor, A.P., Kobe, B.A., Biesinger, M.C. and McIntyre, N.S., 2004. Investigation of multiplet splitting of Fe 2p XPS spectra and bonding in iron compounds. *Surface and Interface Analysis: An International Journal devoted to the development and application of techniques for the analysis of surfaces, interfaces and thin films*, *36*(12), pp.1564-1574.

Habisreutinger, S.N., Schmidt-Mende, L. and Stolarczyk, J.K., 2013. Photocatalytic reduction of CO$_2$ on TiO$_2$ and other semiconductors. *Angewandte Chemie International Edition*, *52*(29), pp.7372-7408.

Han, S.A., Sohn, A. and Kim, S.W., 2017. Recent advanced in energy harvesting and storage applications with two-dimensional layered materials. *FlatChem*.

He, Y., Sobhani, A., Lei, S., Zhang, Z., Gong, Y., Jin, Z., Zhou, W., Yang, Y., Zhang, Y., Wang, X. and Yakobson, B., 2016. Layer engineering of 2D semiconductor junctions. *Advanced Materials*, *28*(25), pp.5126-5132.

Hisatomi, T., Kubota, J. and Domen, K., 2014. Recent advances in semiconductors for photocatalytic and photoelectrochemical water splitting. *Chemical Society Reviews*, *43*(22), pp.7520-7535.

Ho, T.A., Bae, C., Lee, S., Kim, M., Montero-Moreno, J.M., Park, J.H. and Shin, H., 2017. Edge-on MoS_2 thin films by atomic layer deposition for understanding the interplay between the active area and hydrogen evolution reaction. *Chemistry of Materials*, *29*(17), pp.7604-7614.

Hodes, G. and Kamat, P.V., 2015. Understanding the implication of carrier diffusion length in photovoltaic cells. *The Journal of Physical Chemistry Letters,*6, pp. 4090-4092.

Huang, H., Zhou, J., Liu, H., Zhou, Y. and Feng, Y., 2010. Selective photoreduction of nitrobenzene to aniline on TiO_2 nanoparticles modified with amino acid. *Journal of hazardous materials*, *178*(1-3), pp.994-998.

Jaafar, S.N.H., Minggu, L.J., Arifin, K., Kassim, M.B. and Wan, W.R.D., 2017. Natural dyes as TIO_2 sensitizers with membranes for photoelectrochemical water splitting: An overview. *Renewable and Sustainable Energy Reviews*, *78*, pp.698-709.

Jeong, H.Y., Jin, Y., Yun, S.J., Zhao, J., Baik, J., Keum, D.H., Lee, H.S. and Lee, Y.H., 2017. Heterogeneous Defect Domains in Single-Crystalline Hexagonal WS_2. *Advanced Materials*, *29*(15), p.1605043.

Ji, Q., Zhang, Y., Gao, T., Zhang, Y., Ma, D., Liu, M., Chen, Y., Qiao, X., Tan, P.H., Kan, M. and Feng, J., 2013. Epitaxial monolayer MoS_2 on mica with novel photoluminescence. *Nano letters*, *13*(8), pp.3870-3877.

Jin, S., Bierman, M.J. and Morin, S.A., 2010. A new twist on nanowire formation: Screw-dislocation-driven growth of nanowires and nanotubes. *The Journal of Physical Chemistry Letters*, *1*(9), pp.1472-1480.

Joy, J., Mathew, J. and George, S.C., 2018. Nanomaterials for photoelectrochemical water splitting-review. *International journal of hydrogen energy, 43*(10), pp. 4804-4817.

Katz, M.J., Riha, S.C., Jeong, N.C., Martinson, A.B., Farha, O.K. and Hupp, J.T. 2012. Towards solar fuels: Water splitting with sunlight and "rust"?. *Coordination Chemistry Reviews*, 256(21-22), pp. 2521-2529.

Kang, K., Xie, S., Huang, L., Han, Y., Huang, P.Y., Mak, K.F., Kim, C.J., Muller, D. and Park, J., 2015. High-mobility three-atom-thick semiconducting films with wafer-scale homogeneity. *Nature*, *520*(7549), pp. 656.

Kim, T.W. and Choi, K.S., 2014. Nanoporous $BiVO_4$ photoanodes with dual-layer oxygen evolution catalysts for solar water splitting. *Science*, *343*(6174), pp.990-994.

King, R.B., 1963. Organosulfur Derivatives of the Metal Carbonyls. V. The Reactions between Certain Organic Sulfur Compounds and Various Cyclopentadienyl Metal Carbonyl Derivatives. *Journal of the American Chemical Society*, *85*(11), pp.1587-1590.

Knapp, C.E. and Carmalt, C.J., 2016. Solution based CVD of main group materials. *Chemical Society Reviews*, *45*(4), pp. 1036-1064.

Komsa, H.P., Kotakoski, J., Kurasch, S., Lehtinen, O., Kaiser, U. and Krasheninnikov, A.V., 2012. Two-dimensional transition metal dichalcogenides under electron irradiation: defect production and doping. *Physical review letters*, *109*(3), p.035503.

Kong, X., Wang, N., Zhang, Q., Liang, J., Wang, M., Wei, C., Zhao, Y. and Zhang, X., 2018. Ni-doped MoS_2 as an Efficient Catalyst for Electrochemical Hydrogen Evolution in Alkine Media. *Chemistry Select*, *3*, pp. 9493-9498.

Kou, J., Lu, C., Wang, J., Chen, Y., Xu, Z. and Varma, R.S., 2017. Selectivity enhancement in heterogeneous photocatalytic transformations. *Chemical reviews*, *117*(3), pp.1445-1514.

Kudo, A., & Miseki, Y., 2009. Heterogeneous photocatalyst materials for water splitting. *Chemical Society Reviews*, *38*(1), pp.253-278.

Lan, Y.W., Torres Jr, C.M., Tsai, S.H., Zhu, X., Shi, Y., Li, M.Y., Li, L.J., Yeh, W.K. and Wang, K.L., 2016. Atomic-Monolayer MoS_2 Band-to-Band Tunneling Field-Effect Transistor. *Small*, *12*(41), pp.5676-5683.

Le Formal, F., Tetreault, N., Cornuz, M., Moehl, T., Grätzel, M. and Sivula, K., 2011. Passivating surface states on water splitting hematite photoanodes with alumina overlayers. *Chemical Science*, *2*(4), pp.737-743.

Leonhardt, A., Hampel, S., Mueller, C., Moench, I., Koseva, R., Ritschel, M., Elefant, D., Biedermann, K. and Buechner, B., 2006. Synthesis, Properties, and Applications of Ferromagnetic-Filled Carbon Nanotubes. *Chemical vapor deposition*, *12*(6), pp.380-387.

Lewis, D. J., Tedstone, A. A., Zhong, X. L., Lewis, E. A., Rooney A., Savjani, N., Brent, J. R., Haigh, S. J., Burke, G., Muryn, C. A., Raftery, J. M., Warrens, C., West, K., Gaemers, S. and O' Brien, P., 2015. Chemistry of Materials. *Thin Films of Molybdenum Disulfide Doped with Chromium by Aerosol-Assisted Chemical Vapor Deposition (AACVD),* 27 (4), pp 1367–1374.

Li, B., Gong, Y., Hu, Z., Brunetto, G., Yang, Y., Ye, G., Zhang, Z., Lei, S., Jin, Z., Bianco, E. and Zhang, X., 2016. Solid–Vapor Reaction Growth of Transition-Metal Dichalcogenide Monolayers. *Angewandte Chemie*, *128*(36), pp.10814-10819.

Li, H., Zhang, Q., Yap, C.C.R., Tay, B.K., Edwin, T.H.T, Olivier, A. and Baillargeat, D., 2012. From bulk to monolayer MoS_2: evolution of Raman scattering. *Advanced Functional Materials, 22*(7), pp. 1385-1390.

Li, J. and Wu, N., 2015. Semiconductor-based photocatalysts and photoelectrochemical cells for solar fuel generation: a review. *Catalysis Science & Technology*, 5(3), pp.1360-1384.

Li, X. and Zhu, H., 2015. Two-dimensional MoS_2: Properties, preparation, and applications. *Journal of Materionics,* 1(1), pp.33-44.

Liu, B., Fathi, M., Chen, L., Abbas, A., Ma, Y. and Zhou, C., 2015. Chemical vapor deposition growth of monolayer WSe_2 with tunable device characteristics and growth mechanism study. *Acs Nano*, *9*(6), pp.6119-6127.

Liu, G., Wang, L., Yang, H.G., Cheng, H.M. and Lu, G.Q.M., 2010. Titania-based photocatalysts-crystal growth, doping and heterostructuring. *Journal of Materials Chemistry*, *20*(5), pp.831-843.

Lim, C.E., Ooi, M.L., Wong, R.C.S., Neo, K.E., Mumtaz, A., Mazhar, M., Mohamed, N.M. and Saheed, M.S.M., 2019. Facile Synthesis of Molybdenum Multisulfide Composite Nanorod Arrays from Single Source Precursor for Photoelectrochemical Hydrogen Generation. *Applied nanoscience,* 1-12.

Lin, Z., Carvalho, B.R., Kahn, E., Lv, R., Rao, R., Terrones, H., Pimenta, M.A. and Terrones, M., 2016. Defect engineering of two-dimensional transition metal dichalcogenides. *2D Materials*, 3(2), p.022002.

Lince, J. R., Hilton, M. R., and Bommannavar, A. S., 1995. EXAFS of sputter-deposited MoS_2 films. *Thin Solid Films*, 264(1), pp. 120-134.

Lousada, C.M., Pinto, S.S., Canongia Lopes, J.N., Minas da Piedade, M.F., Diogo, H.P. and Minas da Piedade, M.E., 2008. Experimental and molecular dynamics simulation study of the sublimation and vaporization energetics of iron metalocenes. Crystal structures of $Fe(\eta^5$-$C_5H_4CH_3)_2$ and $Fe[(\eta^5$-$(C_5H_5)(\eta^5$-$C_5H_4CHO)]$. *The Journal of Physical Chemistry A*, *112*(13), pp.2977-2987.

Luo, Y.Y., Pan, S.S., Xu, S.C., Zhong, L., Wang, H. and Li, G.H., 2016. Influence of sputtering power on the phase transition performance of VO_2 thin films grown by magnetron sputtering. *Journal of Alloys and Compounds*, *664*, pp.626-631.

Ly, T.H., Zhao, J., Kim, H., Han, G.H., Nam, H. and Lee, Y.H., 2016. Vertically conductive MoS2 spiral pyramid. *Advanced Materials*, *28*(35), pp.7723-7728.

Ma, Q., Isarraraz, M., Wang, C.S., Preciado, E., Klee, V., Bobek, S., Yamaguchi, K., Li, E., Odenthal, P.M., Nguyen, A. and Barroso, D., 2014. Postgrowth tuning of the bandgap of single-layer molybdenum disulfide films by sulfur/selenium exchange. *ACS nano*, *8*(5), pp.4672-4677.

Ma, D., Tang, Y., Yang, G., Zeng, J., He, C. and Lu, Z., 2015. CO catalytic oxidation on iron-embedded monolayer MoS_2. *Applied Surface Science*, 328, pp. 71-77.

Macdonald, J.R. and Barsoukov, E., 2005. Impedance spectroscopy: theory, experiment, and applications. *History*, *1*(8), pp.1-13.

Merki, D., Vrubel, H., , Roveli, L., Fierro, S. and Hu, X. 2012. Fe, Co, and Ni ions promote the catalytic activity of amorphous molybdenum sulfide films for hydrogen evolution. *Chemical Science*, 3(8), pp. 2515-2525.

Matamoros-Veloza, A., Cespedes, O., Johnson, B. R., Stawski, T. M., Terranova, U., de Leeuw, N. H., & Benning, L. G., 2018. A highly reactive precursor in the iron sulfide system. *Nature communications*, *9*(1), 3125.

Mumtaz, A., Mohamed, N.M., Mazhar, M., Ehsan, M.A. and Mohamed Saheed, M.S., 2016. Core–shell vanadium modified titania@ β-In_2S_3 hybrid nanorod arrays for superior interface stability and photochemical activity. *ACS applied materials & interfaces*, *8*(14), pp.9037-9049.

Mumtaz, A., Mohamed, N.M., Saheed, M.S.M., Yar, A. and Irshad, M.I., 2016, November. Enhanced photoelectrochemical activity by nanostructured V_2O_5/TiO_2 bilayer. In *AIP Conference Proceedings* (Vol. 1787, No. 1, p. 030001). AIP Publishing LLC

Najmaei, S., Liu, Z., Zhou, W., Zou, X., Shi, G., Lei, S., Yakobson, B.I., Idrobo, J.C., Ajayan, P.M. and Lou, J., 2013. Vapour phase growth and grain boundary structure of molybdenum disulphide atomic layers. *Nature materials*, *12*(8), p.754.

Najmaei, S., Yuan, J., Zhang, J., Ajayan, P. and Lou, J., 2014. Synthesis and defect investigation of two-dimensional molybdenum disulfide atomic layers. *Accounts of chemical research*, *48*(1), pp.31-40

Osterloh, F.E. and Parkinson, B.A., 2011. Recent developments in solar water-splitting photocatalysis. *MRS bulletin*, 36(1), pp.17-22.

Peng, H., Lu, J., Wu, C., Yang, Z., Chen, H., Song, W., Li, P. and Yin, H., 2015. Co-doped MoS_2NPs with matched energy band and low overpotential high efficiency convert CO_2 to methanol. *Applied Surface Science,* 353, pp. 1003-1012.

Petrucci, R.H., Cunningham, C.M. and Moore, T.E., 1989. *General chemistry* (pp. 495-497). New York: Macmillan.

Pleskov, Y.V. and Gurevich, Y.Y., 1986. Semiconductor photoelectrochemistry.

Qiu, H., Xu, T., Wang, Z., Ren, W., Nan, H., Ni, Z., Chen, Q., Yuan, S., Miao, F., Song, F. and Long, G., 2013. Hopping transport through defect-induced localized states in molybdenum disulphide. *Nature communications*, *4*, p.2642.

Rahman, I.A. and Purqon, A., 2017, July. First Principles Study of Molybdenum Disulfide Electronic Structure. In *Journal of Physics: Conference Series* 877(1), pp. 12026.

Regula, M., Ballif, C., Remskar, M. and Levy, F., 1997. Crystalinity and texture promotion in WS_2 thin films. *Journal of Vacuum Science & Technology A: Vacuum Surfaces, and Films,* 15(4), pp. 2323-2329.

Roger, I., Shipman, M.A. and Symes, M.D., 2017. Earth-abundant catalysts for electrochemical and photoelectrochemical water splitting. *Nature Reviews Chemistry*, 1(1), p.0003.

Roger, I., Moca, R., Miras, H.N., Crawford, K.G., Moran, D.A.G., Ganin, A.Y., and Symes, M.D., 2017. The direct hydrothermal deposition of cobalt-doped MoS_2 onto fluorine-doped SnO_2 substrates for catalysis of the electrochemical hydrogen evolution reaction. *Journal of Materials Chemistry A*, 5, pp. 1472-1480.

Salitra, G., Hodes, G., Klein, E. and R, Tenne., 1993. Highly oriented WSe_2 thin films prepared by selenization of evaporated WO_3. *Thin solid films*, 245, pp. 184-185.

Sanne, A., Ghosh, R., Rai, A., Movva, H.C.P., Sharma, A., Rao, R., Mathew, L. and Banerjee, S.K., 2015. Top-gated chemical vapor deposited MoS_2 field-effect transistors on Si_3N_4 substrates. *Applied Physics Letters*, 106(6), p.062101.

Sarkar, D., Liu, W., Xie, X., Anselmo, A. C., Mitragotri, S., and Banerjee, K. MoS_2 field-effect transistor for next-generation label-free biosensors., 2014. *ACS nano*, *8*(4), 3992-4003.

Schweicher, G., Oliver, Y., Lemaur, V. and Geerts, Y.H., 2014. What currently limits charge mobility in crystals of molecular semiconductors?. *Israel Journal of Chemistry*, 54(5-6), pp. 596-620.

Shi, J., Yang, Y., Zhang, Y., Ma, D., Wei, W., Ji, Q., Zhang, Y., Song, X., Gao, T., Li, C. and Bao, X., 2015. Monolayer MoS_2 Growth on Au Foils and On-Site Domain Boundary Imaging. *Advanced Functional Materials*, *25*(6), pp.842-849.

Shi, J., Zhang, X., Ma, D., Zhu, J., Zhang, Y., Guo, Z., Yao, Y., Ji, Q., Song, X., Zhang, Y. and Li, C., 2015. Substrate facet effect on the growth of monolayer MoS_2 on Au foils. *ACS nano*, *9*(4), pp.4017-4025.

Shi, Y., Zhou, Y., Yang, D.R., Xu, W.X., Wang, C., Wang, F.B., Xu, J.J., Xia, X.H. and Chen, H.Y., 2017. Energy level engineering of MoS_2 by transition-metal doping for accelerating hydrogen evolution reaction. *Journal of the American Chemical Society*, *139*(43), pp.15479-15485.

Sirringhaus, H., 2014. 25th Anniversary Article: Organic field-effect transistors: the path beyond amorphous silicon. *Advanced materials*, 26(9), pp. 1319-1335.

Sivula, K., Le Formal, F. and Gratzel, M., 2011. Solar water splitting: progress using hermatite (α-Fe$_2$O$_3$) photoelectrodes. *ChemSusChem*, 4(4), pp. 432-449.

Tanaka, I., Kleebe, H.J., Cinibulk, M.K., Bruley, J., Clarke, D.R. and Ruhle, M., 1994. Calcium concentration dependence of the intergranular film thickness in silicon nitride. Journal of the American Ceramic Society, 77(4), pp. 911-914.

Tang, B., Yu, Z.G., Seng, H.L., Zhang, N., Liu, X., Zhang, Y.W., Yang, W. and Gong, H., 2018. Simultaneous edge and electronic control of MoS$_2$ nanosheets through Fe doping for an efficient oxygen evolution reaction. *Nanoscale*, *10*(43), pp.20113-20119.

Tedstone, A.A., Lewis, E.A., Savjani, N., Zhong, X.L., Haigh, S.J., O'Brien, P. and Lewis, D.J., 2014. Chemistry of Materials. *A Single Source Precursor for Tungsten Dichalcogenide Thin Films: Mo1-xWxS2 (0 ≤ x ≤ 1) Alloys by Aerosol-Assisted Chemical Vapor Deposition (AACVD),* 29(9), pp 3858–3862.

Tenne, R., Galun, E., Ennaoui, A., Fiechter, S., Ellmer, K., Kunst, M., Koelzow, C., Pettenkofer, C., Tiefenbacher, S., Scheer, R. and Jungblut, H., 1996. Characterization of oriented thin films of WSe$_2$ grown by van der Waals rheotaxy. *Thin sold films*, 272(1), pp. 38-42.

Tilley, S.D., 2019. Recent Advances and Emerging Trends in Photo-Electrochemical Solar Energy Conversion. *Advanced Energy Materials*, *9*(2), p. 1802877.

Topsøe, H., Clausen, B.S., Candia, R., Wivel, C. and Mørup, S., 1981. In situ Mössbauer emission spectroscopy studies of unsupported and supported sulfided Co-Mo hydrodesulfurization catalysts: Evidence for and nature of a Co-Mo-S phase. *Journal of Catalysis*, *68*(2), pp. 433-452.

Tosun, M., Chan, L., Amani, M., Roy, T., Ahn, G.H., Taheri, P., Carraro, C., Ager, J.W., Maboudian, R. and Javey, A., 2016. Air-stable n-doping of WSe_2 by anion vacancy formation with mild plasma treatment. *ACS nano*, *10*(7), pp.6853-6860.

Tsutsui, Y., Schweicher, G., Chattopadhyay, B., Sakurai, T., Arlin, J.B., Ruzié, C., Aliev, A., Ciesielski, A., Colella, S., Kennedy, A.R. and Lemaur, V., 2016. Unraveling Unprecedented Charge Carrier Mobility through Structure Property Relationship of Four Isomers of Didodecyl [1] benzothieno [3, 2-b][1] benzothiophene. *Advanced materials*, 28(33), pp.7106-7114.

Van Zeghbroeck, B., 2004. Principles of semiconductor devices. *Colarado University*, *34*.

Vieyra-Eusebio, M.T. and Rojas, A., 2011. Vapor pressure and sublimation enthalpies of nickelocene and cobaltocene measured by thermogravity. *Journal of Chemical & Engineering Data, 56*(12), pp. 5008-5018.

Wang, H., Tsai, C., Kong, D., Chan, K., Abild-Pedersen, F., Nørskov, J.K. and Cui, Y., 2015. Transition-metal doped edge sites in vertically aligned MoS_2 catalysts for enhanced hydrogen evolution. *Nano Research*, *8*(2), pp.566-575.

Wang, S., Rong, Y., Fan, Y., Pacios, M., Bhaskaran, H., He, K. and Warner, J.H., 2014. Shape evolution of monolayer MoS_2 crystals grown by chemical vapor deposition. *Chemistry of Materials*, *26*(22), pp.6371-6379.

Wang, S.Y., Ko, T.S., Huang, C.C. and Huang, Y.S., 2014. Optical and electrical properties of MoS_2 and Fe-doped MoS_2. *Japanese Journal of Applied Physics,* 53(4S), p.04EH07.

Wang, S., Lee, G.D., Lee, S., Yoon, E. and Warner, J.H., 2016. Detailed atomic reconstruction of extended line defects in monolayer MoS_2. *ACS nano*, *10*(5), pp.5419-5430.

Wang, Z., Liu, P., Ito, Y., Ning, S., Tan, Y., Fujita, T., Hirata, A. and Chen, M., 2016. Chemical vapor deposition of monolayer $Mo_{1-x}W_xS_2$ crystals with tunable band gaps. *Scientific reports*, *6*, p.21536.

Wu, J., Hu, Z., Jin, Z., Lei, S., Guo, H., Chatterjee, K., Zhang, J., Yang, Y., Li, B., Liu, Y. and Lai, J., 2016. Spiral Growth of $SnSe_2$ Crystals by Chemical Vapor Deposition. *Advanced Materials Interfaces*, *3*(16), p.1600383.

Xie, G., Zhang, K., Guo, B., Liu, Q., Fang, L. and Gong, J.R., 2013. Graphene-based materials for hydrogen generation from light-driven water splitting. *Advanced materials*, *25*(28), pp.3820-3839.

Xiong, Q., Zhang, X., Wang, H., Liu, G., Wang, G., Zhang, H. and Zhao, H., 2018. One-step synthesis of cobalt-doped MoS_2 nanosheets as bifunctional electrocatalysts for overall water splitting under both acidic and alkaline conditions. *Chemical Communications*, *54*(31), pp.3859-3862.

Yan, Z., Peng, Z. and Tour, J.M., 2014. Chemical vapor deposition of graphene single crystals. *Accounts of chemical research*, *47*(4), pp.1327-1337.

Ye, J., Chen, W., Xu, S., Yu, Z. and Hou, S., 2016. Synthesis of Co-doped MoS_2/graphene hybrids as enhanced electrocatalysts for the hydrogen evolution reaction. *RSC Advances*, *6*(106), pp. 104925-104932.

Young, K.M., Klahr, B.M., Zandi, O. and Hamann, T.W., 2013. Photocatalytic water oxidation with hematite electrodes. *Catalysis Science & Technoligy*, 3(7), pp. 1660-1671.

Yu, L., Xia, B.Y., Wang, X. and Lou, X.W., 2016. General formation of $M–MoS_3$ (M= Co, Ni) hollow structures with enhanced electrocatalytic activity for hydrogen evolution. *Advanced materials*, 28(1), pp.92-97.

Yu, Y., Huang, S.Y., Li, Y., Steinmann, S.N., Yang, W. and Cao, L., 2014. Layer-dependent electrocatalysis of MoS_2 for hydrogen evolution. *Nano letters*, *14*(2), pp.553-558.

Yu, Y., Li, C., Liu, Y., Su, L., Zhang, Y. and Cao, L., 2013. Controlled scalable synthesis of uniform, high quality monolayer and few-layer MoS_2 films. *Scientific reports, 3,* pp. 1866.

Yue, Q., Chang, S., Qin, S. and Li, J., 2013. Functionalization of monolayer MoS_2 by substitutional doping: a first-principles study. *Physics Letters A, 377*(19-20), pp. 1362-1367.

Zhang, L. F., Ou, G., Gu, L., Peng, Z. J., Wang, L. N., & Wu, H., 2016. A highly active molybdenum multisulfide electrocatalyst for the hydrogen evolution reaction. *RSC Advances*, *6*(109), 107158-107162.

Zhang, Z., Ji, X., Shi, J., Zhou, X., Zhang, S., Hou, Y., Qi, Y., Fang, Q., Ji, Q., Zhang, Y. and Hong, M., 2017. Direct chemical vapor deposition growth and band-gap characterization of MoS_2/h-BN van der Waals heterostructures on Au foils. *ACS nano*, *11*(4), pp.4328-4336.

Zheng, F., Huang, N., Peng, R., Ding, Y., Li, G., Xia, Z., Sun, P., Sun, X. and Geng, J., 2018. Cobalt-doped molybdenum disulfide in-situ grown on graphite paper with excellent electrocatalytic activity for triiodide evolution. *Electrochemica Acta*, *263*, pp. 328-337.

Zhou, X., Gan, L., Tian, W., Zhang, Q., Jin, S., Li, H., Bando, Y., Golberg, D. and Zhai, T., 2015. Ultrathin SnSe2 Flakes Grown by Chemical Vapor Deposition for High-Performance Photodetectors. *Advanced Materials*, *27*(48), pp.8035-8041.

Zhou, X., Shi, J., Qi, Y., Liu, M., Ma, D., Zhang, Y., Ji, Q., Zhang, Z., Li, C., Liu, Z. and Zhang, Y., 2016. Periodic modulation of the doping level in striped MoS_2 superstructures. *ACS nano*, *10*(3), pp.3461-3468.

APPENDICES

Appendix A

Calculations of conduction and valence band potential of MoS_2:

1 eV = 96.48 kJ/mol

Electron affinity of Mo, E_{EA} = 72.1 kJ/mol / 96.48 = 0.747 eV

First ionization of Mo, E_{ion} = 684.3 kJ/mol / 96.48 = 7.093 eV

Electronegativity of Mo, X_{Mo} = 0.5(E_{EA} + E_{ion}) = 3.92 eV

Electron affinity of S, E_{EA} = 200.4 kJ/mol/ 96.48 = 2.077 eV

First ionization of S, E_{ion} = 999.6 kJ/mol/ 96.48 = 10.36 eV

Electronegativity of S, X_S = 0.5(E_{EA} + E_{ion}) = 6.22 eV

Therefore, the electronegativity for MoS_2 of X_{MoS_2} is:

$$X_{MoS_2} = (X_{Mo} \times X_S \times X_S)^{1/n}$$

$$= (3.92 \text{ eV} \times 6.22 \text{ eV} \times 6.22 \text{ eV})^{1/3}$$

$$= 5.33 \text{ eV}$$

Conduction band of MoS$_2$, $E_{CB} = X_{MoS_2} - 0.5(E_g) - E_c$

$$= 5.32 \text{ eV} - 0.5(1.9 \text{ eV}) - 4.5 \text{ eV}$$

$$= -0.12 \text{ eV}$$

Valence band of MoS$_2$, $E_{VB} = E_{CB} - E_g$

$$= -0.12 \text{ eV} + 1.9 \text{ eV}$$

$$= 1.78 \text{ eV}$$

Where E_g and E_c are band gap value and energy of the free electron in the hydrogen scale (4.5 eV), respectively.

Calculations of conduction and valence band potential of Mo$_2$S$_3$:

Electron affinity of Mo, E_{EA} = 72.1 kJ/mol / 96.48 = 0.747 eV

First ionization of Mo, E_{ion} = 684.3 kJ/mol / 96.48 = 7.093 eV

Electronegativity of Mo, X_{Mo} = 0.5(E_{EA} + E_{ion}) = 3.92 eV

Electron affinity of S, E_{EA} = 200.4 kJ/mol/ 96.48 = 2.077 eV

First ionization of S, E_{ion} = 999.6 kJ/mol/ 96.48 = 10.36 eV

Electronegativity of S, X_S = 0.5(E_{EA} + E_{ion}) = 6.22 eV

Therefore, the electronegativity for MoS_2 of $X_{Mo_2S_3}$ is:

$$X_{Mo_2S_3} = (X_{Mo} \times X_{Mo} \times X_S \times X_S \times X_S)^{1/n}$$

$$= (3.92 \text{ eV} \times 3.92 \text{ eV} \times 6.22 \text{ eV} \times 6.22 \text{ eV} \times 6.22 \text{ eV})^{1/5}$$

$$= 5.17 \text{ eV}$$

Conduction band of Mo_2S_3, $E_{CB} = X_{Mo_2S_3} - 0.5(E_g) - E_c$

$$= 5.17 \text{ eV} - 0.5(2.3 \text{ eV}) - 4.5 \text{ eV}$$

$$= -0.48 \text{ eV}$$

Valence band of Mo_2S_3, $E_{VB} = E_{CB} + E_g$

$$= -0.48 \text{ eV} + 2.3 \text{ eV}$$

$$= 1.82 \text{ eV}$$

Calculations of conduction and valence band potential of $Fe(MoS_2)_2$:

Electron affinity of Mo, E_{EA} = 72.1 kJ/mol / 96.48 = 0.747 eV

First ionization of Mo, E_{ion} = 684.3 kJ/mol / 96.48 = 7.093 eV

Electronegativity of Mo, X_{Mo} = 0.5(E_{EA} + E_{ion}) = 3.92 eV

Electron affinity of S, E_{EA} = 200.4 kJ/mol/ 96.48 = 2.077 eV

First ionization of S, E_{ion} = 999.6 kJ/mol/ 96.48 = 10.36 eV

Electronegativity of S, X_S = 0.5(E_{EA} + E_{ion}) = 6.22 eV

Electron affinity of Fe, E_{EA} = 15.0 kJ/mol/ 96.48 = 0.155 eV

First ionization of Fe, E_{ion} = 762.5 kJ/mol/ 96.48 = 7.903 eV

Electronegativity of Fe, X_{Fe} = 0.5(E_{EA} + E_{ion}) = 4.03 eV

Therefore, the electronegativity for $Fe(MoS_2)_2$ of $X_{Fe(MoS_2)_2}$ is:

$$X_{Fe(MoS_2)_2} = (X_{Fe} \times X_{Mo} \times X_{Mo} \times X_S \times X_S \times X_S \times X_S)^{1/n}$$

$$= (4.03 \text{ eV} \times 3.92 \text{ eV} \times 3.92 \text{ eV} \times 6.22 \text{ eV} \times 6.22 \text{ eV} \times 6.22 \text{ eV}$$

$$\times 6.22 \text{ eV})^{1/7}$$

$$= 5.12 \text{ eV}$$

Conduction band of $Fe(MoS_2)_2$, $E_{CB} = X_{Fe(MoS_2)_2} - 0.5(E_g) - E_c$

$$= 5.12 \text{ eV} - 0.5(1.6 \text{ eV}) - 4.5 \text{ eV}$$

$$= -0.18 \text{ eV}$$

Valence band of $Fe(MoS_2)_2$, $E_{VB} = E_{CB} + E_g$

$$= -0.18 \text{ eV} + 1.6 \text{ eV}$$

$$= 1.42 \text{ eV}$$

Calculations of conduction and valence band potential of $Co(MoS_2)_2$:

Electron affinity of Mo, $E_{EA} = 72.1$ kJ/mol / $96.48 = 0.747$ eV

First ionization of Mo, $E_{ion} = 684.3$ kJ/mol / $96.48 = 7.093$ eV

Electronegativity of Mo, $X_{Mo} = 0.5(E_{EA} + E_{ion}) = 3.92$ eV

Electron affinity of S, $E_{EA} = 200.4$ kJ/mol/ $96.48 = 2.077$ eV

First ionization of S, $E_{ion} = 999.6$ kJ/mol/ $96.48 = 10.36$ eV

Electronegativity of S, $X_S = 0.5(E_{EA} + E_{ion}) = 6.22$ eV

Electron affinity of Co, $E_{EA} = 61.0$ kJ/mol/ $96.48 = 0.632$ eV

First ionization of Co, $E_{ion} = 760.4$ kJ/mol/ $96.48 = 7.881$ eV

Electronegativity of Co, $X_{Co} = 0.5(E_{EA} + E_{ion}) = 4.26$ eV

Therefore, the electronegativity for $Co(MoS_2)_2$ of $X_{Co(MoS_2)_2}$ is:

$$X_{Co(MoS_2)_2} = (X_{Co} \times X_{Mo} \times X_{Mo} \times X_S \times X_S \times X_S \times X_S)^{1/n}$$

$$= (4.26 \text{ eV} \times 3.92 \text{ eV} \times 3.92 \text{ eV} \times 6.22 \text{ eV} \times 6.22 \text{ eV} \times 6.22 \text{ eV} \times 6.22 \text{ eV})^{1/7}$$

$$= 5.16 \text{ eV}$$

Conduction band of $Co(MoS_2)_2$, $E_{CB} = X_{Co(MoS_2)_2} - 0.5(E_g) - E_c$

$$= 5.16 \text{ eV} - 0.5(1.6 \text{ eV}) - 4.5 \text{ eV}$$

$$= -0.14 \text{ eV}$$

Valence band of $Co(MoS_2)_2$, $E_{VB} = E_{CB} + E_g$

$$= -0.14 \text{ eV} + 1.6 \text{ eV}$$

$$= 1.46 \text{ eV}$$

Calculations of conduction and valence band potential of Mo_3NiS_4:

Electron affinity of Mo, $E_{EA} = 72.1$ kJ/mol / $96.48 = 0.747$ eV

First ionization of Mo, $E_{ion} = 684.3$ kJ/mol / $96.48 = 7.093$ eV

Electronegativity of Mo, $X_{Mo} = 0.5(E_{EA} + E_{ion}) = 3.92$ eV

Electron affinity of S, $E_{EA} = 200.4$ kJ/mol/ $96.48 = 2.077$ eV

First ionization of S, $E_{ion} = 999.6$ kJ/mol/ $96.48 = 10.36$ eV

Electronegativity of S, $X_S = 0.5(E_{EA} + E_{ion}) = 6.22$ eV

Electron affinity of Ni, $E_{EA} = 111.7$ kJ/mol/ $96.48 = 1.158$ eV

First ionization of Ni, $E_{ion} = 737.1$ kJ/mol/ $96.48 = 7.640$ eV

Electronegativity of Ni, $X_{Ni} = 0.5(E_{EA} + E_{ion}) = 4.40$ eV

Therefore, the electronegativity for Mo_3NiS_4 of $X_{Mo_3NiS_4}$ is:

$$X_{Mo_3NiS_4} = (X_{Mo} \times X_{Mo} \times X_{Mo} \times X_{Ni} \times X_S \times X_S \times X_S \times X_S)^{1/n}$$

$$= (3.92 \text{ eV} \times 3.92 \text{ eV} \times 3.92 \text{ eV} \times 4.40 \text{ eV} \times 6.22 \text{ eV} \times 6.22 \text{ eV}$$

$$\times 6.22 \text{ eV} \times 6.22 \text{ eV})^{1/8}$$

$$= 5.01 \text{ eV}$$

Conduction band of Mo_3NiS_4, $E_{CB} = X_{Mo_3NiS_4} - 0.5(E_g) - E_c$

$$= 5.01 \text{ eV} - 0.5(1.6 \text{ eV}) - 4.5 \text{ eV}$$

$$= -0.29 \text{ eV}$$

Valence band of $Co(MoS_2)_2$, $E_{VB} = E_{CB} + E_g$

$$= -0.29 \text{ eV} + 1.6 \text{ eV}$$

$$= 1.31 \text{ eV}$$